University of Nevada, Reno

Sensitive Force Measurements With Optically Trapped Micro-Spheres in High Vacuum

A dissertation submitted in partial fulfillment of the
requirements for the degree of Doctor of Philosophy
in Physics

by

David P. Atherton

Dr. Andrew A. Geraci, Dissertation Advisor

May 2015

THE GRADUATE SCHOOL

We recommend that the dissertation
prepared under our supervision by

DAVID P. ATHERTON

Entitled

Sensitive Force Measurments With Optically Trapped Micro-Spheres in High Vacuum

be accepted in partial fulfillment of the
requirements for the degree of

DOCTOR OF PHILOSOPHY

Andrew Geraci, PhD., Advisor

Jonathan Weinstein, PhD., Committee Member

Andrei Derevianko, PhD., Committee Member

Sean Casey, PhD., Committee Member

Josh Baker, PhD, Graduate School Representative

David W. Zeh, Ph. D., Dean, Graduate School

May, 2015

Abstract

This dissertation details our work on optically levitating and cooling micro-spheres in vacuum for use as force sensors. We have extensively modeled various optical trap configurations to determine stable trap geometries for μm sized spheres in a dual-beam optical trap. Techniques have been developed for overcoming instabilities which occur when pumping trapped micro-spheres from low to high vacuum. We have also improved on methods for depositing micro-spheres in optical traps.

We have shown that optically levitated micro-spheres are excellent force sensors. By eliminating the need to tether the spheres to a solid substrate, excellent environmental decoupling is achieved. In this work we present the realization of aN force sensitivity. The intended use for the technology developed is to extend the search for non-Newtonian gravity by several orders of magnitude at the micrometer length scale [1]. This technology is also suitable for investigating the Casimir effect in the unexplored regime where neither the Proximity Force Approximation or the Casimir-Polder limits are valid.

Citations to Previously Published Work

Portions of this thesis have appeared previously in the following papers:

David P. Atherton, Gambhir Ranjit, Andrew A. Geraci, and Jonathan D. Weinstein. Observation of a classical cheshire cat in an optical interferometer. Opt. Lett., 40(6):879-881, Mar 2015.

Gambhir Ranjit, David P. Atherton, Jordan H. Stutz, Mark Cunningham, and Andrew A. Geraci. Sub-an force detection using microspheres in a dual beam optical trap in high vacuum. arXiv:1503.08799, April 2015. Accepted at Phys. Rev. A, May 2015

Acknowledgments

I would like to thank my PhD advisor, Dr. Andrew Geraci, for his support, encouragement, and feedback throughout this effort. Additional thanks go to my committee members, Drs. Jonathan Weinstein, Andrei Derevianko, Sean Casey and Josh Baker, for their time, expertise, and valuable perspective.

Many thanks to Dr. Gambhir Ranjit for his hard work and outstanding mentorship. Additional thanks to Wade Cline and Carl Davidson for their machine shop assistance and experimental expertise.

To the UNR Physics Department, especially the office staff, for guidance and logistical support.

Finally, to my friends and family: I am forever grateful for all of your love and support.

This work is funded by National Science Foundation grant # NSF PHY-1205994.

Contents

List of Figures

Chapter 1

Motivation for This Experiment

1.1 Levitated Micro-Spheres as Force Sensors

Optically levitated and cooled dielectric micro-spheres in high vacuum show great promise as resonant force detectors. By eliminating the need to tether the spheres to a solid substrate, excellent environmental decoupling is expected. In this work we present the realization of attonewton force sensitivity.

We intend to use this new technology to extend the search for non-Newtonian gravity by several orders of magnitude at the micrometer length scale [1]. This technology is also suitable for investigating the Casimir effect in the unexplored regime between where the Proximity Force Approximation and the Casimir-Polder limits are valid.

Figure 1.1 depicts the basic experiment we are developing for measuring the Casimir force and gravity at the micrometer length scale. Two lasers are injected into an optical cavity composed of a curved glass mirror and a grounded gold mirror. One laser traps a micro-sphere at an anti-node of a standing wave created by the trapping laser. The second laser cools the center-of-mass mode of the sphere along the cavity axis via sideband cooling. This laser also measures the center-of-mass motion of the sphere by measuring the phase shift $\delta\varphi$ of the light reflected from the cavity. The phase shift is proportional to the sphere's displacement δx.

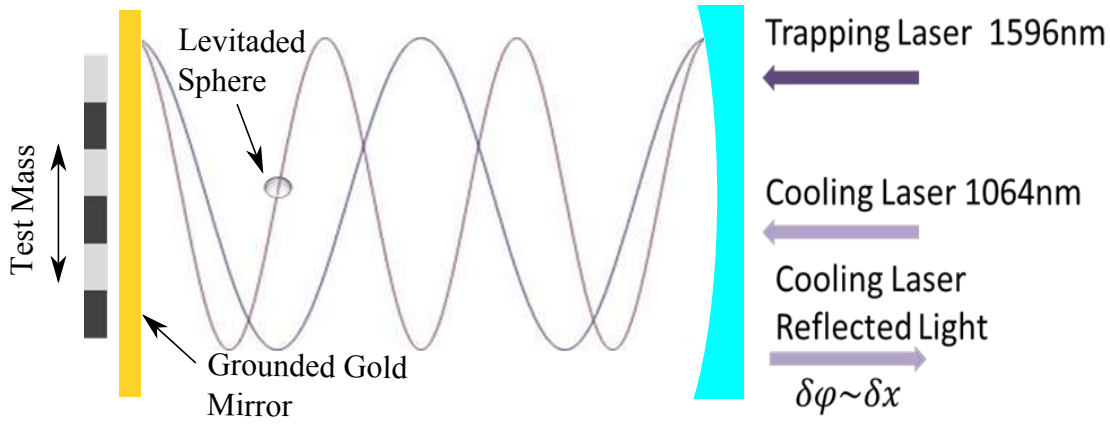

Figure 1.1: The basic experiment we are developing for measuring short range forces. Two lasers are injected into an optical cavity composed of a curved mirror and a grounded flat gold mirror. One laser traps a micro-sphere at an anti-node. The second laser cools the center-of-mass motion of the sphere along the cavity axis. The change in phase $\delta\varphi$ of the cooling laser light reflected from the optical cavity results from the sphere displacement δx. A test mass with varying density oscillates transverse to the optical cavity and applies a time varying gravitational force on the sphere. We plan to use this system to investigate corrections to Newtonian gravity and the Casimir force at the μm scale.

1.2 Corrections to Newtonian Gravity

1.2.1 The Hierarchy Problem

A phenomenon that perplexes many scientists is the large discrepancy between the strength of the other Standard Model forces and gravity. Many scientists feel that there should only be one fundamental scale in nature. Based on our current measurements and theories, there appear to be two unique energy scales in nature. The electroweak scale, given from the Standard Model, is roughly $E_{EW} \sim 10^3$ GeV. These interactions have been extensively probed through various high energy physics experiments. For example, the Large Hadron Collider has performed experiments with energy up to 8 TeV [2]. The Planck energy scale, $E_{Pl} \sim 1.22 \times 10^{19}$ GeV, is by definition the energy where quantum effects of gravity can no longer be ignored. This energy corresponds to a length scale of $l_{Pl} \sim 1.6 \times 10^{-35}$ m. In 2007, the record for shortest interaction measurement of gravity was 55 μm [3]. This approximately 10^{30}

orders of magnitude greater than the Planck scale. It is the belief of many scientists that somewhere within this enormous experimental space lies the unification of gravity and the Standard Model.

1.2.2 Parameterizing Corrections to Newtonian Gravity

A number of theories predict a Yukawa-type correction to gravity. Refs. [4, 5] suggest new forces mediated by light moduli from string theory and Refs. [6, 7, 8] predict exotic particles in "large" extra dimensions as force mediators. The Yukawa-type correction to Newtonian gravity is given by:

$$V(r) = -\frac{Gm_1m_2}{r}[1 + \alpha e^{-r/\lambda}], \tag{1.1}$$

where m_1 and m_2 are two masses interacting at a distance r. α is the strength of the potential compared to classical gravity and λ is the potential interaction length. The interaction length corresponds to the Compton wavelength of the particle being exchanged. For $r \ll \lambda$, the second term in equation 1.1 vanishes and only the Newtonian term remains. If $\lambda \sim r$ or smaller, a non-negligible and non-classical term remains. Figure 1.2 shows the experimental phase space Yukawa-type corrections to Newtonian gravity at short range. The area shaded in yellow has already been excluded by experiments, while the remaining area is space that has yet to be explored. We expect our levitated micro-sphere system to further the search into the areas outlined in red and centered around λ=1 μm. Curve (a) is for a 300 nm and curve (b) is for a 3 μm sphere.

1.2.3 Measuring Gravity at Short Range

Ref. [9] is a review from 1996 which shows that new forces with a strength weaker than or comparable to gravity over distances between 1 cm and 10^{17} cm have been excluded by experiment. Figure 1.3 give the α and λ constraints from experiments conducted up until 1996 [9].

The first sub-cm measurements were reported by Lamoreaux [10] in 1997. Torsional balance experiments investigated large deviations ($\alpha > 10^8$) in the 0.6 to 6

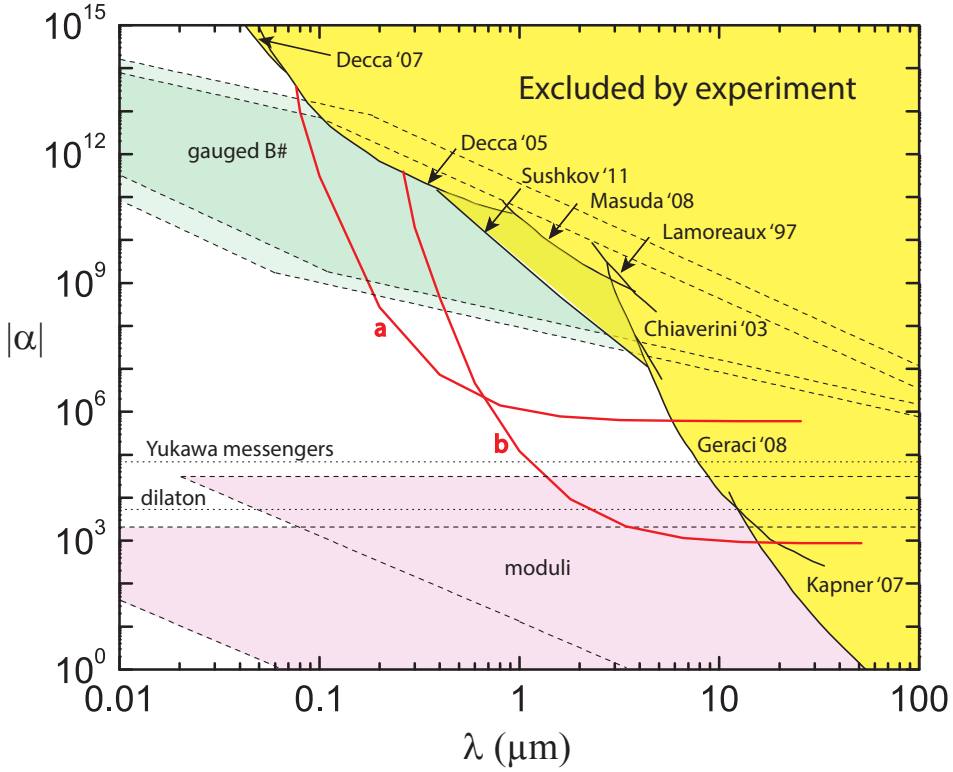

Figure 1.2: Experimental phase space plot for corrections to Newtonian gravity. α is the strength of corrections relative to Newtonian gravity and λ is the gravitational interaction length. The area in yellow has already been excluded by previous experiments where α was not measured and measurements agree with Newtonian gravity. The red curves a and b represent the areas where we expect to further the search. The difference between curves a and b is the size of the micro-sphere used, respectively, 300 nm and 3 μm spheres. Adapted from Ref. [1]

μm range. In 2003, Chiaverini et al. reported on cantilever experiments which put a lower limit of $\alpha \sim 10^4$ at length scales of 20 μm [11]. Also in that year, Long et al. [12] used a planar oscillator to place limits at the $\sim$100 μm range. In 2005, Decca et al. [13] used a microelectromechanical torsional oscillator to place a limit of $\alpha < 10^{12}$ at 200 nm. Then, in 2007, a similar experiment [14] placed constraints for the 29.5 nm to 86 nm range with $\alpha > 10^{14}$. Also in 2007, Kapner et al. [3] reported the first (and only to date) sub-mm result that placed $\alpha < 1$. This experiment was performed at 55 μm with a torsional balance. In 2008, Mesuda et al. [15] placed limits at the 1.0-2.9 μm range with a torsional balance experiment and Geraci et al. [16] placed limits on the range of 5 - 15 μm with cantilever experiments. The most recent sub-mm gravity

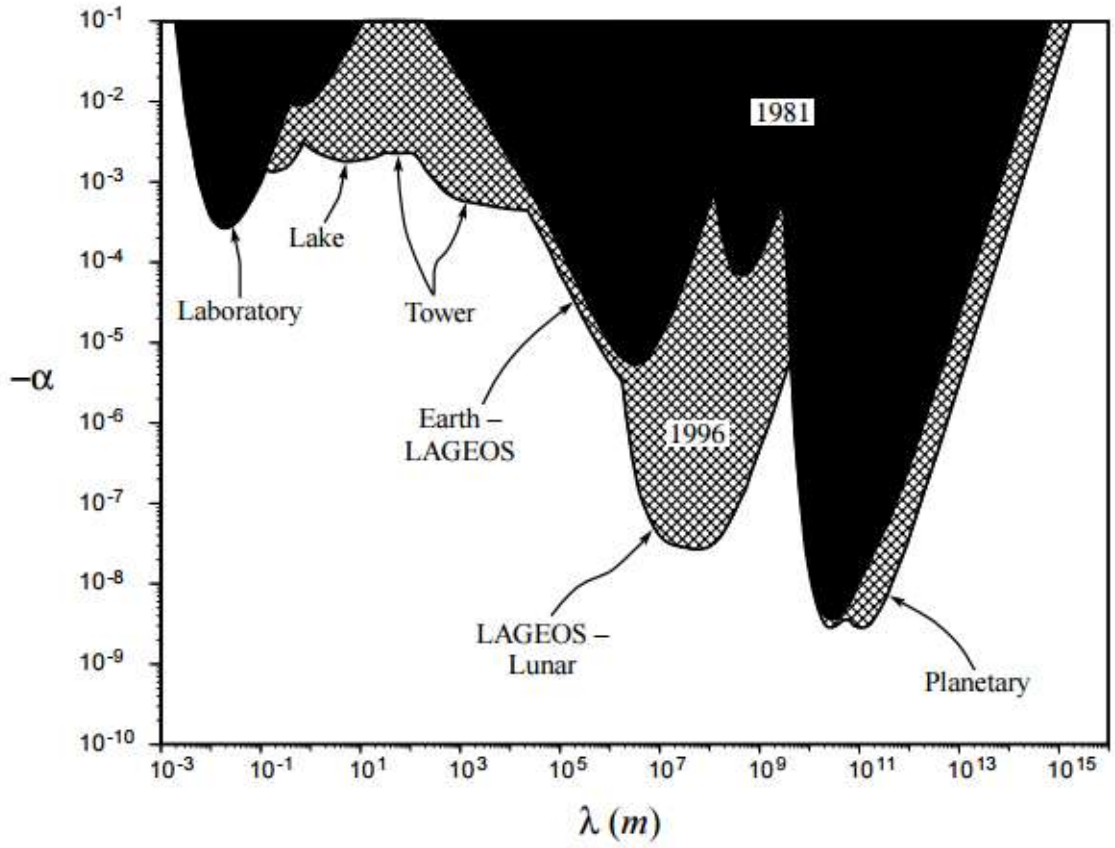

Figure 1.3: Experimental phase space plot for corrections to Newtonian gravity up to and prior to 1996. α is the strength of corrections relative to Newtonian gravity and λ is the gravitational interaction length. Taken from Ref. [9]

measurement was performed by Sushkov et al. [17], where they placed limits on the 0.7 μm and 7.0 μm range with a torsional balance. All of the results discussed in this section, with the exception of ref. [12], are plotted in figure 1.2 and represent the current limits.

1.3 Casimir Effect

The intuitive picture of vacuum as a volume completely void of particles with a temperature of absolute zero fails to capture the presence of fluctuating fields, such as electromagnetic fields in that volume. Quantum mechanics tells us that all fields fluctuate around a mean value and that fields in a vacuum are not exempt. As such,

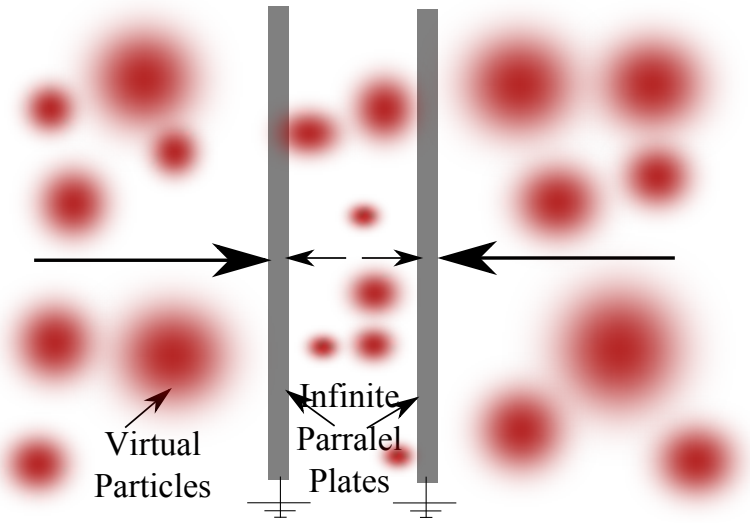

Figure 1.4: Two infinite uncharged parallel plates spaced closely together. A) The plates feel an attractive force since fewer vacuum fluctuation modes meet the boundary conditions between the plates a than outside of the plates. B) The plates feel an attractive force because fewer modes of virtual particles fit within the space between the plates a than outside of the plates.

vacuums have energy known as the zero-point energy resulting from field fluctuations know as vacuum fluctuations. Vacuum fluctuations can be described as virtual particles randomly popping into and out of the vacuum.

A different method for representing a non-zero vacuum energy is to look at the energy time uncertainty.

$$\triangle E \cdot \triangle t \geq \frac{\hbar}{2}, \tag{1.2}$$

where $\triangle E$ is the vacuum energy uncertainty, $\triangle t$ is the uncertainty in time of the measurement and $\hbar$ is Planck's constant. The vacuum energy uncertainty will always be non-zero allowing for a zero-point energy.

The example typically used to illustrate the Casimir Effect is depicted in figure 1.4. Two uncharged infinite parallel plates are placed closely together in vacuum. In figure 1.4 there is a net force on each plate bringing them together. This is because fewer modes of virtual particles fit within the plates than outside due to boundary conditions. The force pushing the two plates together is known as the Casimir force.

The force per unit area for the infinite parallel plate example was calculated by Casimir in 1948 [18] and given by

$$\frac{F_c}{A} = -\frac{d}{dx}\frac{\langle E\rangle}{A} = -\frac{\hbar c\pi^2}{240a^4}. \tag{1.3}$$

$\langle E\rangle$ is the vacuum energy expectation value, c is the speed of light and a is the separation between the plates.

The Casimir effect is in fact a real phenomenon and the Casimir force has been measured previously. In practice, it is very difficult to have two planes perfectly parallel. This caused early attempts to measure the Casimir force to be overwhelmed with uncertainty [19][20]. However, in the late 1990s, the Casimir force between a plane and sphere (see figure 1.5) were measured by two groups [10][21]. In these experiments, the of curvature of the sphere R was very large compared to the separation between the sphere and plate L (figure 1.5.B.) In this limit, where $R \gg L$, a mathematical solution exists know as the proximity force approximation (PFA). The formula for the PFA is provided in Ref. [10] and given by

$$F_{PFA} = 2\pi R\left(\frac{1}{3}\frac{\pi^2}{240}\frac{\hbar c}{a^3}\right), \tag{1.4}$$

where R is the radius of the sphere. A solution also exists for the limit where $R \ll L$ (figure 1.5.A) know as the Casimir-Polder limit where experiments agree [22][23]. The Casimir-Polder force for a metallic plane and dielectric sphere is given by

$$F_{CP} = -\frac{3\hbar c\alpha}{8\pi^2\epsilon_0}\frac{1}{a^5}, \tag{1.5}$$

where α is the electric polarizability and ϵ_0 is the vacuum permitiivity [24].

The PFA and Casimir-Polder limit are both not valid in the limit where $R \sim L$ (figure 1.5.C.) Measuring the Casimir force in this regime has proven difficult because the force sensor, such as a cantilever in an atomic force microscope, is mechanically clamped to the sphere and contributes to the Casimir effect by a non-trivial amount. Since our system is completely mechanically decoupled from the environment, we expect to successfully measure the Casimir force within this unexplored regime. The

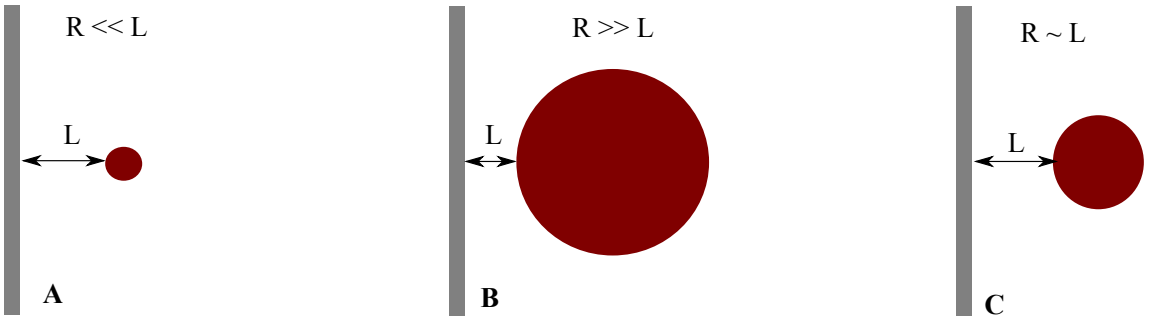

Figure 1.5: Depiction of the plane-sphere geometry for measuring the Casimir force. A) The the Casimir-Polder limit where the radius of curvature R of the sphere is significantly smaller then the separation between the sphere and plane L ($R \ll L$.) B) The PFA limit where $R \gg L$. C) The unexplored limit where $R \sim L$. We expect levitated micro-sphere force sensors to significantly improve measurements within this regime.

theory for this has been worked out in Ref. [25]. An undergraduate from our group performed calculations for our particular experimental geometry of a metallic mirror and dielectric sphere [26] where the PFA and Casimir-Polder limits disagree and are incorrect. Measurements within this regime could aid in the understanding of the heating of ultracold neutrons (UCNs) in traps near a surface [27, 28, 29].

Chapter 2

Laser Radiation Forces on Dielectric Spheres

2.1 History of micro-sphere trapping

In 1619, Johannes Kepler suggested that light radiated from the Sun could explain the observed phenomenon that a comet's tail always points away from the Sun [30]. A little over 250 years later, Maxwell worked out the mathematical framework for electricity and magnetism which suggests that electromagnetic radiation has momentum [31]. This was shown experimentally in 1900 by Pyotr Lededev [32] and by Ernest Nichols in 1901 [33]. Although the study of radiation forces was very exciting at the time, little progress was made in the field before the invention of the laser in 1960 by Charles Townes [34].

Without a doubt, Arthur Ashkin is the godfather of bead trapping. In 1970, while working at Bell Labs, Ashkin published the first experimental results showing that a focused laser beam can alter the dynamics of particles in liquid by radiation pressure [35][1]. Within this work, Ashkin identified two different radiation force components. The first component is referred to as the scattering force and is directed along the axis of laser propagation. The second component is referred to as the gradient force and is along the direction of the intensity gradient of the laser field. By exploiting these forces, Ashkin was able to show that a single focused laser beam could accelerate and

[1] An interesting factoid about [35] is that Arthur Ashkin proposes using frequency tuned lasers to trap and cool atoms which later earned Steve Chu, Claude Cohen-Tannoudji and Bill Phillips the 1997 Nobel Prize in Physics.

had the potential to three dimensionally trap particles. Ashkin's early work laid the foundation for the optical tweezers technology which revolutionized certain aspects biology and nanotechnology [36]. In 1971, Ashkin and Dziedzic reported the stable trapping of 20 μm glass spheres in air and vacuum at pressures down to $\sim$ 1 Torr [37]. In 1975, Ashkin and Dziedzic successfully trapped oil droplets down to $\sim 10^{-6}$ Torr, which is well within the high vacuum regime[38]. Within this work, radiometric forces, which arise from temperature gradients near the sphere and destabilize the trapped sphere are addressed. Radiometric forces are discussed in great detail in chapter 5. In 1976, Ashkin and Dziedzic published a paper describing a feedback stabilization technique for trapping glass spheres in air and vacuum [39], which aided in countering the radiometric forces responsible for trap loss at pressures around 1 Torr. It wasn't until 2011 that nm and μm scale glass spheres were successfully trapped at high vacuum pressures [40][41].

2.2 Arthur Ashkin's "Back of the Envelope" Radiation Pressure Calculation

Radiation pressure is simply defined as the pressure exerted on any surface exposed to electromagnetic radiation. In his seminal paper on radiation forces [35], Arthur Ashkin provided an intuitive "back of the envelope" calculation on the strength of radiation pressure. Below we reproduce his calculation.

Figure 2.1 depicts the free body diagram for a single photon reflecting from a flat mirror. The magnitude of the momentum of the photon before and after reflection is given by $p = \frac{h\nu}{c}$; where p is momentum, h is Boltzmann's constant, ν is the photon frequency and c is the speed of light. The total change in momentum of the photon from the reflection is:

$$|\vec{p}_{out} - \vec{p}_{in}| = 2p = 2\frac{h\nu}{c}. \tag{2.1}$$

Now, assume we have a laser with power P incident on the same mirror instead of a single photon. $\frac{P}{h\nu}$ photons strike the mirror per second, which produces a force

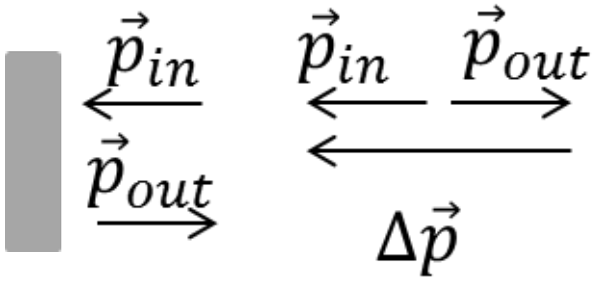

Figure 2.1: Free body diagram illustrating the change in momentum $\vec{\Delta p}$ for a single photon reflecting from a flat mirror with incident momentum $\vec{p}_{in}$ and reflected momentum $\vec{p}_{out}$.

$F_{radiation}$ on the mirror given by:

$$F_{radiation} = \frac{\Delta p}{\Delta t} = 2\frac{h\nu}{c}\frac{P}{h\nu} = \frac{2P}{c}. \tag{2.2}$$

For $P = 1W$,

$$F_{radiation} = \frac{2\text{x}1W}{3\text{x}10^8 m/s} = 6.7nN. \tag{2.3}$$

Although the force calculated above is small in absolute terms, it is useful for accelerating particles with small masses. Figure 2.2 depicts a 1 W laser focused to a diffraction limited spot of roughly 1 μm in diameter incident on 100% reflecting particle made of fused silica which is also 1 μm in diameter. The density, ρ, of fused silica (glass) is $\sim 2200\frac{kg}{m^3}$ which gives a particle mass of

$$m = \rho \times V \approx 1.3\text{x}10^{-15} kg \tag{2.4}$$

The acceleration, a, experienced by the particle is

$$\frac{F_{radiation}}{m} = \frac{6.7nN}{4\text{x}10^{-18} kg} \approx 10^9 \frac{m}{s^2} \approx 10^8 g, \tag{2.5}$$

where g, is the Earth's gravitational acceleration. Although this "back of the envelope" calculation provides an upper limit to the radiation force, it does suggest that focused laser beams can be used to overcome the Earth's gravity.

The remainder of this chapter is dedicated to improving Ashkin's "back of the envelope" calculation to more precise calculations of the radiation force from a focused

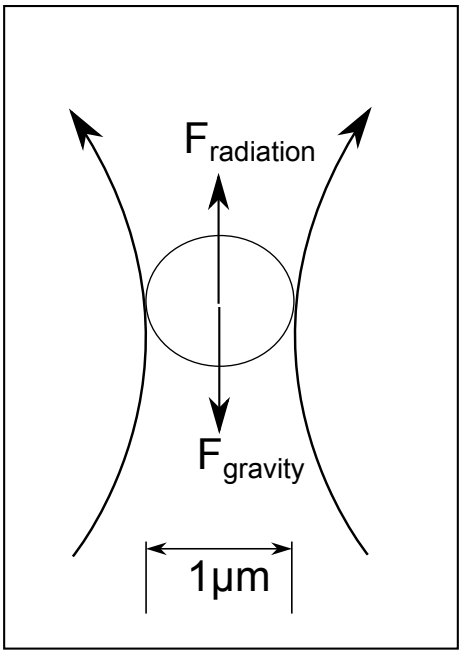

Figure 2.2: Free body diagram of a vertical optical trap. The radiation force $F_{radiation}$ counters the gravitational force $F_{gravity}$ providing a stable trapping potential.

laser beam on fused silica spheres. There are three models typically used for calculating the radiation force on micro-spheres which differ by the ratio of laser wavelength λ to the length scale of the bead r. For $r \gg \lambda$ we can use a ray optics approach. For $r \ll \lambda$ Rayleigh scattering provides an analytic solution. Lastly, when $r \approx \lambda$ we need to use a more complicated numerical Mie scattering approach.

2.3 Ray Optics Regime $r \gg \lambda$

Perhaps the most intuitive radiation force model is within the ray optics regime where the length scale r of the trapped particle is significantly larger than the trapping laser wavelength λ. In his first publication on radiation forces [35], Ashkin improved on the flat mirror description given in the previous section by replacing the 100% reflecting mirror with a refractive sphere near the focus of a laser beam as depicted in Figure 2.3. In figure 2.3, a particle is located just off of the beam axis of a Gaussian laser beam. Two photons a and b refract through the sphere at the same time. Since the photons' paths change direction they experience a change in momentum which

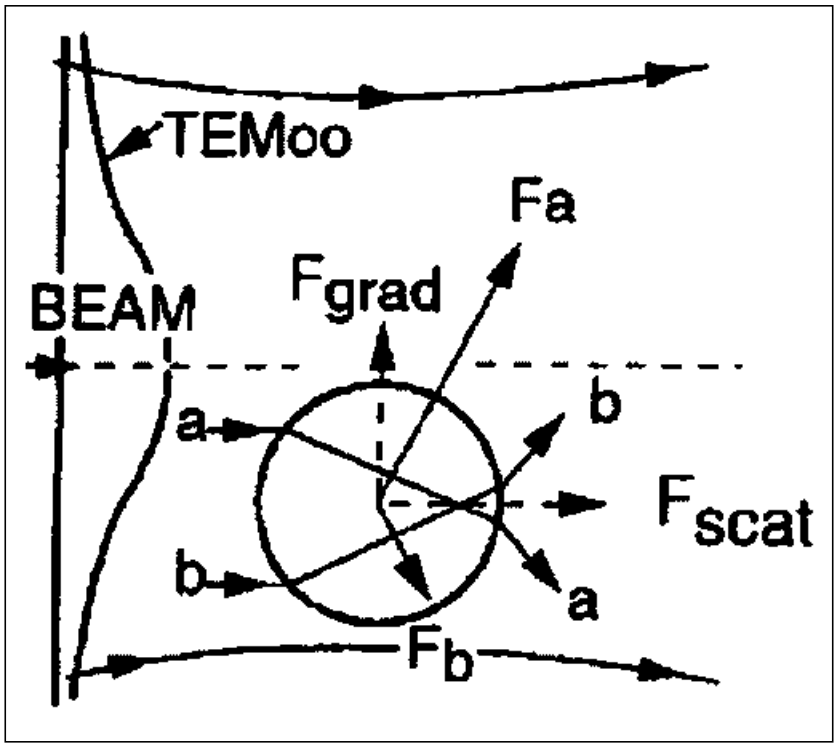

Figure 2.3: Depiction of a micro-sphere off axis within a Gaussian beam. The sphere experiences a scattering force F_{scat} along the axis of laser propagation and a gradient force F_{grad} in the direction of the laser intensity gradient. Figure taken from Ref. [35].

results in a radiation force of equal magnitude from both photons onto the particle. The net force from all photons incident at location a, F_a, is greater in magnitude than the net force from all photons incident at location b, F_b, since the laser intensity is greater at location a. Integrating the force over the face of the sphere in figure 2.3 results in a total force with a component parallel to the laser beam axis and a component pointing in the direction of the gradient of the laser intensity. These force components are referred to as the scattering force, F_{scat}, and the gradient force, F_{grad}, respectively.

Ashkin provided a second picture for visualizing radiation forces by treating the sphere as a lens near the focus of a laser beam [42], which is depicted in figure 2.4. When the sphere is located at the beam focus, rays pass through the sphere with a refraction angle equal to 0 resulting in no change of photon momentum and thus no

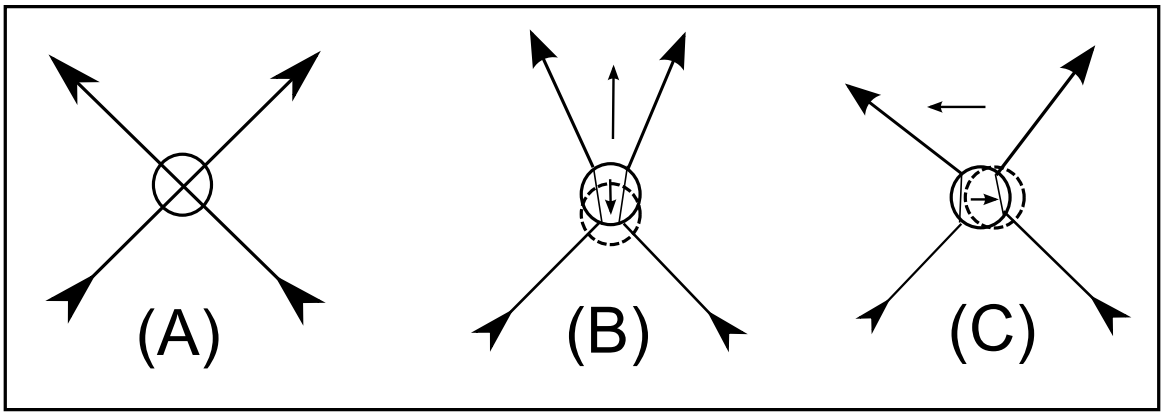

Figure 2.4: Illustration of a micro-sphere trapped near a tight laser focus. A) A sphere trapped at the laser focus experiences no gradient force. However, it does experience a scattering force along the axis of propagation. B) A sphere positioned near the focus but offset axially experiences an axial restoring force. C) A sphere positioned near the focus but offset radially experiences an radial restoring force.

force on the sphere (figure 2.4.A.) When the sphere is offset from the focus slightly along the beam axis, as in 2.4.B, the beam is more focused, resulting in a force that returns the micro-sphere towards the beam focus. For a sphere offset radially from the beam axis, as depicted in 2.4.C, the laser is deflected in such a way that a force on the bead moves it radially towards the beam focus. The forces drawn in 2.4 all restore the sphere to the beam focus resulting in a 3D harmonic trapping potential. It should be noted that the force in 2.4.B is a gradient force along the trap axis and the force in 2.4.C is a radial gradient force. In this picture we assume the laser focus is tight enough that we can ignore a scattering force along the beam propagation axis. If the laser focus was not sufficiently tight, the scattering force would dominate over the gradient in figure 2.4 resulting in sphere trap loss.

Although the ray optics pictures described in this section are simple and intuitive, actual force calculations are non-trivial due to the fact that the laser light can be reflected from the spheres and that there can be many internal reflections within the sphere. In our experiments, the ray optics picture served only as an intuitive mental picture for radiation forces. We primarily use 300 nm and 3 μm spheres in our experiments with 1064 nm and 1596 nm lasers. For more detailed analyses of radiation

forces in the ray optics regimes, [42, 43, 44, 45] provide for excellent references. Ref. [45] provides a thorough computational toolbox in MATLAB for calculating optical forces in the ray optics regime called Optical Tweezers in Geometrical Optics (OTGO) which is freely available for download.

2.4 Rayleigh Scattering Regime

The experiment described in section 1.1 requires a sphere to be trapped at the anti-node of a standing wave in an optical cavity. This imposes the requirement that the sphere's size be significantly smaller than the trapping laser wavelength($r \ll \lambda$.) Conveniently, Rayleigh scattering provides an analytic solution for calculating the radiation force on the sphere.

In simple terms, the electric field of the laser induces an electric dipole moment in the dielectric sphere. Since the laser field is time varying, the dipole oscillates within the field. This oscillation, in turn, radiates. The radiation force on the sphere is simply the result of the change in momentum of the incoming and out going field scattered from the sphere. Here we present the theory of radiation forces on a dielectric sphere in the Rayleigh scattering regime which is taken directly from Ref. [46].

The geometry for this model is given in figure 2.5. A linearly polarized Gaussian beam (TEM00 mode) is focused to a minimum waist of w_0 at the coordinates $(\mathbf{x}, \mathbf{y}, \mathbf{z}) = (0, 0, 0)$. The polarization direction of the laser's electric field is parallel to the x-axis and the laser propagates along the z-axis. A dielectric sphere of radius a is located at $\mathbf{r}$ within the Gaussian envelope of the laser.

The waist of a Gaussian beam as a function of axial position z is given by

$$w(z) = w_0 \left[1 + \left(\frac{\lambda z}{\pi w_0^2} \right)^2 \right]^{1/2}. \tag{2.6}$$

where w_0 is the minimum waist at $z = 0$ and λ is the laser wavelength. The intensity profile of a Gaussian beam is given by

$$I(x, y, z) = I_0(z) e^{\frac{-2(x^2+y^2)}{w(z)}} = \frac{2P}{\pi w^2(z)} e^{\frac{-2(x^2+y^2)}{w(z)}}, \tag{2.7}$$

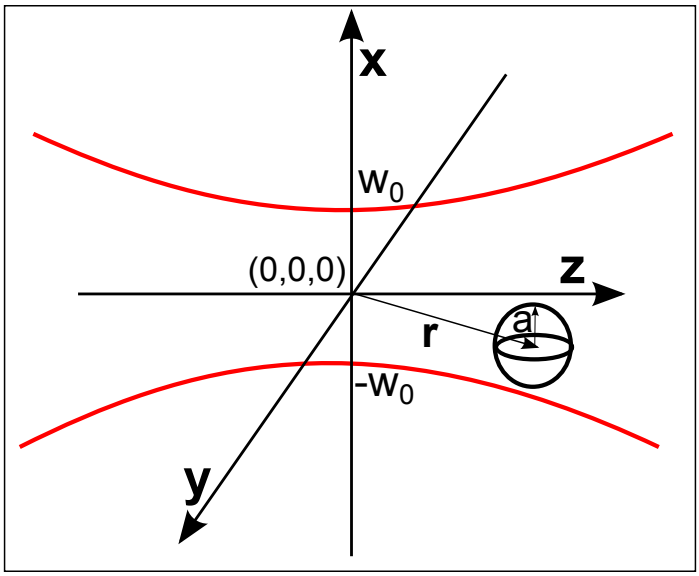

Figure 2.5: A linearly polarized Gaussian beam ($TEM00$ mode) is focused to a minimum waist of w_0 at the coordinates $(\mathbf{x}, \mathbf{y}, \mathbf{z}) = (0, 0, 0)$. The polarization direction of the laser's electric field is parallel to the x-axis and the laser propagates along the z-axis. A dielectric sphere of radius a is located at $\mathbf{r}$ within the Gaussian envelope of the laser.

where $I_0(z)$ is the intensity at the beam center and P is the laser power. As discussed in section 2.3, the radiation force can be separated into a force directed along the the beam propagation axis called the scattering force, F_{scat}, and a force along the gradient of the laser intensity called the gradient force, F_{grad}. The gradient force is proportional to the gradient of the beam intensity and provides a conservative trapping potential at the beam focus. However, the scattering force accelerates the sphere away from the beam focus. As such, the gradient force must be greater than the scattering force for a stable trap to be realized.

F_{scat} is given by [46]

$$\vec{F}_{scat} = \left(\frac{n_{md}}{c}\right) C_{scat} I(x, y, z)\hat{z} = \frac{128\pi^5 a^6}{3c\lambda^4} \left(\frac{m^2 - 1}{m^2 + 2}\right) n_{md}^5 I(x, y, z)\hat{z} \tag{2.8}$$

and F_{grad} is given

$$\vec{F}_{grad} = -\frac{2\pi n_{md} a^3}{c} \left(\frac{m^2 - 1}{m^2 + 2}\right) \nabla I(x, y, z); \tag{2.9}$$

where n_{md} is the index of refraction for the medium the particle is in, and C_{scat} is the scattering cross section of the sphere. m is a unit-less parameter that quantifies the

surface reflection of the sphere and is defined as the ratio of the index of refraction for the sphere n_{sphere} to the index of refraction of the medium: given by $m = n_{sphere}/n_{md}$. These force equations are valid for a particle near the trap center.

Since the intensity profile is symmetric about the x and y axes it is useful to look at the radial and axial radiation forces separately. Table 2.1 contains typical parameters used in our lab to calculate the forces plotted in figures 2.6 and 2.7.

Parameter	Value	Comments
a	300 nm	Typical bead radius used in our lab.
λ	1064 nm	Trap laser used in our lab
P	2.2 W	Trap laser power
w_0	10 μm	Trap laser minimum waist
n_{glass}	1.46	Refractive index at 1064nm
n_{vacuum}	1	By definition
m	1.46	n_{glass}/n_{vacuum}

Table 2.1: The parameters used for the force calculations presented in this section.

In figure 2.6, the scattering and gradient force contributions to the axial force are plotted. Since the non-conservative scattering force, figure 2.A, is significantly larger than the conservative gradient force, figure 2.6.B, the parameters in table 2.1 do not produce a stable trap along the beam axis. We dealt with this issue by using two counter propagating laser beams focused to the same spot. In this case, the scattering forces cancel each other and the gradient restoring force is doubled. This trap configuration is commonly known as a Dual-Beam Dipole Trap and is discussed in greater detail in chapter 3.

The radial gradient force is plotted in figure 2.7 for the parameters listed in table 2.5. Also plotted in figure 2.7 is the weight force for a 300 nm fused silica sphere. The radial radiation restoring force dominates over the weight force allowing for a stable trapping potential along the vertical axis.

Since the Rayleigh solution provides analytical expressions, it is typically the preferred method for particles significantly smaller than the trapping wavelength. In section 2.5 we discuss numerical methods for estimating radiation forces using Mie

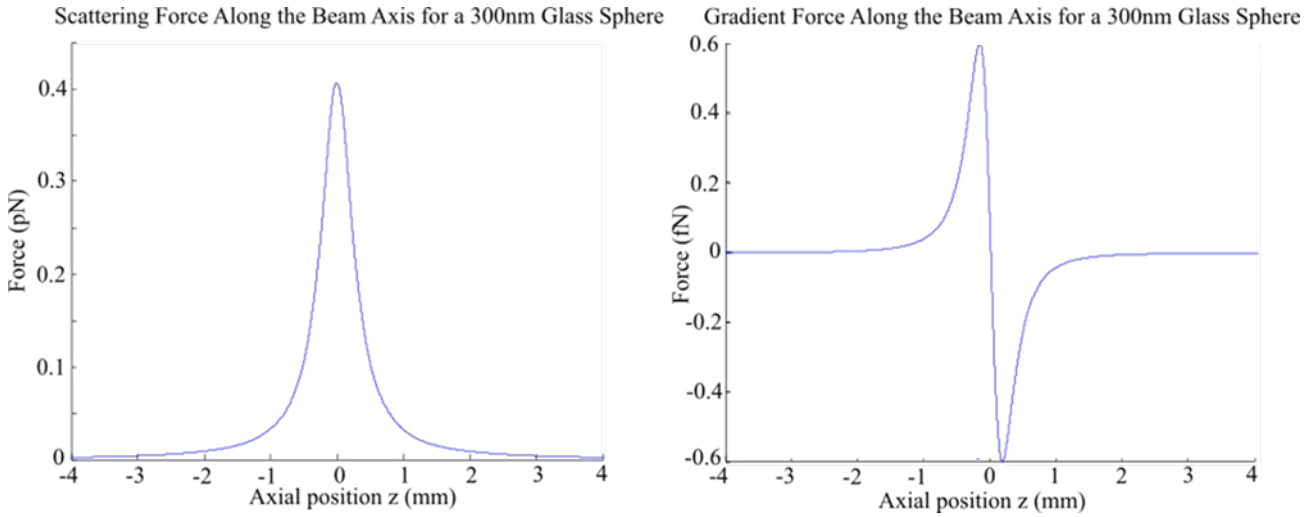

Figure 2.6: The calculated Rayleigh optical force on a 300 nm micro-sphere with a 2.2 W 1064nm laser and waist of 10 μm. A) The scattering force along the laser propagation axis. B) The gradient force along the laser propagation axis. The beam waist for this configuration is 10 μm and the Rayleigh length is .0003 m. Note the different force scales.

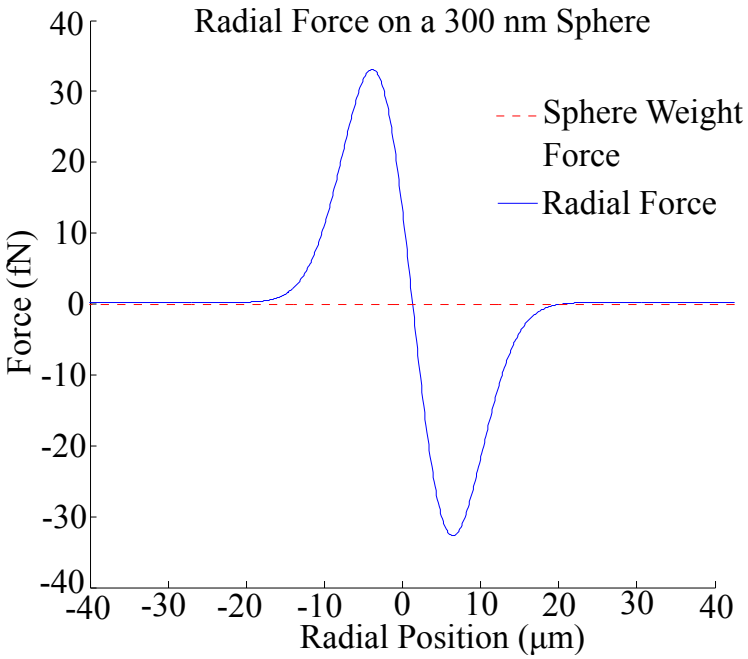

Figure 2.7: The calculated radial Rayleigh gradient force on a 300 nm micro-sphere with a 2.2 W 1064 nm laser and waist of 10 μm. The beam waist for this configuration is 10 μm.

scattering. These solutions hold true within the Rayleigh regime as well as for larger particles, but the models are significantly more complicated.

2.5 Mie Scattering Regime

For much of the work presented in this dissertation we used 3 μm spheres because they are easy to deposit into the optical trap (section 4.3.1.) We also used a 1064 nm laser for our dipole trap. This combination is well within the Mie scattering regime where $r \sim \lambda$. Several codes have been written that model Mie scattering of electromagnetic waves from spherical particles. [47, 48, 49, 50]. The results presented in this chapter were primarily computed with a modified version of a MATLAB code written by Christian Mätzler [47]. A detailed review on Mie scattering of a focused Gaussian laser beam by a spherical particle is provided by Ref. [51].

The Mie scattering solution for the radiation force is similar to Rayleigh scattering in that the radiation force results from a change in momentum of the scattered electromagnetic field. However, there is not a concise analytic solution because the incoming and radiated fields are expanded into radiating spherical vector wave functions, which necessitate high order Bessel functions. The mathematical computation is quite complex and omitted from this dissertation.

Plotted in figure 2.8 is the radiation force on a micro-sphere calculated at the laser focus for both the Rayleigh and Mie solutions as a function of sphere radius. The laser wavelength in these calculations is 1064 nm. The two solutions agree quite well in the limit $r \ll \lambda$. However, they diverge around $r = .15$ μm where $\frac{r}{\lambda} \sim \frac{1}{2\pi}$.

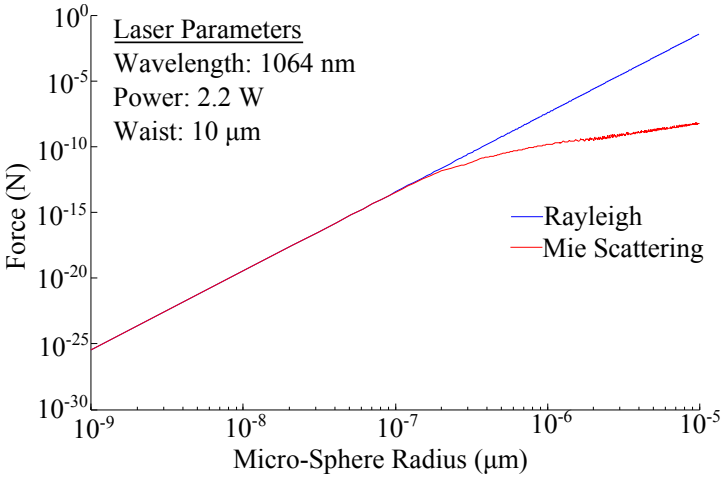

Figure 2.8: The calculated Mie and Rayleigh optical forces on a micro-sphere at the focus of a 2.2 W laser with 1064 nm wavelength as a function of sphere radius. The two theories agree very well within the Rayleigh limit.

Chapter 3

Dipole Optical Trapping

As discussed in chapter 2, the optical forces on a micro-sphere from a focused laser beam are of two types. The first type being a scattering force F_{Scat} along the axis of laser propagation $\hat{z}$. The second type is a gradient force F_{Grad} in the direction of the gradient of the laser intensity.

The intensity of a focused Gaussian laser beam is given by

$$I(r,z) = I_0 \left(\frac{w_0}{w(z)} \right)^2 e^{\frac{-2r^2}{w^2(z)}}, \tag{3.1}$$

where z is a position coordinate along the axis of propagation, r is the radial position from the beam axis, I_0 is the intensity at the beam center and w_0 is the minimum beam waist at the focus. The beam waist $w(z)$ is given by

$$w(z) = w_0 \sqrt{1 + \left(\frac{z}{z_R} \right)^2}, \tag{3.2}$$

where z_R is the Rayleigh length given by $z_R = \frac{\pi w_0^2}{\lambda}$. A micro-sphere located within the beam but off axis will experience a gradient force pushing it towards the beam axis.

Plotted in figure 3.1 is a contour plot of a Gaussian laser beam intensity in the plane perpendicular to the axis of propagation. Also plotted is the intensity gradient field.

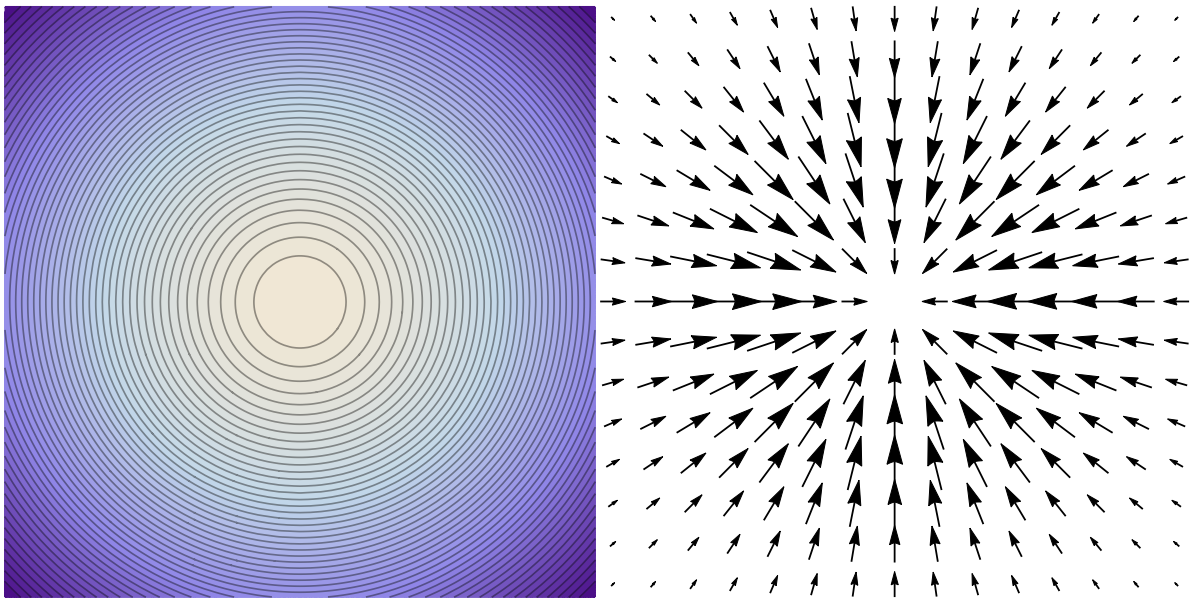

Figure 3.1: A) Contour plot of a Gaussian laser beam intensity in the plane perpendicular to the axis of propagation. B) Gradient field, ∇I, plot of a Gaussian laser beam in the plane perpendicular to the axis of propagation.

3.1 Single Beam Dipole Trap

The simplest dipole traps are formed by focusing a single laser beam with a high numerical aperture[1] (NA) lens. The minimum beam waist w_0 as a function of NA for a focused Gaussian beam is given by [52]

$$w_0 = \frac{n\lambda}{\pi(NA)}, \tag{3.3}$$

where n is the index of refraction of the medium the lens acts in. By using higher NA lenses, smaller waists are produced. When the focus of the beam is sufficiently small the gradient force is larger than the scattering force along the beam axis providing a restoring force centered on the focus. Plotted in figures 3.2 and 3.3 are the optical forces on a 300 nm sphere trapped in vacuum and air respectively. As illustrated in figure 3.2.C, a NA$\sim$ .9 is required for the magnitude of the gradient force to roughly equal the magnitude of the scattering force for a 300 nm sphere. Since the index of refraction for water is greater than the index of refraction of vacuum, a larger NA is

[1]See appendix C for a relevant description of NA

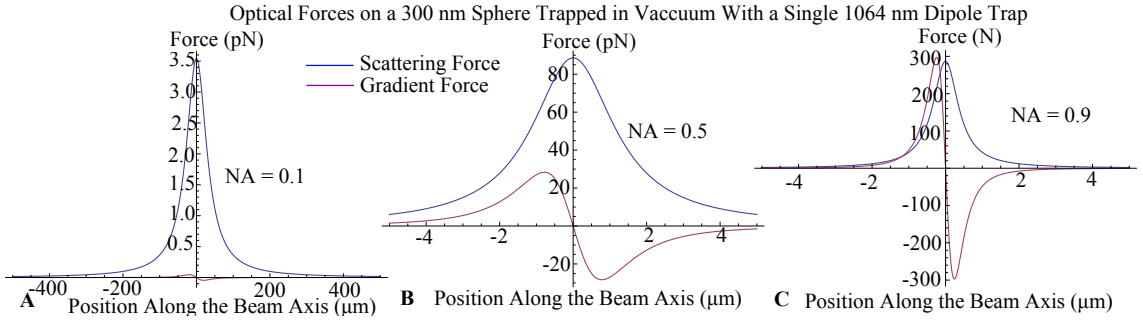

Figure 3.2: The scattering and gradient forces on a 300 nm sphere trapped in vacuum. 2.2 W of 1064 nm laser light is focused with a single lens of varying NA. The ratio of the gradient force to the scattering force increases as NA increases.

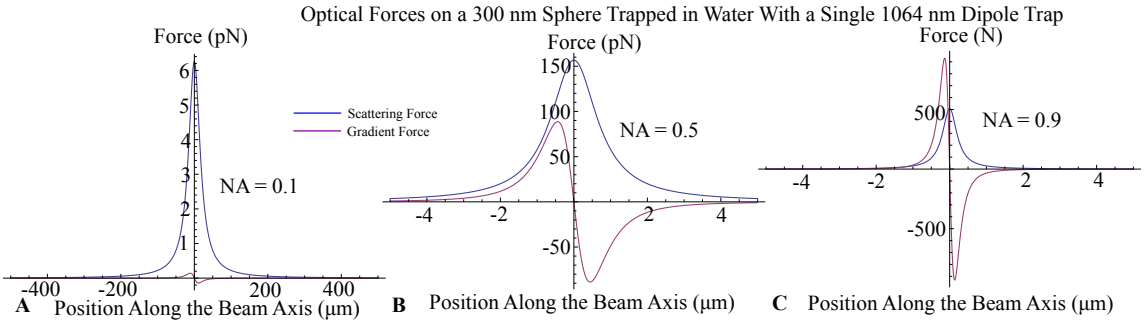

Figure 3.3: The scattering and gradient forces on a 300 nm sphere trapped in water. 2.2 W of 1064 nm laser light is focused with a single lens of varying NA. The NA used for the calculations is the NA for a lens in Air. The ratio of the gradient force to the scattering force increases as NA increases.

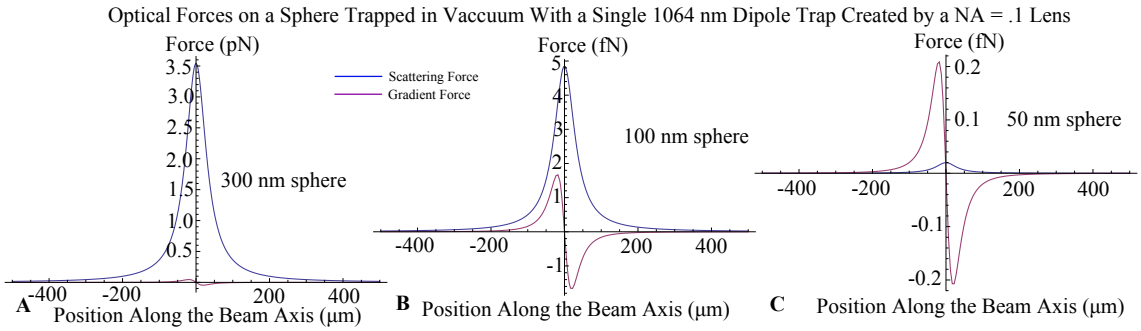

Figure 3.4: The scattering and gradient forces on spheres of varying size trapped in vacuum. 2.2 W of 1064 nm laser light is focused with a single lens with NA = 0.1. The ratio of the gradient force to the scattering force increases as the diameter of the sphere decreases.

achieved with the same lens when acting in water.

From equations 2.8 and 2.9 we see that $F_{scat} \propto a^6$ and $F_{grad} \propto a^3$. So, the ratio of the gradient force to the scattering force scales as one over the radius cubed.

$$\frac{F_{grad}}{F_{scat}} \propto a^{-3} \tag{3.4}$$

Plotted in figure 3.4 are the optical forces from a single beam 2.2 W dipole trap for micro-spheres of various diameters.

There are two drawbacks with single beam traps which prevent us from using their simple geometry in our experiments. First, the working length of most high NA lenses is typically under a few millimeters. We need a longer working length in order to trap a sphere in both a dipole trap and optical cavity with the cavity perpendicular to the dipole trap. Secondly, we are interested in trapping micro-spheres in air and vacuum. The highest NA lenses are designed to operate in liquid where the higher index of refraction is advantageous.

3.2 Dual Beam Traps

Dual beam dipole traps use two counter propagating lasers focused to the same spot. With this configuration the axial scattering forces cancel each other while the axial gradient restoring forces add to create a deeper trapping potential. We opted to use a dual beam dipole trap configuration in our experiments.

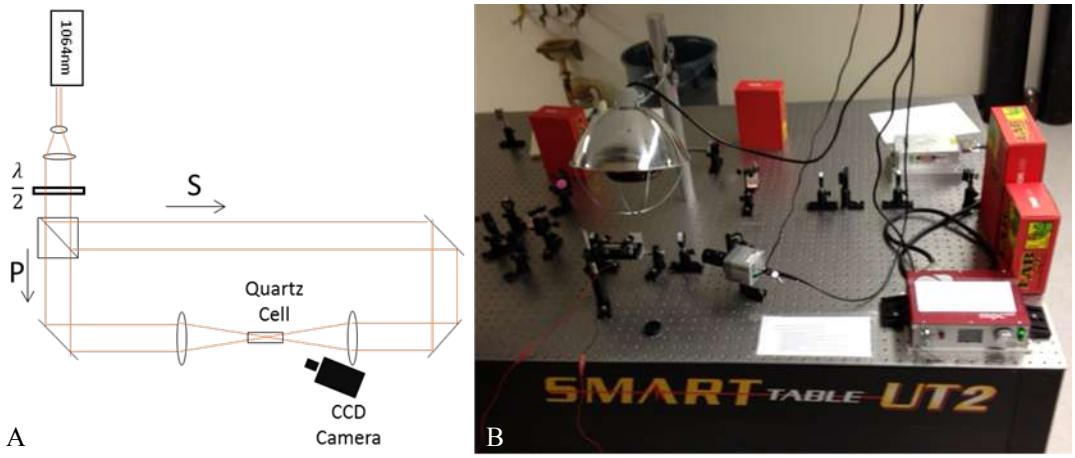

Figure 3.5: A) An optical schematic for the first proof of concept dual beam dipole trap in our lab. A 2.2 W 1064 nm laser is split into two perpendicularly polarized beams of equal power with a half-wave-plate and polarizing cube beam splitter. Two 50 mm lenses focus the beams to the same point in space. The optical trap is located at the foci of the beams. A quartz cell surrounds the trap to reduce air currents in the room and a CCD camera images the trapped sphere. B) A photograph of the first dual beam dipole trap in our lab. Note that very few optics were used.

The first dipole trap built in our lab is depicted in figure 3.5. A 2.2 W 1064 nm laser beam is expanded to ~ 1 cm in diameter and split into two perpendicularly polarized beams of equal power with a half-wave-plate and polarizing cube beam splitter. The two beams are then focused to the same position in space with 50 mm lenses. A quartz cell was place at the trap location to minimize air currents which can easily knock a micro-sphere from the trap. Figure 3.5.B is a photograph of the first trap which clearly shows the simplicity. With roughly a dozen optical components we were able to trap micro-spheres in air with ease.

3.3 Trapping potential

The magnitude of the electric field for a Gaussian beam is given by

$$E(r,z) = \sqrt{\frac{2I(r,z)}{c\epsilon_0}}, \tag{3.5}$$

where c is the speed of light, ϵ_0 is the vacuum permitivity and $I(r,z)$ is the laser intensity given in equation 3.1. The gradient force provides a trapping potential

given by

$$U(r,z) = -\frac{1}{4}\alpha E^2(r,z). \tag{3.6}$$

α is the polarizability of the micro-sphere given by

$$\alpha = 3\epsilon_0 V \frac{(\epsilon - 1)}{(\epsilon + 2)}, \tag{3.7}$$

where V and ϵ are the volume and permitivity of the micro-sphere respectively. Plotted in figure 3.6 are the trapping forces and trap potentials for a 300 nm sphere trapped in a dual beam trap with 2.2 W total Nd:YAG power and 10 μm minimum beam waists.

We define the axial force as the optical force along the dipole lasers' axis of propagation. The vertical axis is perpendicular to both the dipole trap axis and the optical table plane. The horizontal axis is parallel to the optical table and perpendicular to the dipole axis and vertical axis.

Although the intensity profile of the laser is the same along the horizontal and vertical axes, the sphere experiences the additional weight force along the vertical axis. As such, the vertical and horizontal potentials differ slightly (figure 3.6 B and D.) We refer to the effect added by the weight force of the sphere to the potential as droop.

3.4 Dipole Trap Frequency

Here we derive the the trap frequency for the dipole trapping potential given in equation 3.6. By combining equations 3.1, 3.2, 3.5, 3.6 and 3.7 we can rewrite the potential as

$$U(r,z) = -\frac{3I_0 V(\epsilon - 1)e^{-\frac{2r^2}{w_0^2\left(\frac{\lambda^2 z^2}{\pi^2 w_0^4}+1\right)}}}{2c(\epsilon + 2)\left(\frac{\lambda^2 z^2}{\pi^2 w_0^4} + 1\right)}. \tag{3.8}$$

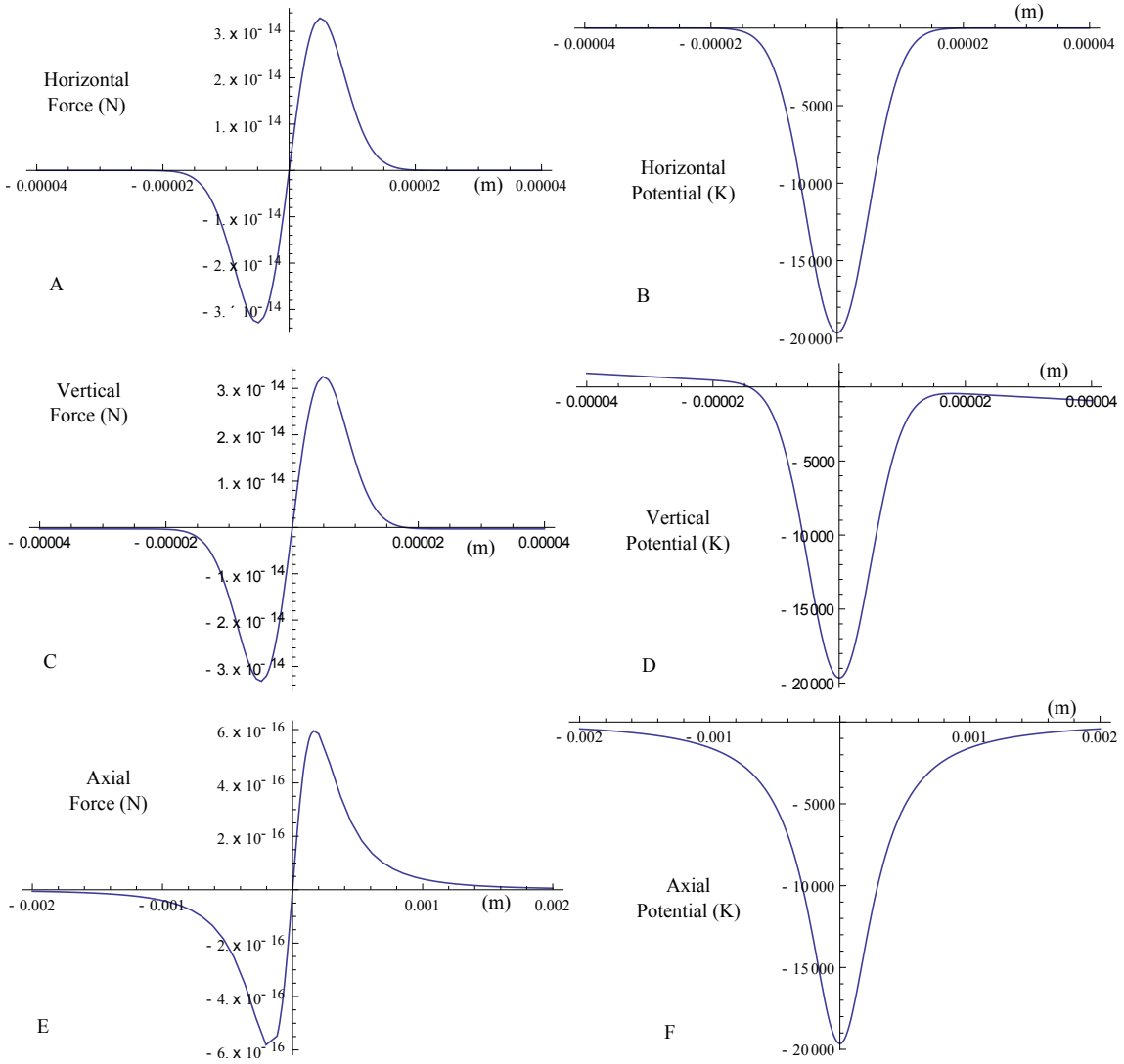

Figure 3.6: Three dimensional optical forces and trapping potentials for a dual beam dipole trap on a 300 nm sphere. 2.2 W of 1064 nm laser light was used for these calculations.

The radial force F_i at the trap center are obtained by taking the first partial derivatives of the potential.

$$F_r = -\frac{\partial U(r,0)}{\partial r}, \tag{3.9}$$

$$F_r = -\frac{6I_0 rV(\epsilon-1)e^{-\frac{2r^2}{w_0^2}}}{cw_0^2(\epsilon+2)}, \tag{3.10}$$

$$F_z = -\frac{\partial U(0,z)}{\partial z}, \tag{3.11}$$

$$F_z = -\frac{3I_0\lambda^2 Vz(\epsilon-1)}{\pi^2 cw_0^4(\epsilon+2)\left(\frac{\lambda^2 z^2}{\pi^2 w_0^4}+1\right)^2}. \tag{3.12}$$

The spring constants k_i are derived by Taylor expanding the forces F_i, looking at the first order terms and comparing them to Hook's Law: $F_i = -k_i x_i$.

$$F_r = -\frac{6I_0 V(\epsilon-1)}{cw_0^2(\epsilon+2)}r + O(r^2), \tag{3.13}$$

$$\implies k_r = \frac{6I_0 V(\epsilon-1)}{cw_0^2(\epsilon+2)}, \tag{3.14}$$

$$F_z = -\frac{3I_0\lambda^2 V(\epsilon-1)}{\pi^2 cw_0^4(\epsilon+2)}z + O(z^2), \tag{3.15}$$

$$\implies k_z = \frac{3I_0\lambda^2 V(\epsilon-1)}{\pi^2 cw_0^4(\epsilon+2)}. \tag{3.16}$$

Finally, we obtain the trap frequency ω_i by taking the square root of the spring constant k_i divided by the micro-sphere mass $m = \rho V$.

$$\omega_r = \sqrt{\frac{6I_0(\epsilon-1)}{c\rho w_0^2(\epsilon+2)}}, \tag{3.17}$$

$$\omega_z = \sqrt{\frac{3I_0\lambda^2(\epsilon-1)}{c\pi^2\rho w_0^4(\epsilon+2)}}. \tag{3.18}$$

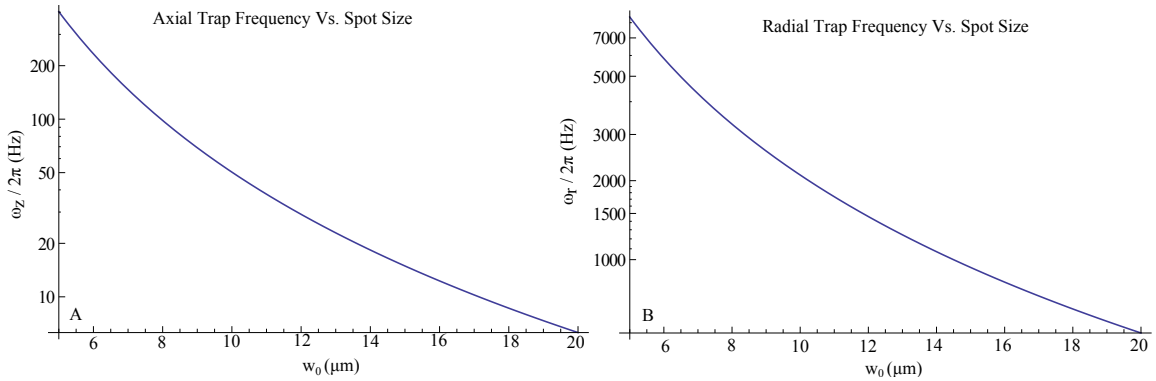

Figure 3.7: The radial and axial trap frequencies, ω_r and ω_z, for a 300 nm sphere in a 1064 nm dual beam trap with a total power of 2.2 W split evenly between the beams. As the spot size w_0 increases the trap frequency decreases for both cases.

The ratio of the radial frequency to the axial frequency for constant intensity is given by

$$\frac{\omega_r}{\omega_z} = \frac{\sqrt{2}\pi w_0}{\lambda} = \sqrt{2}\frac{z_r}{w_0}. \tag{3.19}$$

The radial frequency scales as one over the spot size and the axial frequency scales as one over the Rayleigh length for fixed intensity. As the spot size decreases, the radial intensity gradients increases near the trap center. Similarly, as the Rayleigh length decreases, the axial intensity gradient increases near the trap center. The greater the intensity gradient, the greater the restoring force on the micro-sphere which results in a greater trap frequency.

Plotted in figure 3.7 are the axial and radial trap frequencies for a 300 nm glass sphere in a 1064 nm dual beam trap with a total power of 2.2 W split evenly between the beams. The trap frequencies are plotted as a function of beam spot size which is equal for both beams. Plotted in figure 3.8 is the ratio of the trap frequencies verses spot size for the same parameters.

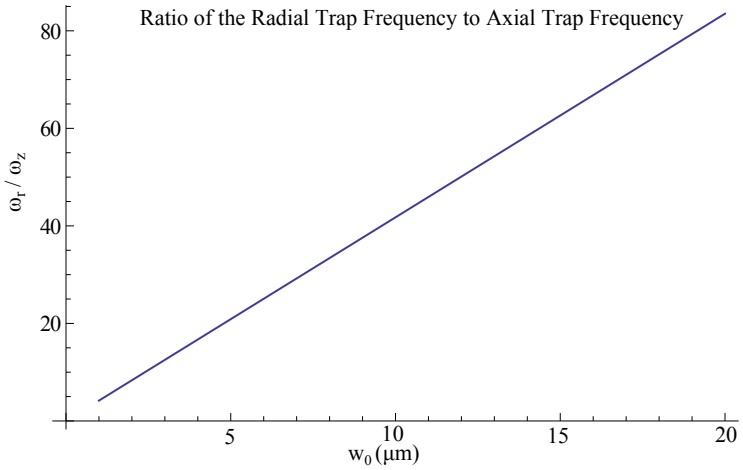

Figure 3.8: The ratio of the radial trap frequency ω_r to the axial trap frequency ω_z plotted as a function of laser spot size w_0.

3.5 Capture Velocity

The maximum velocity of a trappable sphere can be calculated by setting the potential equal to the kinetic energy of the sphere,

$$|U(0,0,0)| = \frac{1}{2}mv^2. \tag{3.20}$$

By rewriting the mass of the sphere m in terms of density ρ and volume V we get

$$\frac{1}{4}\left(3\epsilon_0 V\frac{(\epsilon-1_)}{(\epsilon+2)}\right)\frac{2I}{c\epsilon_0} = \frac{1}{2}\left(\rho V\right)v^2, \tag{3.21}$$

Solving for the velocity v we get

$$v = \sqrt{\frac{3I}{c\rho}\frac{\epsilon-1}{\epsilon+2}}. \tag{3.22}$$

For a dual beam trap with 2.2 W total Nd:YAG power and 10 μm minimum beam waists, the capture velocity is 13.2 cm/s. Plotted in figure 3.9 is the capture velocity verses trapping power and laser spot size. Since the acceleration required to launch micro-spheres is quite large, $> 10^6$ m/s^2, we cannot launch micro-spheres at high vacuum without accelerating the beads to a velocity greater than the capture velocity. Low vacuum is required because collisions with the gas in the vacuum chamber slows the micro-sphere. The lowest vacuum chamber pressure where we consistently capture micro-spheres is $\sim$5 mBar.

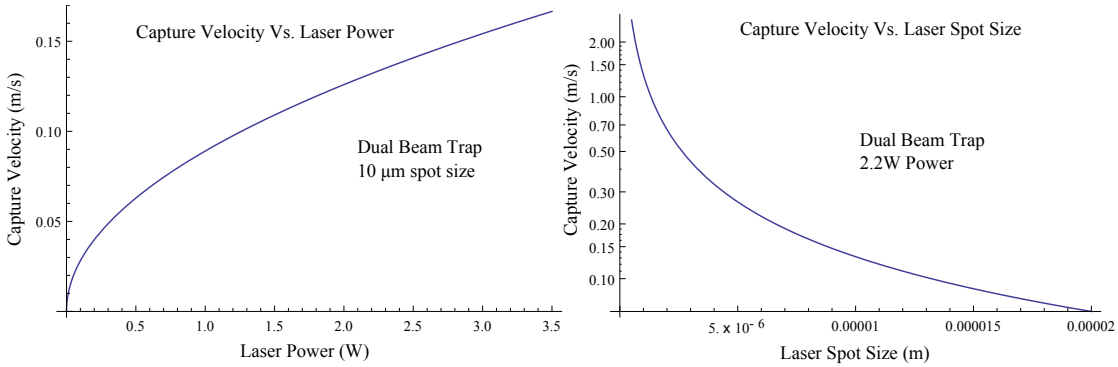

Figure 3.9: The capture velocity for 300 nm spheres trapped in a 1064 nm dual beam trap plotted as a function of laser power and laser spot size.

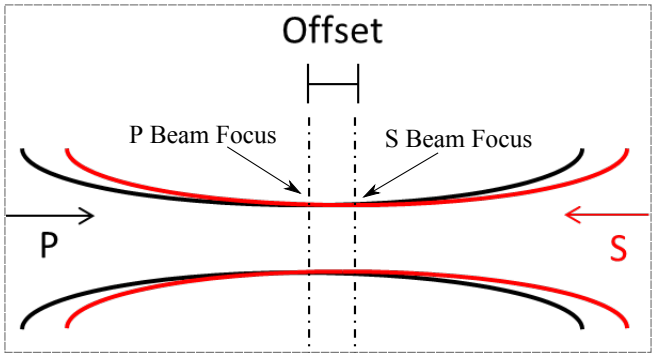

Figure 3.10: Illustration of the offset between the two foci of a dual beam dipole trap. The space between the two foci allow for small power imbalances between the two beams while maintaining a stable trap.

3.6 Dual Beam Trap with Foci Offset Axially

Typically, the scattering force is much greater than the gradient force for small NA traps as depicted in figures 3.2, 3.3 and 3.4. In order for the dual beam trap described in section 3.2 to work, the power in both beams need to be equal for the non-conservative scattering forces to cancel. If there is even a slight power imbalance between the beams the scattering force may produce an unstable trap. A simple solution to this problem is to offset the foci of the two beams as depicted in figure 3.10. This configuration allows for a "sweet spot" to exist where the scattering forces cancel somewhere between the foci. Since it is nearly impossible to get two laser beams with exactly the same power, an offset is a necessary consideration when designing a dual

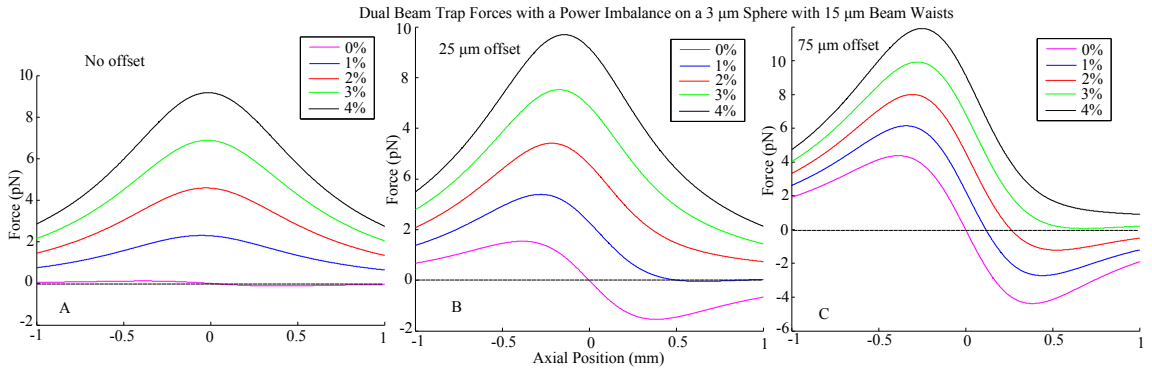

Figure 3.11: Axial forces on a 3 μm sphere from a 2.2 W 1064nm dual beam trap with 15 μm minimum waists. The power imbalance between the trapping beams varies from 0% to 4%. Power imbalance is defined so that e.g. 1% indicates 51% of the power is in the P-beam. The offset is 0 in A, 25 μm in B and 75 μm in C. As the offset increases the trap is capable of accommodating greater power imbalances.

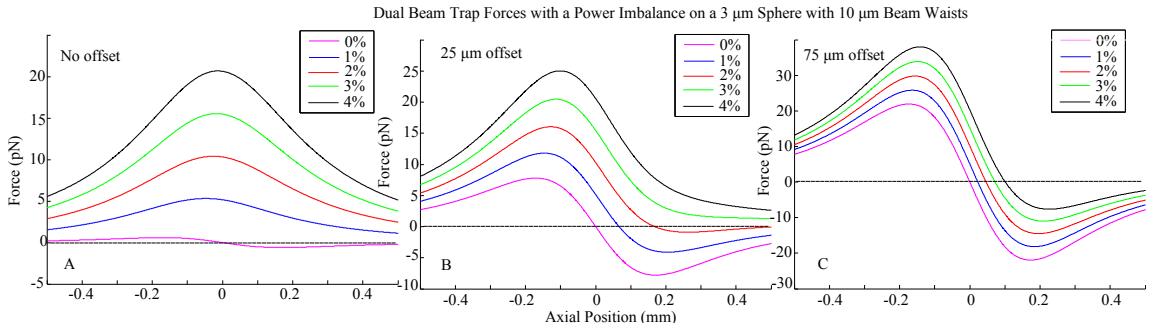

Figure 3.12: Axial forces on a 3 μm sphere from a 2.2 W 1064nm dual beam trap with 10 μm minimum waists. The power imbalance between the trapping beams varies from 0% to 4%. Power imbalance is defined so that e.g. 1% indicates 51% of the power is in the P-beam. The offset is 0 in A, 25 μm in B and 75 μm in C. As the offset increases the trap is capable of accommodating greater power imbalances.

beam dipole trap.

Plotted in figures 3.11 and 3.12 are the optical forces from a dual beam trap on a 3 μm sphere for various power imbalances and offsets. The difference between the two plots are the beam spot sizes. Figure 3.11 contains information for a trap with 15 μm waists and figure 3.12 contains information for a trap with 10 μm waists.

Plotted in figures 3.13 and 3.14 are the optical forces from a dual beam trap on a 300 nm. Figure 3.13 contains information for a trap with 15 μm waists and figure 3.14 contains information for a trap with 10 μm waists.

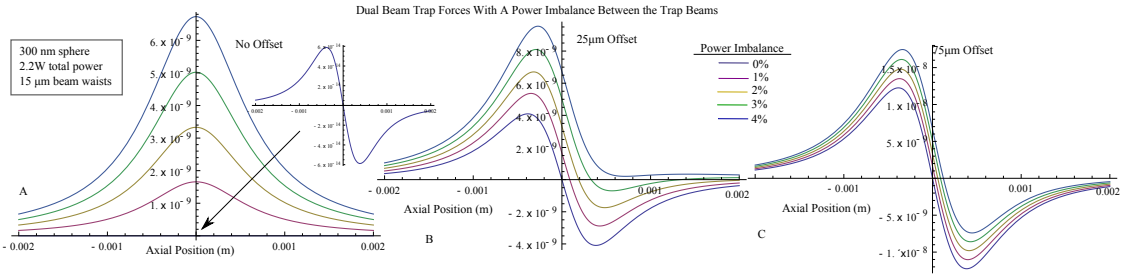

Figure 3.13: Axial forces on a 300 nm sphere from a 2.2 W 1064nm dual beam trap with 15 μm minimum waists. The power imbalance between the trapping beams varies from 0% to 4%. Power imbalance is defined so that e.g. 1% indicates 51% of the power is in the P-beam. The offset is 0 in A, 25 μm in B and 75 μm in C. As the offset increases the trap is capable of accommodating greater power imbalances.

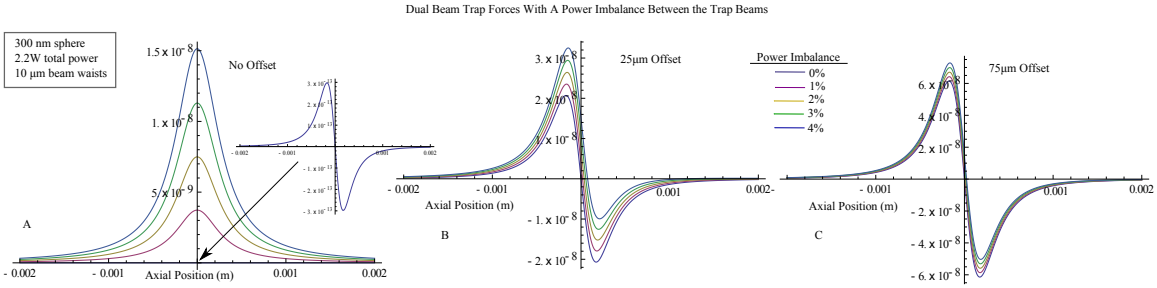

Figure 3.14: Axial forces on a 300 nm sphere from a 2.2 W 1064nm dual beam trap with 10 μm minimum waists. The power imbalance between the trapping beams varies from 0% to 4%. Power imbalance is defined so that e.g. 1% indicates 51% of the power is in the P-beam. The offset is 0 in A, 25 μm in B and 75 μm in C. As the offset increases the trap is capable of accommodating greater power imbalances.

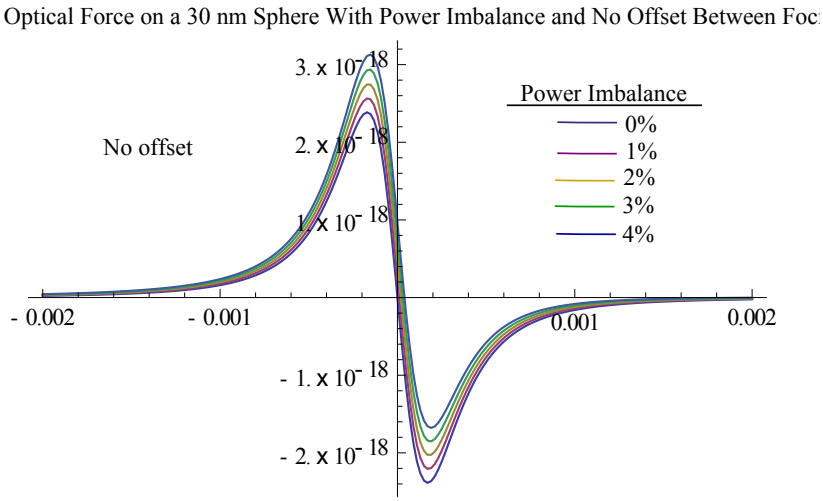

Figure 3.15: Axial forces on a 30 nm sphere from a 2.2 W 1064nm dual beam trap with 10 μm minimum waists. The power imbalance between the trapping beams varies from 0% to 4%. Power imbalance is defined so that e.g. 1% indicates 51% of the power is in the P-beam. Even though the offset is zero a wide range of power imbalances still provide a stable trap.

The first thing to note in all these figures is that when the offset is set to zero very good power balance is required to produce a stable trap. If there is even a 1% power imbalance there are no stable traps for every configuration plotted. A second effect to note is that as the beam waists decrease, we see that the traps with an offset can accommodate greater power imbalances. This is because as the beam waists decrease, the gradient force increases as a result of an increase in the gradient of the intensity. A third effect to note is that the smaller spheres can be stably trapped with greater power imbalances. Here again, the gradient force to the scattering force ratio increases as the spheres get smaller. Plotted in figure 3.15 are the trapping forces for a 30 nm sphere with various power imbalances and no offset. This figure clearly shows a stable trap with a 4% power imbalance.

Plotted in figure 3.16 is the maximum allowed power imbalance as a function of micro-sphere diameter for a trap with no offset and a 75 μm offset. The total power is 2.2 W and the beam waists are 9 μm. Power imbalance is defined so that e.g. 1 indicates 100% of the power is in the P-beam and 0 indicates a 50/50 balance between the beams. For both traps, 100% power in the P-beam allowed for a stable

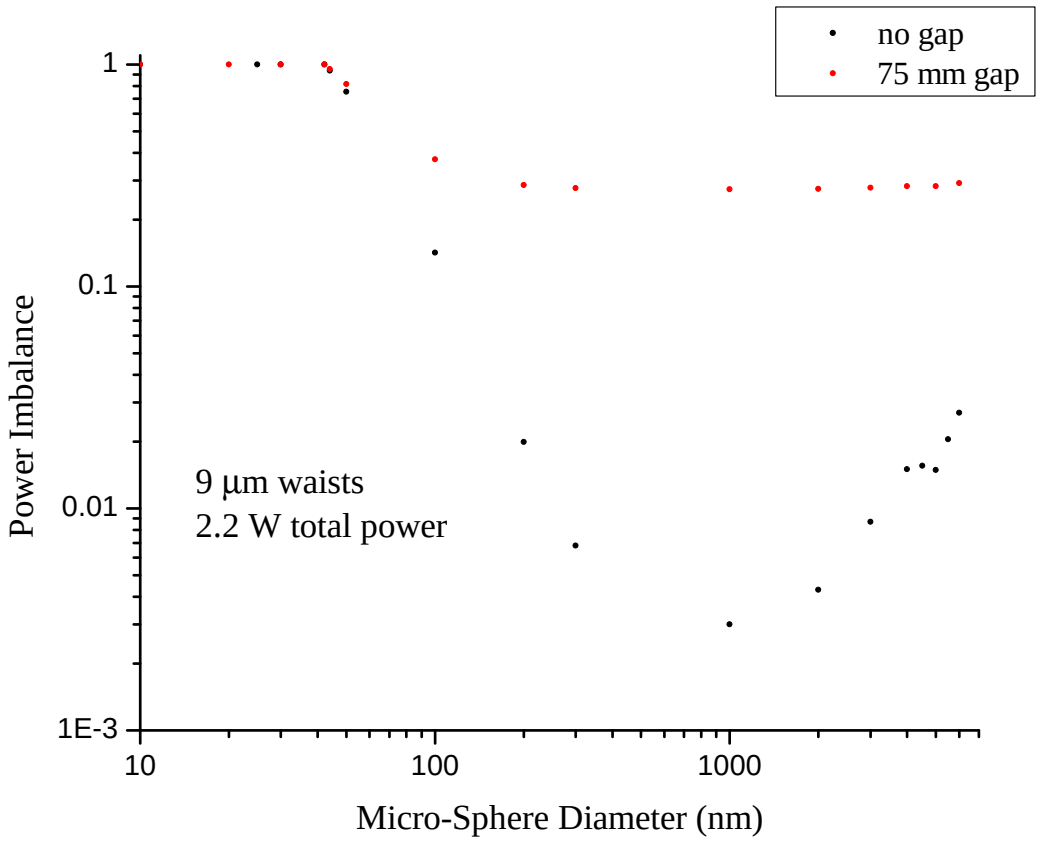

Figure 3.16: The maximum allowed power imbalance as a function of micro-sphere diameter for a trap with no offset and a 75 μm offset. The total power is 2.2 W and the beam waists are 9 μm. Power imbalance is defined so that e.g. 1 indicates 100% of the power is in the P-beam and 0 indicates a 50/50 balance between the beams.

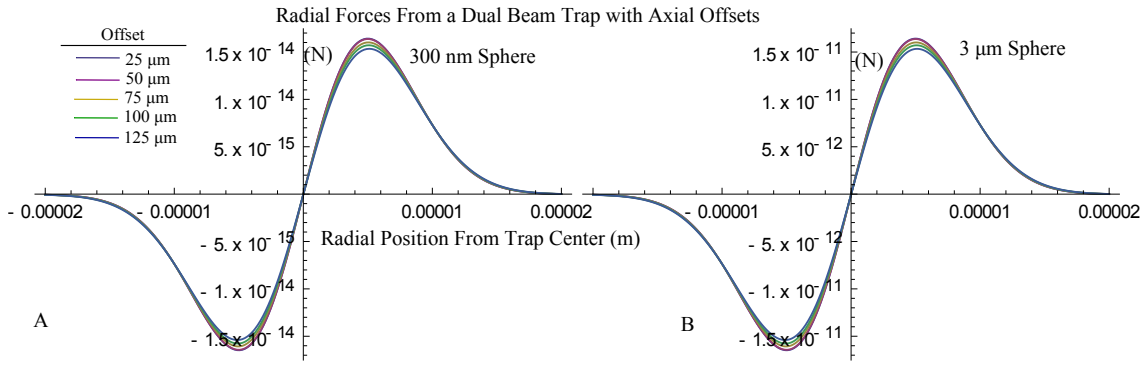

Figure 3.17: Radial forces on a 300 nm sphere (A) and a 3 μm sphere (B) from a 2.2 W 1064nm dual beam trap with 10 μm minimum waists. The axial offset varies from 25 μm to 125 μm. Note that the strength of the radial force decreases slightly as the axial offset increases.

trap for micro-spheres under 42.2 nm in diameter. This is because the gradient force dominates in this region. The maximum allowable power imbalance is at a minimum for $\sim$1 μm. The behavior of the curve above 4 μm appears odd to us and we do not have a good explanation for it. Possibly our Mie scattering code is failing as the force on the micro-sphere enter the ray optics regime.

Lastly, as the offsets get larger, the strength of the trap forces increase and the traps can accommodate greater power imbalances. This is because the scattering forces are less effective at canceling each other away from the trap center. Plotted in figure 3.17 are the radial forces on 300 nm and 3 μm spheres with various offsets. As the offset increases, the strength of the radial force decreases slightly. A typical offset used for our trap is 75 μm.

3.7 Asymmetrical Dipole Trap

In an effort to fend off thermal drift in our optics that caused misalignment of the dipole trap foci we experimented with an optical trap which we refer to as the Asymmetrical Dipole Trap; this is depicted in figure 3.18. Instead of focusing two collimated beams of equal diameter, as depicted in figure 3.5, this configuration uses collimated beams with different diameters. This produces two different spot sizes because spot

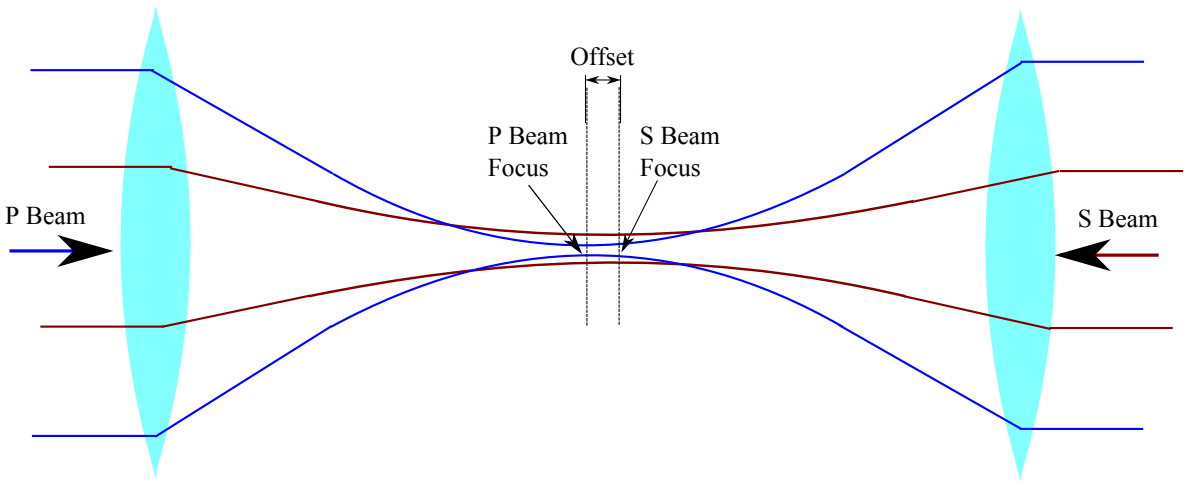

Figure 3.18: Illustration of an asymmetrical dipole trap. Two counter propagating collimated beams with different beam diameters are focused near each other with a small offset $\sim$3 μm. The focus of one beam is nested within the other beam. This configuration makes the alignment of the trap simpler. It is also resistant to small thermal drifts in the optics and power imbalances between the beams.

size is inversely proportional to the diameter of a collimated beam focused by a lens. The advantage of having different spot sizes is that the small spot can be nested within the larger spot. When one of the trapping beams drifts slightly, the effect on the trap is less noticeable when one focus is smaller than the other. This configuration also makes alignment simpler since it is not as critical to have the foci completely overlap.

Chapter 4

Experimental Setup

4.1 Vacuum System

The vacuum system was designed and built in house. Figure 4.1 is a SolidWorks drawing of our vacuum chamber. The chamber is made from an eight inch diameter

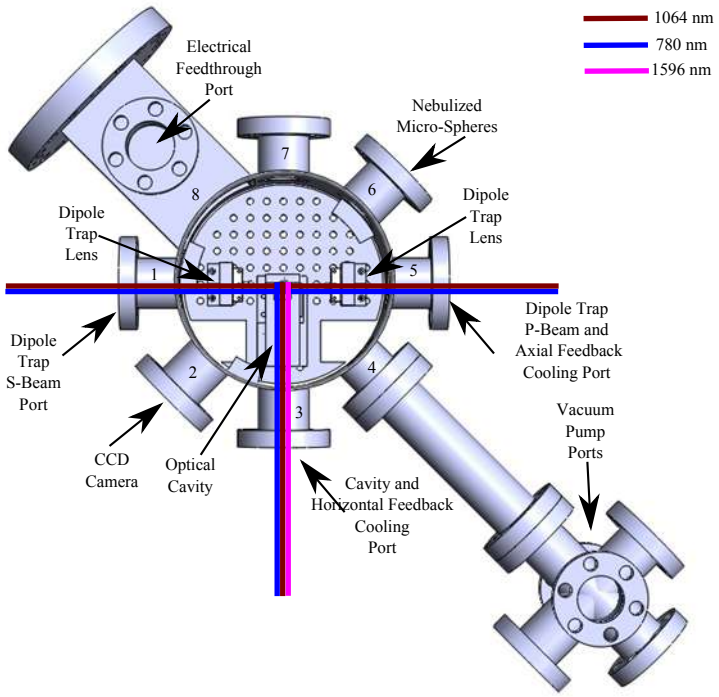

Figure 4.1: A SolidWorks rendering of the vacuum chamber used for our experiments.

stainless steel cylinder with seven 1.5 inch diameter ports and one 3 inch x 3 inch square port on the sides. We refer to the square port as the "dog house" and it houses

most of the electrical feed-throughs and part of the diving board for launching micro-spheres. Four of the ports are entries for laser beams used for trapping and cooling and have windows mounted on them with antireflective coatings for 780 nm, 1064 nm and 1596 nm. Port 1 is where the S-polarized dipole trap laser enters. The axial feedback and P-polarized trap lasers enter through port 5. The horizontal feedback and cavity lasers enter port 3. The vertical feedback cooling laser enters through the bottom port, which is not visible in figure 4.1. A six way conflat cross is attached to port 4 for attaching the vacuum pumps and the nitrogen backfill hose.

Within the vacuum chamber, there is a breadboard, figure 4.2, which holds two lenses for the dual beam dipole trap, the optical cavity and the diving board system for launching micro-spheres. The breadboard can be removed if needed. The 1 inch diameter dipole trap lenses are mounted in custom built lens mounts which are mounted on custom Newport ultra high vacuum xy stages for fine adjustment of the trap.

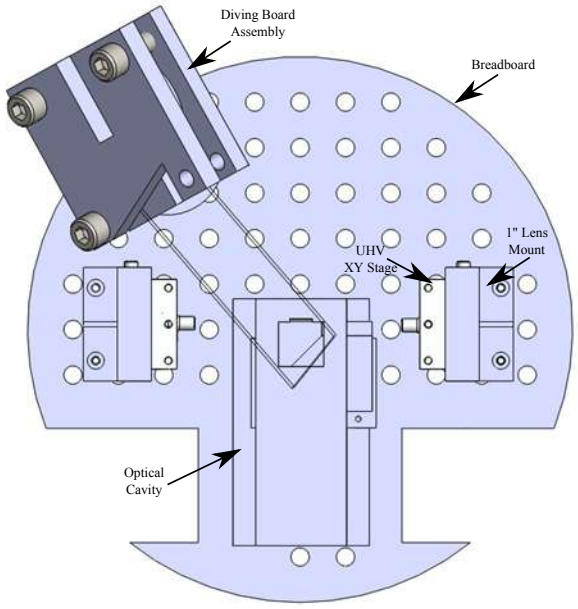

Figure 4.2: A SolidWorks rendering of the breadboard mounted within the vacuum chamber. Mounted on the breadboard are two lenses for the dipole trap, an optical cavity and the diving board assembly.

Two pumps are used to evacuate the chamber. The first pumping unit is a

Oerlikon Leybold Vacuum TURBOPUMP 80, which has both a forepump and a turbo pump. The second pumping unit is a 60 l/s VarianTriode VacIon ion pump model 911-5033. A IONIVAC ITR 90 vacuum gauge is mounted on the turbo pump which has roughly 2 meters of 2 inch bellows between it and the 6 way cross. Figure 4.3 is a photograph of the vacuum system 6 way cross. Mounted on the 6 way cross is a convectron vacuum gauge. Two valves allow chamber gas to flow towards the turbo pump. One is a large Kurt J. Lesker right angle valve which is attached to a 2 inch diameter bellows and the other is a smaller gas shut-off valve that attaches to a 7 mm diameter bellows. The smaller valve is used when sensitive control of the flow rate is required while the large valve is used to pump down quickly or at low pressures. Pumping down from atmospheric pressure with the large valve open causes too much turbulence within the chamber and results in micro-sphere loss from the chamber.

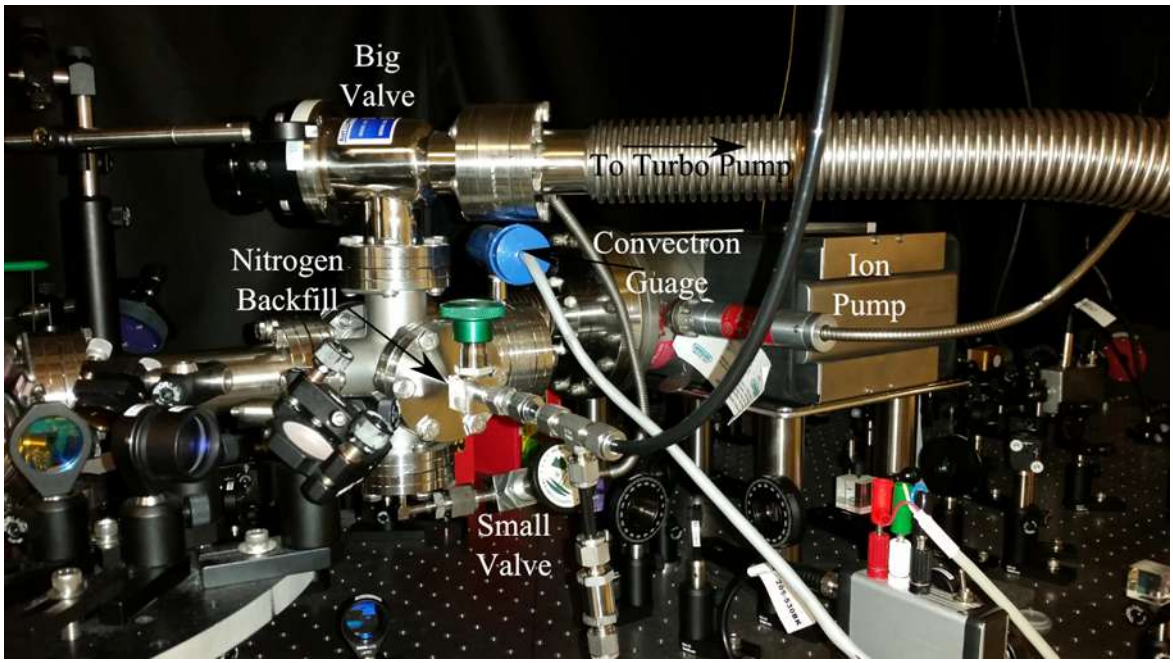

Figure 4.3: A photograph of the 6 way cross mounted on the vacuum chamber. Mounted on the cross are various valves for pumping out the chamber and backfilling it with nitrogen gas.

4.2 Dual Beam Dipole Trap

Depicted in figure 4.4 is the optical circuit for our dual beam dipole trap. A 1064 nm

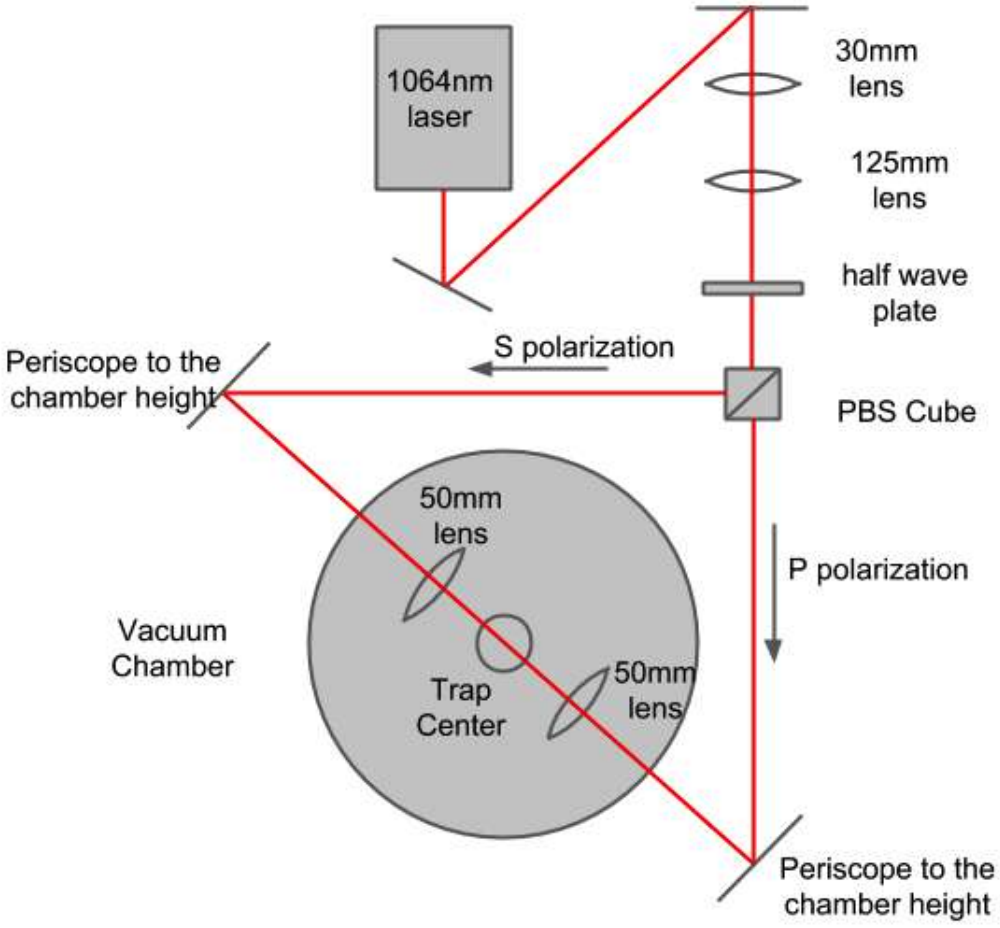

Figure 4.4: A simplified illustration if the optical layout for the dual-beam dipole trap.

Nd:Yag laser with a maximum power output of 3 W is used to create the dipole trap. The specific model of the laser is the Laser Quantum Ventus. The light is expanded with a telescope composed of a 30 mm plano-convex (pcx) and 125 mm acromat lens which brings the beam diameter to ∼9 mm. Next, the linear polarization of the beam is rotated with a $\frac{\lambda}{2}$ waveplate. The primary purpose of the waveplate is to balance the power between the S-polarized and P-polarized beams created by splitting the laser beam with a polarizing cube beam splitter (PBS). Both beams are raised to the

chamber height with a periscope. Two Thorlabs Best Form 50 mm lenses mounted within the chamber focus the beams near each other creating the optical trap. The trap laser coherence length is ∼1 cm, so interference between the S and P beams is not an issue. When the P polarized laser leaves the vacuum chamber, 1-10% of it is picked off and imaged onto quadrant photo-detector 1 for imaging the micro-sphere's motion in the horizontal-vertical plane. The S polarized light and remaining P polarized light terminate at a beam stop behind the PBS.

4.3 Bead Loading

One of the first engineering challenges we encountered was how to actually deposit a single bead into our dipole trap. After a fair amount of brain storming, we determined that producing a dry aerosol was the solution with the most bang for its buck. The system we designed was cheap to build, relatively clean for a high vacuum system and an already proven method by Dr. Tongcang Li while working on his dissertation [53] at the University of Texas in Austin under Professor Mark Raizen. However, this method proved to be less successful when launching beads smaller than 1μm, so we designed a second delivery method that produced a "fine mist" of beads and solution into the vacuum chamber. For both systems, a cloud of micro-spheres is produced which falls under gravity in a partially evacuated chamber towards the dipole trap.

4.3.1 Diving Board Method

Basic Diving Board Launching Method

The method we used to produce a dry aerosol of beads was developed in Ref. [54] and is depicted in figure 4.5. Dry beads are smeared onto the end of a glass microscope slide which is clamped onto a piezoelectric transducer. A time varying signal from a home built high current pulse generator is applied across the piezoelectric transducer such that it drives the piezoelectric transducer at a resonance which in returns drives the glass slide which shakes the beads off creating a dry aerosol. Figure 4.6 is a Solidworks drawing of the diving board system we use. The slide is at a 45° angle so

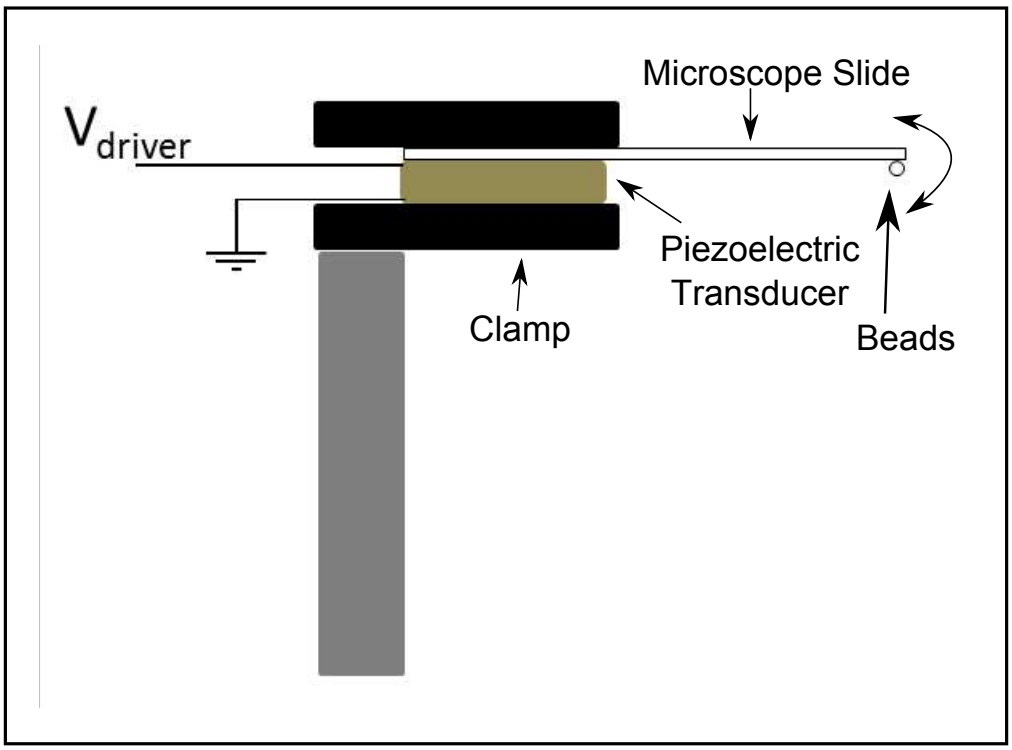

Figure 4.5: Illustration of the diving board launching mechanism. A typical glass microscope slide is clamped onto a piezoelectric transducer. At the end of the slide micro-spheres are deposited. The dominant force holding the spheres onto the slide is the van der Waals force. The piezoelectric transducer is driven at a resonance with a home built pulse power generator. In return, the slide is driven by the piezoelectric transducer knocking micro-spheres off of the slide. An aerosol of micro-spheres is produced which falls towards the optical trap under the force of gravity.

that a laser beam is reflected out of the top of the vacuum chamber for monitoring the slides motion.

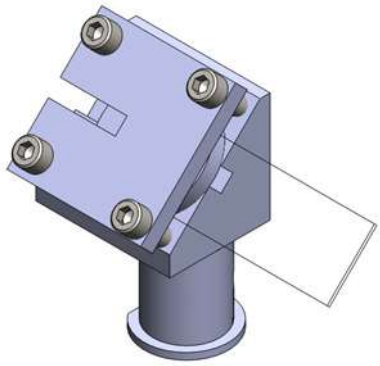

Figure 4.6: Rendering of the Solidworks mechanical drawing for the micro-sphere launching stage used in our experiments. A glass microscope slide is clamped onto a piezoelectric transducer. The slide is mounted at a 45° angle to steer a laser which monitors the slides motion.

Stiction Forces

The primary stiction force holding the beads onto the microscope slide are Van der Waals forces. The force required to flick the beads off is called the "pull-off force" and is calculated in [55, 56] for glass micro-spheres stuck together and glass micro-spheres stuck to a flat glass surface. The stiction forces are given by

$$F_{sphere-flat} = 4\pi r\gamma \tag{4.1}$$

$$F_{sphere-sphere} = 2\pi r\gamma \tag{4.2}$$

where r is the sphere radius and γ is the effective surface energy[1]. Something interesting to note about equations 4.1 and 4.2, is that the pull-off force for two spheres is half that for a sphere and flat surface. This is convenient for us because it increases the chance of trapping a single bead and not a clump of beads since it requires more force to remove a bead from the slide than the neighbor it is stuck to.

[1]Surface energy is defined as the excess energy at the surface of a material compared to the bulk. Intuitively, is makes sense that the surface of a material is less favorable energetically than the bulk, otherwise the bulk would prefer to be the surface. Typical units are mJ/m^2.

For a bead of mass m and density ρ we can rearrange equation 4.1 to calculate the acceleration a needed to detach a bead from the diving board.

$$ma = F_{sphere-flat}, \tag{4.3}$$

$$\left(\rho\frac{4}{3}\pi r^3\right)a = 4\pi r\gamma, \tag{4.4}$$

$$a = \frac{3\gamma}{\rho r^2} \propto \frac{1}{r^2}. \tag{4.5}$$

For fused silica, $\rho \sim 2300\text{g/m}^3$ and $\gamma \sim .014$ J/m^2. The acceleration required to remove various bead sizes is presented in table 4.1.

Sphere Diameter	Pull-Off Acceleration	Comments
20 μm	1.85x10^5 m/s^2	Typical for early air experiments.
3 μm	8.11x10^6 m/s^2	"Big" beads we use.
1 μm	7.30x10^7 m/s^2	
300 nm	8.12x10^8 m/s^2	"Small" beads we use.
30 nm	8.12x10^{10} m/s^2	

Table 4.1: The pull-off acceleration required to launch micro-spheres of various sizes from a glass surface.

In our lab, we typically launch 3 μm and 300 nm beads. Our diving board system is very effective at launching single 3 μm spheres. One slide with beads smeared on the end will provide single 3 μm beads for days to weeks of frequent driving. However, our system is not as effective with the 300 nm beads. We have successfully launched and trapped 300 nm beads with this method, but the flux rate of single beads leaving the diving board is very low. As such, we designed a second delivery method for smaller beads we call the Nebulizer Method. The flux of single beads is significantly higher with this method, but long pump down times are required for experiments in vacuum. This is because the experiment chamber pressure must be near atmospheric pressure. Beads can be launched with the diving board method at a few Torr.

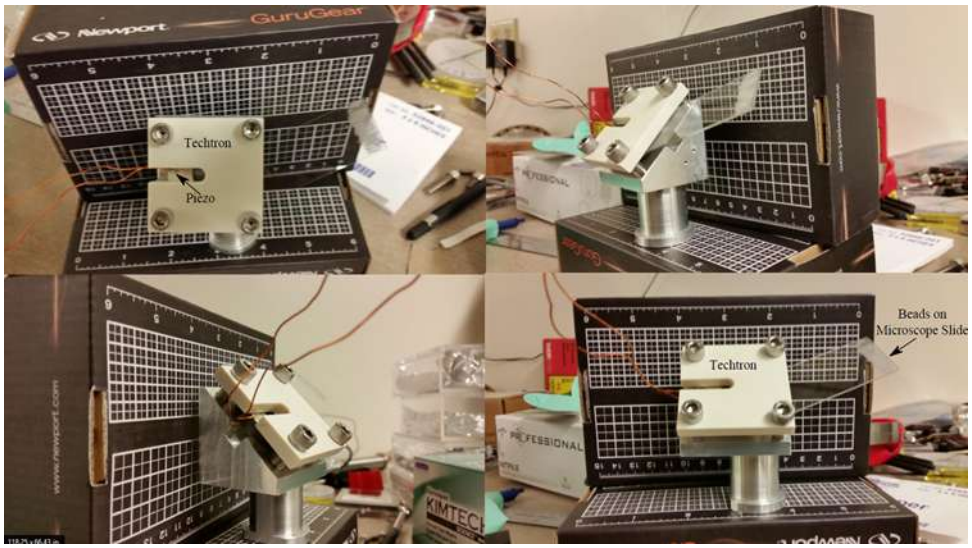

Figure 4.7: Photographs of the diving board assembly from various angles. The base is machined from a single block of aluminum and is attached to the vacuum chamber breadboard with a 1" clamping fork. The top plate is machined from a vacuum compatible plastic called Techtron which is an electrical insulator. Clamped between the base and top are a piezoelectric transducer and glass microscope slide. Micro-spheres are smeared onto the far end of the glass microscope slide.

Diving Board Assembly

Figure 4.7 contains photographs of the diving board assembly used in our experiments. A piezoelectric (piezo) ring and glass microscope slide are clamped between a Techtron top plate (white material in figure 4.7) and an aluminum base machined from a single block of aluminum. The piezo transducer is made of lead zirconate / lead titanate ceramic and manufactured by APC International Ltd. The piezo ring has an outer diameter of 38 mm, an inner diameter of 13 mm and a thickness of 6.35 mm. The top plate of the assembly is made from a high vacuum compatible plastic material called Techtron which has very low electrical conductivity. The electrical insulation of Techtron is desirable for this application to prevent electrical arcing between the grounded aluminum base and the top plate when high voltage signals are applied to the top surface of the piezoelectric transducer.

High-Power Pulse Generator

The impedance of the piezoelectric transducer is only about 12 Ω when on resonance, so a large current is needed to attain the high ultrasonic power required to accelerate the micro-spheres off of the microscope slide. Figure 4.8 contains a simplified electrical schematic for our home built high-power pulse generator which is based on a design by [53]. A high voltage (0-180 V) power supply charges a large 6.8 mF capacitor.

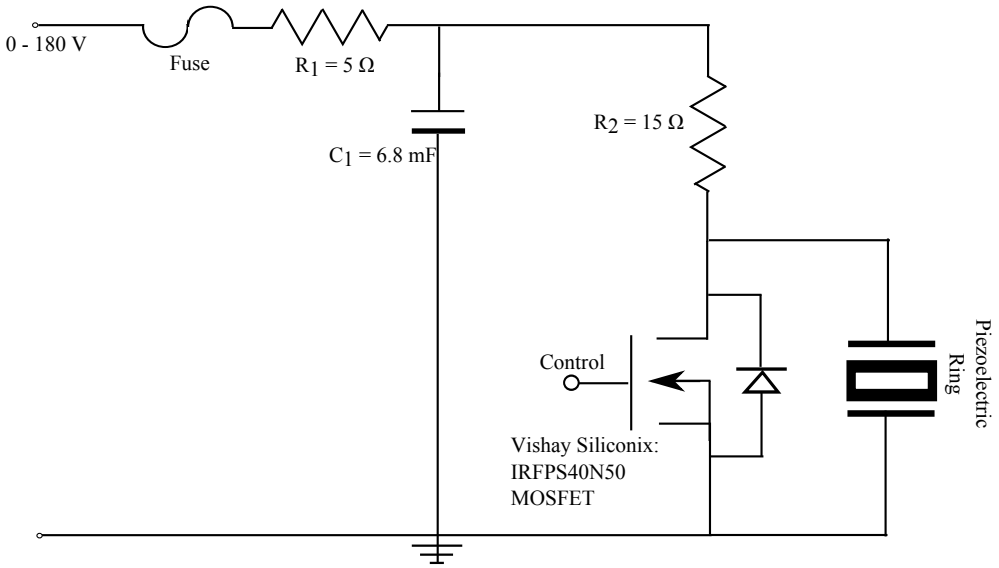

Figure 4.8: A simplified schematic of the home built pulsed power generator for driving the diving board micro-sphere delivery system.

Pulses are controlled by a high-power MOSFET (Vishay Siliconix: IRFPS40N50L) which has an input current limit of 24 A and voltage limit of 500 V. The driving signal frequency is controlled with a DS345 Stanford Reasearch Systems function generator. The input capacitance of the power-MOSFET is too high to be driven with the function generator so a high-current MOSFET (Microchip: TC4422) is used to drive the control terminal of the power-MOSFET. We found that driving the piezo at a resonance ∼140 kHz provides the largest flux of 3 μm spheres accelerated off of the microscope slide. For 300 nm spheres, driving at ∼339 Hz provides the best results.

Slide Preparation

The micro-spheres we use in our lab are commercially available from Bangs Laboratories Inc. and are suspended in a liquid solution with roughly 10% solids. The first step in preparing the diving board slide is to place a few drops of the micro-sphere solution onto a glass microscope slide. The capillary action of the liquid adds an undesirable stiction force. As mentioned in section 4.3.1, the stiction forces between micro-spheres and the glass slide can be quite substantial. In order to remove the undesired capillary force we heat the bead solution droplets to 120° C on a hotplate. Once the droplets are dry we use a fine needle to scrape a small portion of the dry micro-sphere off of the preparation slide and smear them onto the end of a launching slide. Effort is made to minimize clumping on the launching slide to increase the change of launching individual micro-spheres.

Heating

As mentioned in section 4.3.1, the flux of 300 nm beads leaving the diving board was quite low as a result of the strong stiction forces between the beads and the diving board. In order to improve the flux of smaller spheres we used a variety of incandescent and halogen bulbs to increase the thermal energy of the beads stuck to the diving board. Our results were rather subjective, but they do suggest that heating increased the flux of beads released from the diving board based on simple visual observations. In an effort to determine the effect of heating more quantitatively, we produced scanning electron microscope (SEM) samples by depositing beads onto silicon wafers with the diving board with and without heat. After looking at the samples under the SEM it was determined that more beads were deposited on the samples where heat was used which can be interpreted as an improvement in flux resulting from heating the beads on the diving board.

Although we saw an improvement in the flux of the beads with heat we also observed an increase in the kinetic energy of the beads. In simple terms, the heat lamp aided in releasing the beads from the diving board but the heat also caused the

beads to whiz around the vacuum chamber. This extra kinetic energy decreased the success rate of trapping beads.

Teflon

According to equation 4.1, reducing the surface energy γ will reduce the stiction force. The easiest and most obvious method for reducing γ is to use a diving board material with a smaller γ. Bulk glass has a surface energy anywhere from $2\frac{N}{m}$ to $4\frac{N}{m}$. Teflon (PTFE) has a surface energy of $\sim 20\frac{mN}{m}$. From equation 4.5, the acceleration required to flick a sphere off a glass surface is roughly 150 times the acceleration needed for a Teflon surface. We found that the flux of single micro-spheres launched from Teflon coated slides was noticeably improved. Also, SEM photos suggest that Teflon coated slides produce fewer clumps.

Spin Coating

When by launching the smaller 300 nm spheres, we discovered that it was significantly more likely to trap a clump of spheres than a single sphere. This is likely due to the spheres clumping on the glass microscope slide. In an effort to minimize clumping on the slide we implemented a method of spin coating slides with a diluted micro-sphere solution and centrifuge. A detailed description of the procedure is given by [26]. Figure 4.9 contains an SEM image of 300 nm spin coated onto a silicon wafer. This method provides a nice mono-layer of spheres and reduces clumping.

4.3.2 Nebulizer Method

The second bead loading method we used is depicted in figure 4.10, which we refer to as the nebulizer method. This method is very simple and has produced some nice results. The method works by producing ultrasonic waves in water with a piezoelectric transducer to create a mist of water droplets ~ 2 μm in diameter by disturbing the surface tension of the water. This technology is used extensively the medical

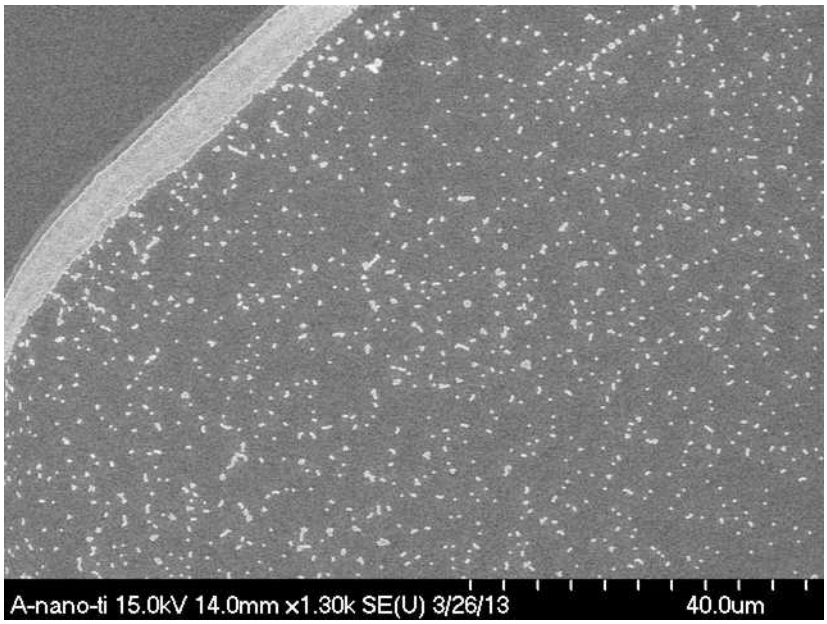

Figure 4.9: SEM photographs of 300 nm spin coated spheres on a silicon wafer.

field to deliver drugs for inhalation and in household humidifiers[2]. The piezoelectric transducer we used was the APC International LTD: 50-1011.1 because it comes mounted on a circuit board with the all the electronics needed to drive the piezoelectric transducer, other than a power supply, and the seals to attach it to a liquid reservoir.

The piezoelectric transducer requires at least two inches of water above it in order to prevent depolarization. Due to the small volume (1-2 drops of bead solution) we designed a reservoir with a thin Kapton drum head, as illustrated in figure 4.10.A. The piezoelectric transducer generates ultrasonic waves in the water within the reservoir which drive the Kapton drum head. The drum head then breaks the surface tension of the bead solution placed on the drum head. The result is a mist of beads and solution suspended in the air. This air is then blown with a fan or compressed dry nitrogen into the experiment chamber towards the optical trap.

[2]Caution should be used with nebulizer humidifiers. If regular tap water is used, the nebulizer will produce a fine aerosol of salts in the air and deposit them evenly throughout the room you are attempting to raise the humidity. This aerosol can also irritate human respiratory systems.

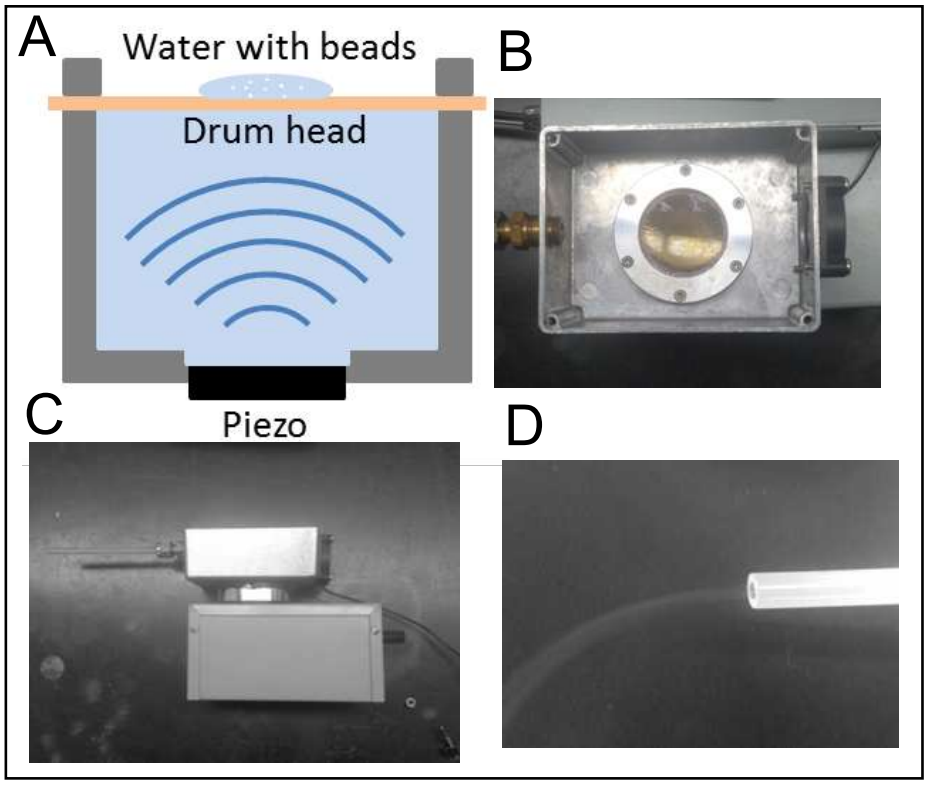

Figure 4.10: A) A piezoelectric transducer generates acoustic waves in water which drives a thin membrane drum head. Deposited on the drum head is a small volume of micro-sphere solution. The drum head breaks the surface tension of the micro-sphere solution creating a fine mist of liquid droplets with micro-spheres suspended in air. B) Birds eye view into the nebulizer system. C) Side view of the nebulizer system. D) A fine mist exiting the nebulizer system.

Nebulizer Micro-sphere Delivery Method

Figure 4.11 contains a drawing with the major components for delivering nebulized micro-spheres from the system described in section 4.3.2 into the vacuum chamber. We use dry compressed nitrogen to push the micro-spheres from the nebulizer to the chamber through a 0.25 inch Teflon hose. It is important to have a flow rate that is large enough to transport the spheres to the chamber but small enough that the speed of the micro-spheres does not exceed the trap capture velocity discussed in section 3.5. A flow meter, needle valve and leak valve provide sufficient control of the flow rate.

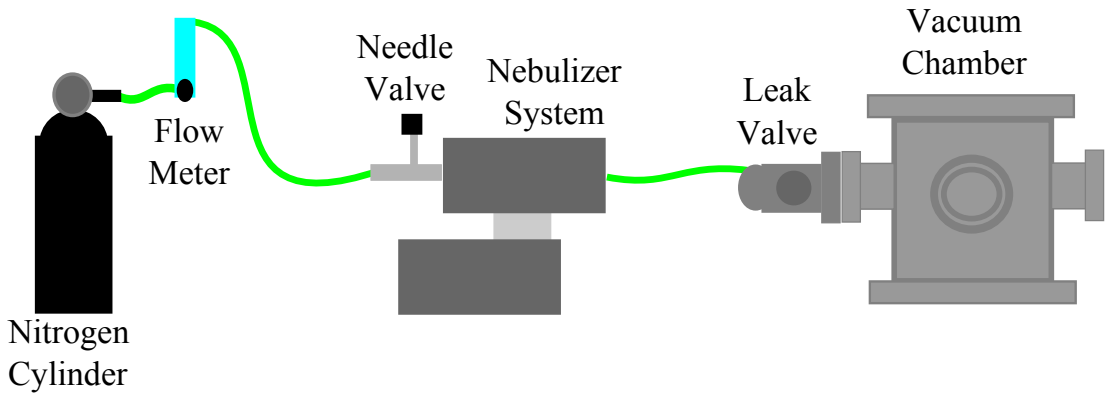

Figure 4.11: Drawing of the primary components of the nebulizer micro-sphere delivery system. Dry nitrogen pushes the nebulized mist of micro-spheres into the vacuum chamber.

The procedure for operating the Nebulizer delivery system is as follows.

- Place one to three drops of diluted micro-sphere solution on the nebulizer drumhead. This should provide enough micro-spheres for a few days of regular operations. Only add more solution when the flux of micro-spheres near the trap is insufficient.
- Fill the remainder of the drum head reservoir with isopropyl alcohol. This volume should be sufficient for a day or two. When the micro-sphere flux in the chamber is poor, first refill the drumhead reservoir with alcohol. If the flux is still poor, add more micro-sphere solution.
- Open the nitrogen chamber.
- Adjust the flow meter to roughly 0.1 liters per min.
- Adjust the needle valve so that the flow meter ball moves roughly half a mm.
- Pulse the nebulizer twice for less than a second each pulse.
- Open the leak valve slowly. Stop when micro-spheres start to scatter laser light in the chamber.

- The valves should be properly adjusted at this point. All that is required to deliver micro-spheres is to pulse that nebulizer.

The above procedure is somewhat over simplified and should be used as a starting point. As an operator gains experience with the system they will most likely develop their own preferred procedure.

Alcohol Nebulizer Solution

A major drawback of the nebulization method is that liquid is introduced to the vacuum chamber. Ultimately, we would like to pump our chamber down to ultra high vacuum. Spraying water into the chamber only makes this more difficult. By diluting the micro-spheres in isopropyl alcohol, a solvent typically used for cleaning vacuum chambers, we were successful in producing a seemingly dry aerosol of micro-spheres within the vacuum chamber. The nebulizer still creates a mist with beads suspended in alcohol droplets, but the alcohol evaporates before the micro-spheres enter then chamber. Figure 4.12 contains an SEM photograph of nebulized 300 nm micro-spheres. The image on the left is of spheres diluted in clean water and the image on the right is of spheres diluted in alcohol. The difference in concentration of micro-sphere solution between the two photos is uncertain. The photos suggest that the alcohol solution is better at producing individual spheres while the water solution produces more clumping. Both photos are the result of a single droplet. The alcohol drop is noticeably smaller and produces less residue.

4.4 Imaging Trapped Micro-Spheres

The center-of-mass motion of the micro-spheres is imaged with one of two quadrant photo-detectors (QPDs.) In our experiments, we either image the shadow of the micro-sphere or the scattered light from a micro-sphere in the trapping laser onto a QPD. Figure 4.13 contains illustrations of our imaging optics. In figure 4.13.A, part of the P-polarized dipole trap beam is picked off and imaged onto a QPD with a lens. In figure 4.13.B, light scattered from the micro-sphere is collected with a lens and

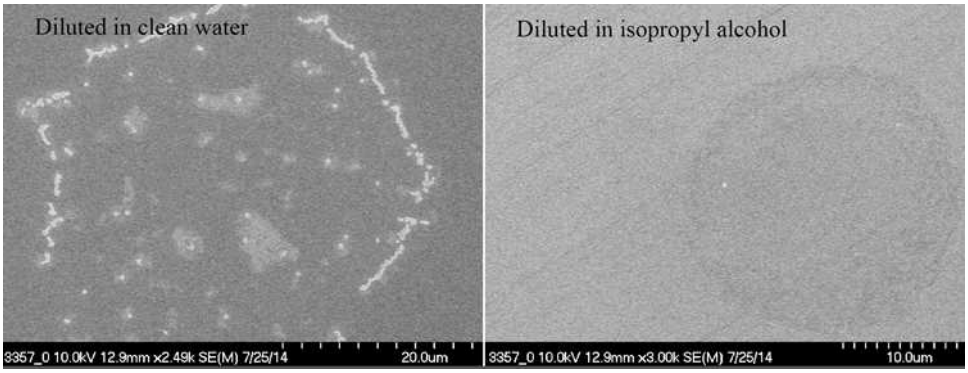

Figure 4.12: SEM photographs of 300 nm spheres deposited on a silicon wafer with the nebulizer System. The image on the left is of spheres diluted in clean water and the image on the right is of spheres diluted in alcohol.

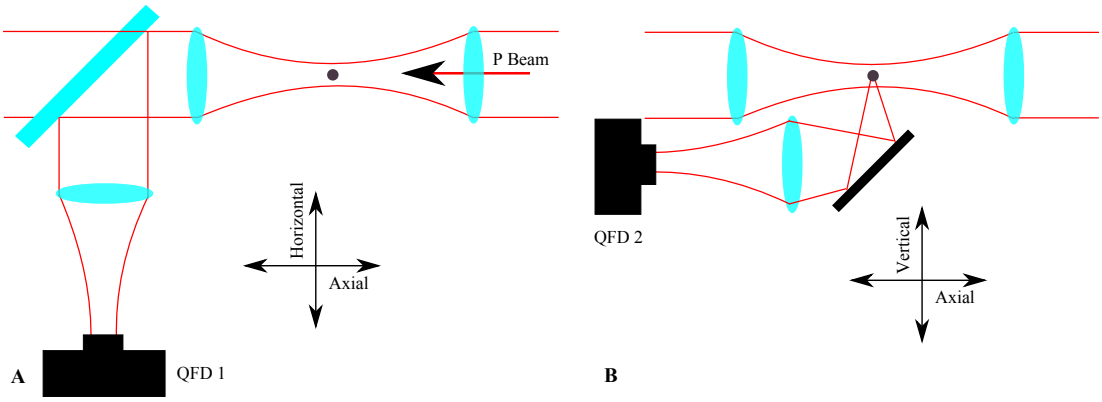

Figure 4.13: Illustration of the micro-sphere imaging optics. A) The shadow from a micro-sphere in the P-polarized trap beam is imaged onto a QPD. This image looks at the horizontal-axial plane. B) Light scattered from a micro-sphere is imaged onto a second QPD. This image looks at the vertical-axial plane. Using both QPDs we can image a micro-spheres motion in 3-D.

imaged onto a second QPD. This configuration allows us to image micro-spheres in three dimensions.

Figure 4.14 is a simple drawing of a quadrant photo-diode. A quadrant photo-diode is simply a single chip with four photo-diodes (PDs) printed on it. Each PD is given a name: A, B, C or D. Using various analog operational amplify circuits, the signals from the PDs are combined to measure the micro-sphere's motion in 2-D. Figure 4.15 contains a simplified schematic of the QPD circuit.

Each PD of the QPD has a current to voltage amplifier which produces an output

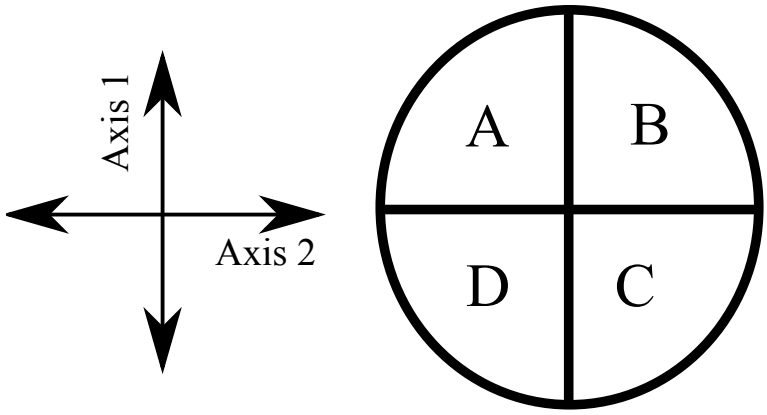

Figure 4.14: A simple drawing of the four photo-diodes (PDs) on a quadrant photo-diode chip.

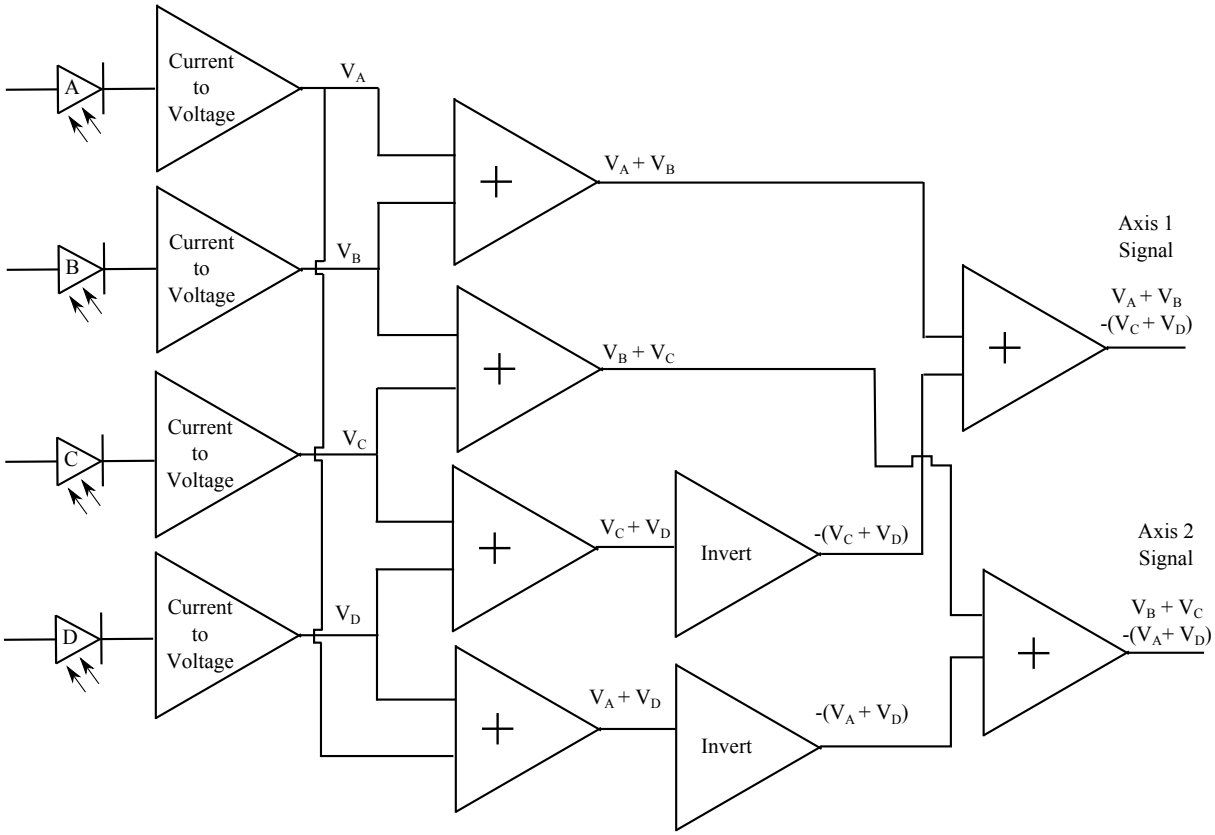

Figure 4.15: A simplified schematic of the quadrant photo-detector.

voltage V_i that is proportional to the power of light incident on the PD; where i = A, B, C, D. The signal along axis 1, in figure 4.14, is produced by first summing signal V_A with signal V_B and summing signal V_C with V_D. This provides the signal V_{AB},

which is proportion to the light incident on the top half of the QPD, and signal V_{CD}, which is proportional to the light incident on the bottom half of the QPD. V_{CD} is then inverted and summed with V_{AB} to produce the signal along axis one; given by

$$V_1 = V_A + V_B - V_C - V_D. \tag{4.6}$$

A similar sequence of operations provides the signal along axis 2, which is given by

$$V_2 = V_C + V_C - V_A - V_D. \tag{4.7}$$

Figure 4.16 contains plots of the 3-D motion of a 3 μm sphere.

QPD Alignment

We have previously defined the lab frame as the horizontal, vertical and axial axes. It is important to insure that the QPDs are aligned with the lab frame in order to get the best feedback signal and to minimize crosstalk between channels. To perform this alignment we place a cross-hair outside of the vacuum chamber where the trap laser exits, so that the shadow from the cross-hair is visible on the QPD. We then rotate the QPD so that its axis is aligned with the lab frame.

4.5 Data Collection and Analysis

The micro-sphere's motion is measured in 3-D with two quadrant photo-detectors (QPD) as described in section 4.4. The signal data is recorded on a personal computer (PC) with LabVIEW and a National Instruments BNC-2120 data acquisition device (DAQ) with a sample rate of 125 kHz. The signal from a Stanford Research Systems DS345 a function generator is also captured. Figure 4.17 is a screen shot of the LabVIEW VI we used for our data acquisition. The left most column contains fields for inputing various experimental parameters. The center contains plots of the micro-sphere's motion in 3-D. The x and y-axis extend radially from the dual beam dipole trap axis and the z-axis is along the trap axis. Since the intensity profile of the trapping lasers is symmetric about the x and y axis the trap frequencies are

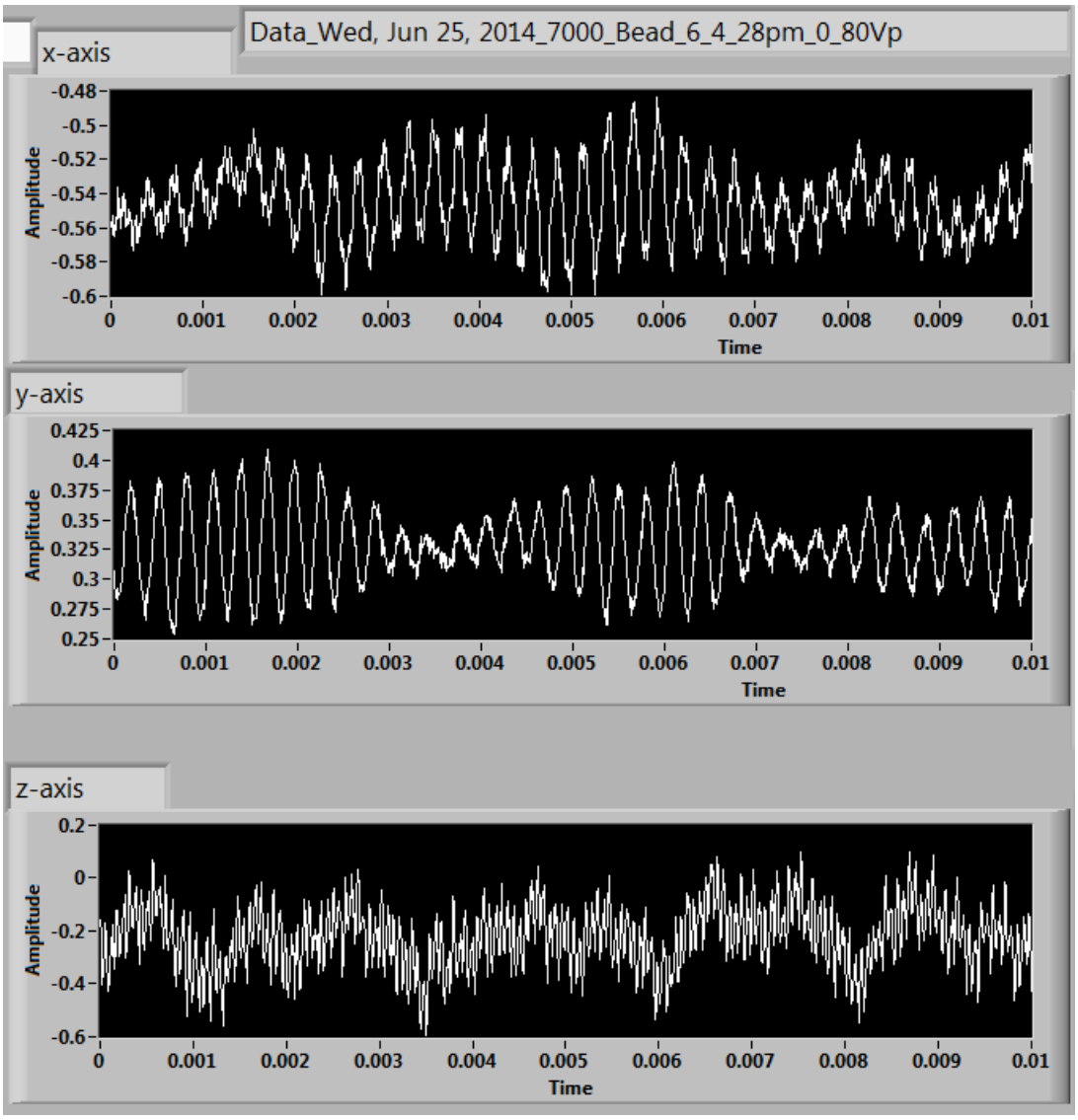

Figure 4.16: A screen shot of the 3-D motion signal of a 3 μm sphere. The x and y-axis are transverse to the trap axis. the z-axis is along the trap axis. Because of laser intensity symmetry, the frequencies of the transverse motions are similar.

roughly the same. However, the axial trap frequency is notably lower than the radial frequencies.

The LabVIEW program performs and plots a discrete Fourier transform (DFT) for all four channels. Although the DFT data is not recorded at this stage of the process, the visual of the DFT on the VI is valuable. It allows the operator to quickly determine whether a single micro-sphere or a clump of micro-spheres is trapped.

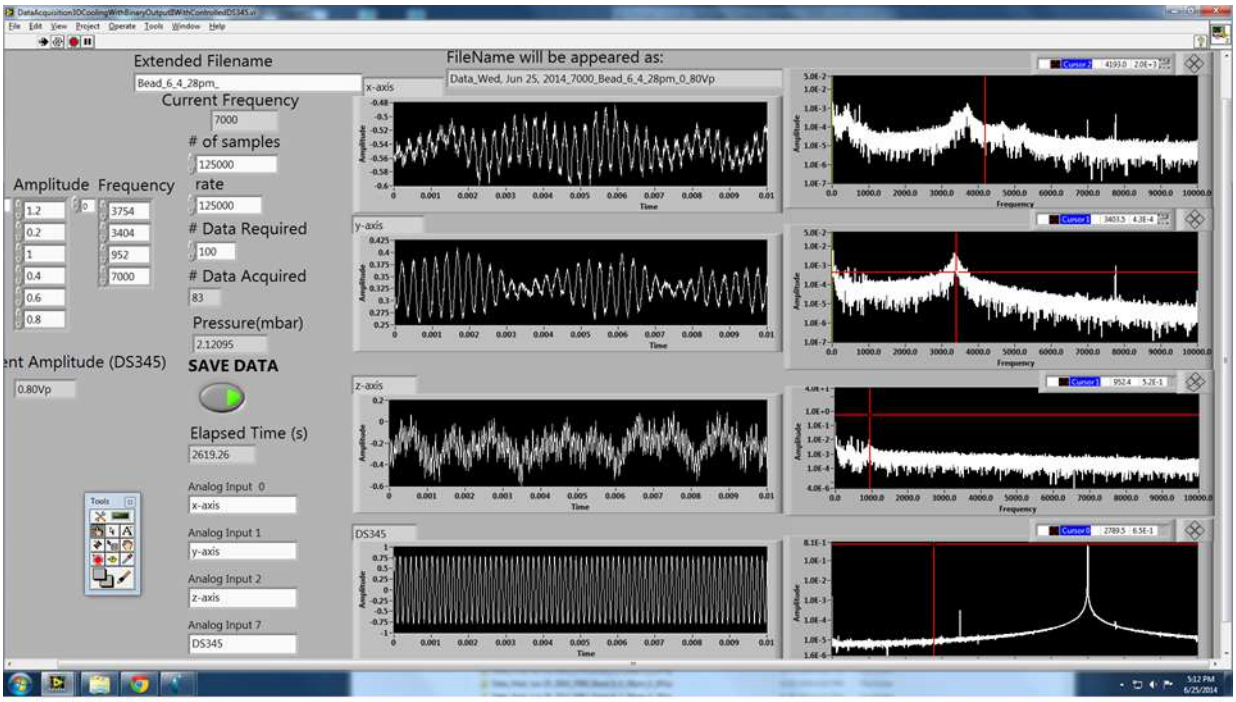

Figure 4.17: Screen shot shot of the micro-sphere motion in 3-D. The x and y axes extend radially from the dual beam dipole trap axis and the z-axis is along the trap axis. The radial frequencies are higher than the axial frequency because of the difference in the trap intensity profile.

When more than one micro-sphere is trapped, obvious rotational modes are present in the DFT.

By modulating a feedback laser or the force calibration wires at the trap frequency, the center of mass motion of a micro-sphere can be driven. This modulation signal is created with a DS345 function generator and is also plotted on the VI. Figure 6.4 contains the DFT of a 3 μm sphere driven micro-sphere.

Once data has been collected it is transfered to a second PC for analysis. We have a variety of MATLAB codes for averaging the data, performing FFT and fitting FFT peaks.

4.6 Active Feedback Cooling

4.6.1 Equation of Motion for a Micro-Sphere Optically Trapped in a Gas

The equation of motion for a classical harmonic oscillator in one dimension is given by

$$\frac{d^2x}{dt^2} + \frac{\omega_0}{Q}\frac{dx}{dt} + \omega_0^2 x = \frac{F}{M}, \tag{4.8}$$

where x is the oscillator's position, ω_0 is the resonance frequency, Q is the quality factor, M is the mass and F is an applied force. Equation 4.8 can be rewritten as

$$\frac{d^2x}{dt^2} + \Gamma_0\frac{dx}{dt} + \omega_0^2 x = \frac{F_{drive}}{M}, \tag{4.9}$$

where $\Gamma_0 = \frac{\omega_0}{Q}$ is a damping coefficient, which tends to reduce the amplitude of oscillations, and F_{drive} is a force that drives the motion of the oscillator. For an optically trapped micro-sphere trapped in thermal equilibrium with air; $\Gamma_0 = \Gamma_{air}$ is the viscous damping coefficient due to air molecules and $F_{drive} = F_{th}$ is the stochastic force from Brownian motion. So, the equation of motion for an optically trapped micro-sphere in equilibrium with a surrounding gas is given by

$$\frac{d^2x}{dt^2} + \Gamma_{gas}\frac{dx}{dt} + \omega_0^2 x = \frac{F_{th}}{M}, \tag{4.10}$$

The equation for F_{th} is provided in reference [53] and given by

$$\frac{F_{th}}{M} = \zeta(t)\sqrt{\frac{2k_bT\Gamma_{gas}}{M}}. \tag{4.11}$$

$\zeta(t)$ is a white noise process, k_b is Boltzmann's constant and T is the temperature of the gas.

It is interesting to note that Γ_{gas} is a parameter of F_{th}. As reference [53] points out, if the mechanical energy of the micro-sphere is greater than k_bT, the damping term will dominate. However, if the mechanical energy is less than k_bT, the thermal driving term will dominate. This mechanism ensures that the average mechanical energy is k_bT. This is related to the fluctuation-dissipation theorem in statistical mechanics [57].

4.6.2 Gas Damping Coefficient

Beresnev et al. [58] provide an equation for Γ_{gas}, which is given by

$$\Gamma_{gas} = \frac{6\pi\eta R}{M}\frac{.619}{.619 + Kn}(1 + c_K). \tag{4.12}$$

R is the radius of the micro-sphere,η is the viscosity coefficient, M is the mass of the micro-sphere and $K_n = l/R$ is called the Knudsen number. The Knudsen number is simply the ratio of the mean free path, l, of the gas molecules to the physical length scale of the oscillator (R.) c_K is a function of K_n and given by $c_K = (0.31K_n)/(0.785 + 1.152K_n + {K_n}^2)$.

Since the mean free path is inversely proportional to the pressure of the gas, Γ_{gas} decreases with pressure. Plotted in figure 4.18 are measured gas damping rates for two different 3 μm spheres in N_2 without feedback cooling. The damping rates were measured by fitting the position spectrum peaks to determine the oscillator quality factor Q. The damping rate is then given by $\Gamma_0 = \frac{\omega_0}{Q}$. The dashed line is

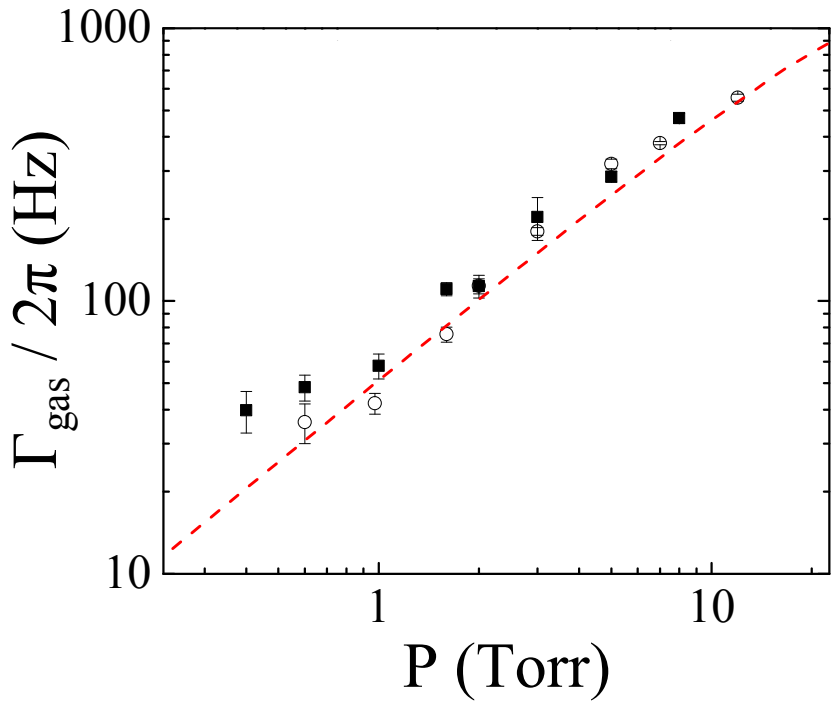

Figure 4.18: The measured gas damping rates for two different 3 μm spheres in N_2 without feedback cooling. The dashed line is the theoretical value from equation 4.12.

the theoretical value from equation 4.12. There is reasonable agreement between the measured and calculated values.

4.6.3 Optical Cooling

The center of mass (COM) temperature of an optically trapped micro-sphere can be cooled by applying a an external force, which can be written as

$$F_{cool} = -\Gamma_{cool}\frac{dx}{dt} \tag{4.13}$$

$$= -\Gamma_{cool}v(t). \tag{4.14}$$

$v(t)$ is the velocity of the micro-sphere and Γ_{cool} a cooling damping coefficient. This force is proportional to the velocity of the micro-sphere, but in the opposite direction. The equation of motion for a cooled micro-sphere in one dimension is given by

$$\frac{d^2x}{dt^2} + (\Gamma_{gas} + \Gamma_{cool})\frac{dx}{dt} + \omega_0^2 x = \frac{F_{th}}{M} = \zeta(t)\sqrt{\frac{2k_bT\Gamma_{gas}}{M}}. \tag{4.15}$$

With feedback cooling, we define the effective damping coefficient and effective temperature as

$$\Gamma_{eff} = \Gamma_{gas} + \Gamma_{cool} \tag{4.16}$$

$$T_{eff} = \frac{T_0\Gamma_{gas}}{\Gamma_{eff}}. \tag{4.17}$$

T_0 is the temperature without feedback cooling.

4.6.4 Optical Heating

If the external force in equation 4.13 were in the same direction as the velocity, heating would occur. For an external force given by

$$F_{heat} = \Gamma_{heat}\frac{dx}{dt}, \tag{4.18}$$

the effective damping coefficient would become

$$\Gamma_{eff}^{heat} = \Gamma_{gas} - \Gamma_{heat}. \tag{4.19}$$

The effective temperature is then given by

$$T_{eff}^{heat} = \frac{T_0 \Gamma_{gas}}{\Gamma_{eff}^{heat}}, \tag{4.20}$$

which is less than T_0. Experimentally, it is easy to change the sign of the driving force relative to the velocity of the micro-sphere. On many occasions we have lost trapped spheres because of this.

4.6.5 Active Feedback Cooling System

We used three intensity modulated 780 nm lasers to cool and damp the center of mass (COM) motion of trapped micro-spheres in 3-D. Figure 4.19 contains the optical circuit for our feedback cooling system. The feedback beams are oriented along the axial, vertical and horizontal exes. Each beam is power modulated with an acousto-optical modulator (AOM.) The position signals from the QPDs are phase shifted 90° to provide a signal proportional to the micro-sphere's instantaneous velocity. This signal is then used to drive the AOMs.

Plotted in figures 4.20 and 4.21 are 3-D position for a 3 μm sphere trapped at 2 mbar. Figure 4.20 is an example of our early cooling efforts. The data presented in figure 4.21 is after we refined our feedback cooling methods. The blue spectra were taken when no feedback was applied and the red spectra are with feedback cooling. For each spectra, the temperature was determined from the integrated area under the peak. The cooling ratio ξ is the ratio of the temperature without cooling to the temperature with cooling.

Plotted in figure 4.22 is the amplitude and phase of the beads motion plotted on a complex plane. For these plots, the radial distance from the origin is proportional to the amplitude of the beads motion. The angle from the real axis is the phase of the beads motion relative to a known signal provided by a Standford Research Systems DS345 function generator. The frequency of the reference signal is set to the trap frequency. Each point corresponds to a DFT of one second worth of data at 125 kHz. The red dots correspond to the signal from a bead without cooling and the black dots

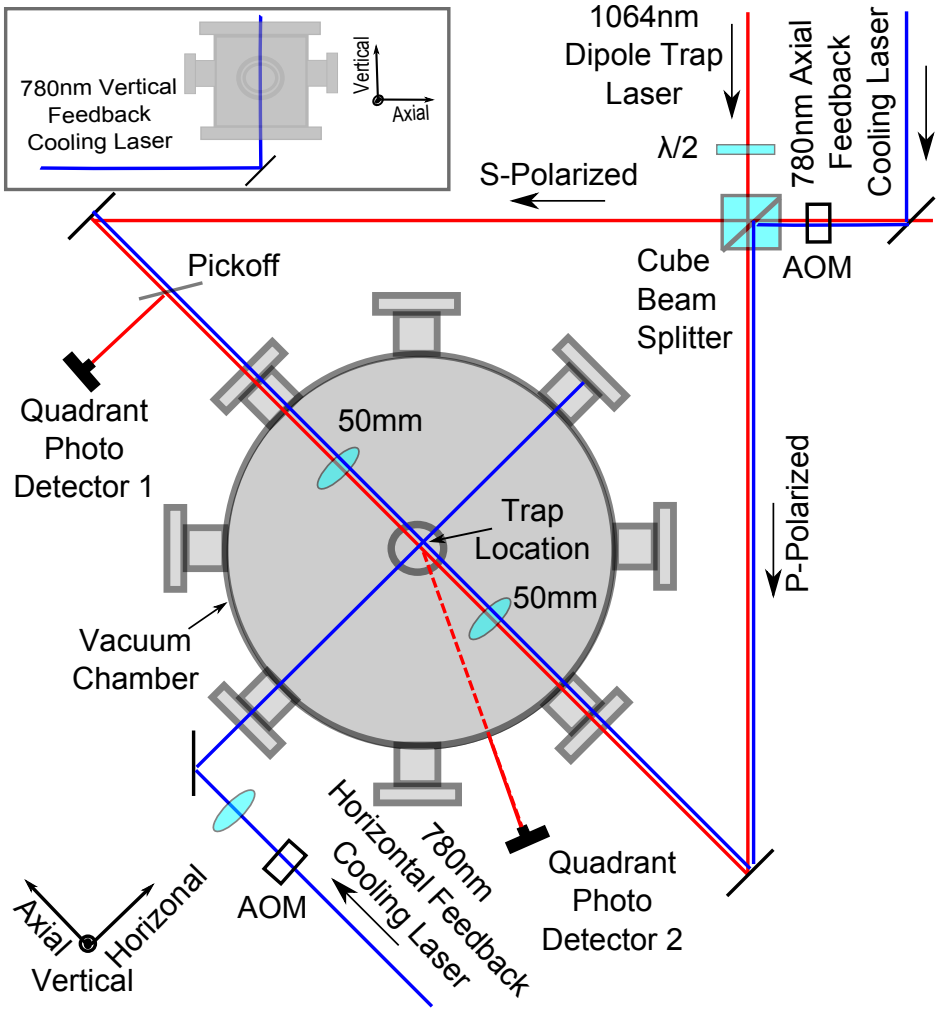

Figure 4.19: Illustration of the feedback cooling optical circuit. Three 780 nm lasers are power modulated with AOMs to damp a micro-spheres COM motion.

are with cooling. As expected, the phase is random for all data sets. When cooling is applied, the amplitudes decease while the phase remains random.

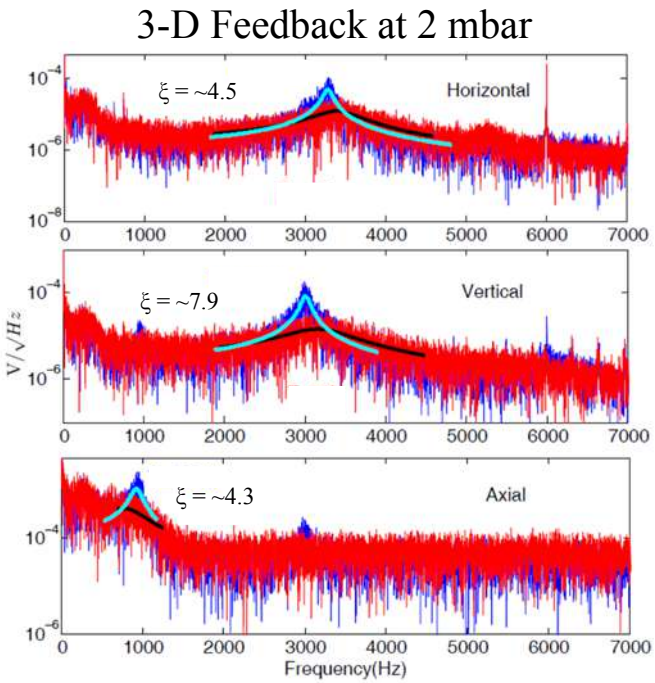

Figure 4.20: 3-D feedback cooling of a 3 μm sphere at 2 mbar

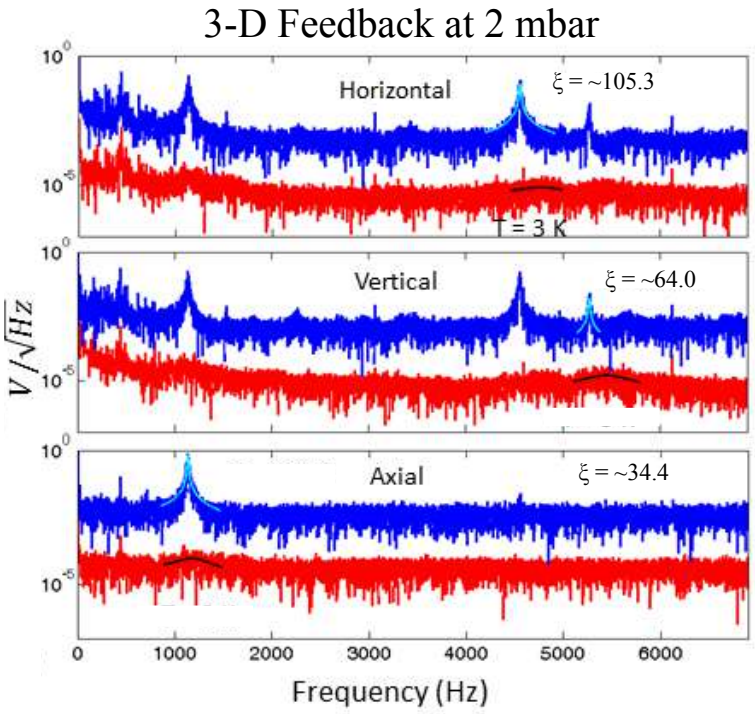

Figure 4.21: Improved 3-D feedback cooling of a 3 μm sphere at 2 mbar

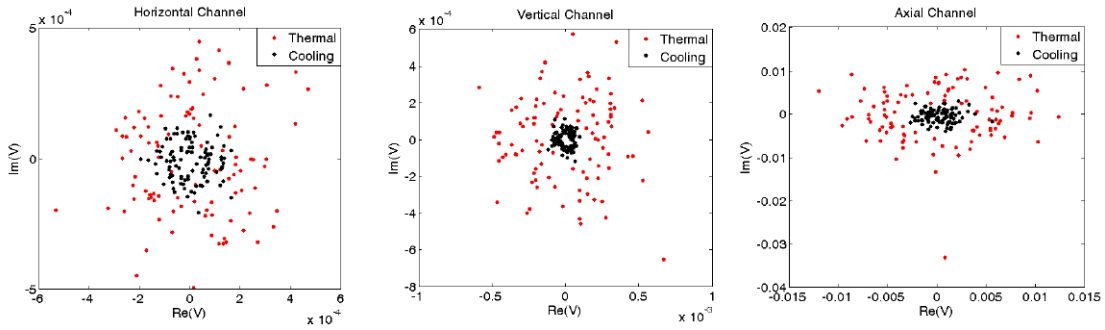

Figure 4.22: The radial distance from the origin is proportional to the amplitude of the beads motion. The angle from the real axis is the phase of the beads motion relative to a known signal provided by a Standford Research Systems DS345 function generator. The frequency of the reference signal is set to the trap frequency. Each point corresponds to a DFT of one second worth of data at 125 kHz.

Chapter 5

Laser Trapping and Cooling at High Vacuum

When the vacuum chamber pressure is above 1 Torr, we can easily keep a micro-sphere trapped without feedback damping. However, feedback damping is required for pressures below 1 Torr. Plotted in figure 5.1 are the average pressures micro-spheres are lost at as a function of trapping laser intensity without feedback damping. Each point represents an average of 5 micro-spheres. For intensities greater than 4 x 10^9 W/m^2, the loss pressure increases rapidly. However, for intensities below this value, the loss pressure is relatively constant. As discussed in chapter 3, the trap potential depth increases linearly with intensity. So, one would expect the loss pressure to decrease as intensity increases. The fact that this does not occur can be partially explained by the non-conservative scattering force from the trap laser [59, 60] and radiometric forces from uneven heating of the sphere's surface [38, 61].

5.1 Non-Conservative Trapping Forces

Instabilities can arise from the non-conservative scattering force discussed in chapter 2, because it is very difficult the achieve perfect anti-parallel alignment of the dual-beam dipole trap. We have observed cyclic motion of micro-spheres when alignment was poor. Figure 5.2 is an illustration of a dual-beam trap with a radial offset between the counter propagating beams.

A micro-sphere trapped within this configuration will have a cyclic component

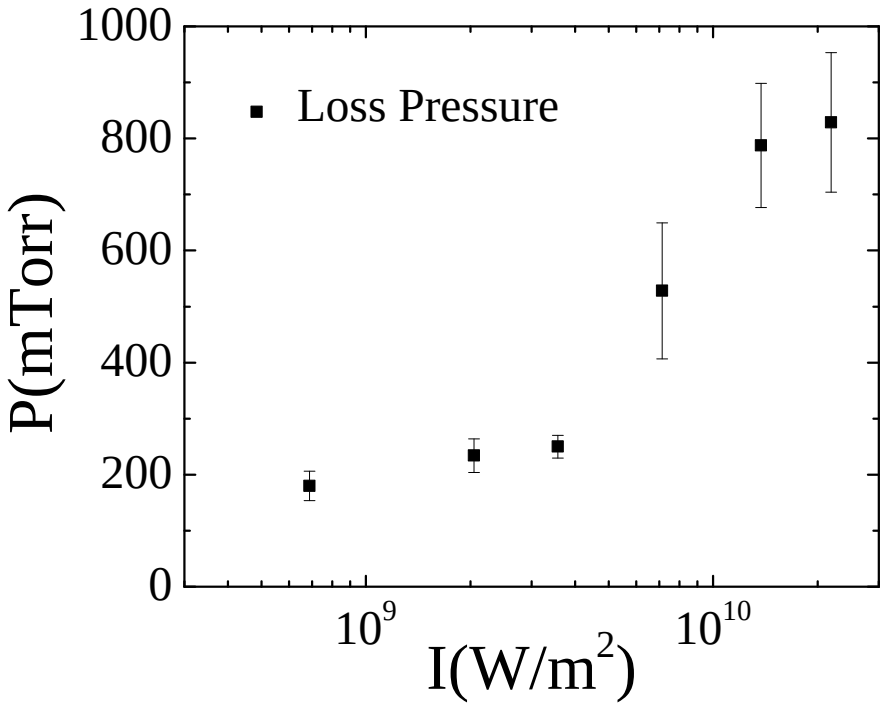

Figure 5.1: The average chamber pressure when micro-spheres are lost as a function of laser intensity. Each point represents the average loss pressure for 5 micro-spheres at a given intensity. The loss pressure increases rapidly for intensities greater than 4 x 10^9 W/m^2.

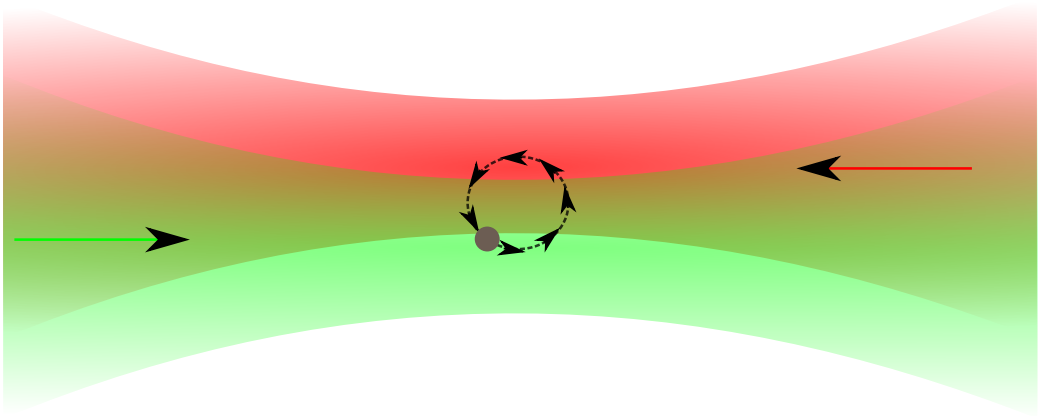

Figure 5.2: An illustration of the possible cyclic motion of a micro-sphere due to poor trap alignment.

to its motion. This motion is easily detected with our imaging system as additional rotational modes in the position DFT. In an effort to minimize these instabilities, we

use a mirror mounted on two piezo-electric (PZT) transducers to fine-tune the steering of the S-polarized trap beam, which is not the beam used for imaging. Figure 5.3 contains three screen shots of the position DFT for the same micro-sphere. The images differ only by the voltage across the PZT (V_{PZT}.) For this particular trap

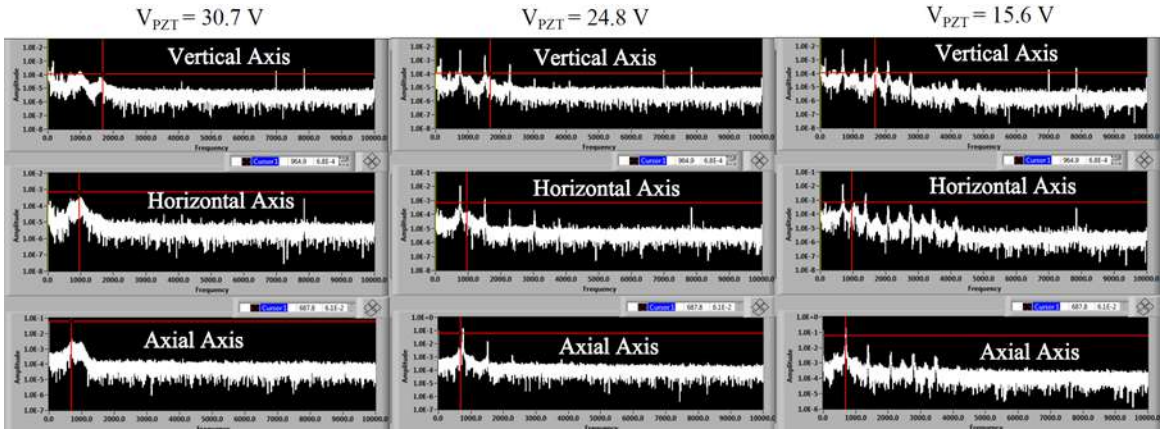

Figure 5.3: DFT power spectrums for a trapped micro-sphere with slight trap misalignment. V_{PZT} is the voltage across a PZT mounted mirror used for fine tuning trap alignment. When the trap alligment is off, sharp peaks appear in the DFT. These peaks are the result of undesirable rotational modes of the micro-sphere's motion.

alignment, the best alignment is when $V_{PZT} = 30.7$ V. By changing the voltage to $V_{PZT} = 24.8$ V, the trap is intentionally misaligned slightly causing sharp peaks to appear in the DFT. The extra peaks are the result of the new cyclic and rotational motion of the micro-sphere. Setting $V_{PZT} = 15.6$ V causes the trap to be even more misaligned and more peaks are viable in the DFT.

5.2 Radiometric Forces

The micro-spheres we use have a finite optical absorption. As such, increasing the trapping laser intensity increases the surface temperature of the micro-spheres. As gas molecules collide with the micro-sphere, they carry away more kinetic energy than they had before the collision. When heating of the micro-sphere is uneven, due to material impurities, surface imperfections or the laser intensity gradient, currents in the gas are created near the micro-sphere. If the currents are great enough, the

sphere can be lost from the trap. As the laser intensity increases, so does this effect; which partially explains the behavior in figure 5.1.

During his earlier work, Arthur Ashkin argued in Ref. [38] that these instabilities are at a maximum when the mean free path l of the surrounding gas is similar to the length scale as the micro-sphere. We define the pressure at which the $l \sim r$ as the mean free path pressure P_0. Plotted in figure 5.4 is P_0 as a function of micro-sphere diameter $2r$. For a 3 μm sphere, the MFP pressure is $\sim$ 20 Torr. Experimentally, we

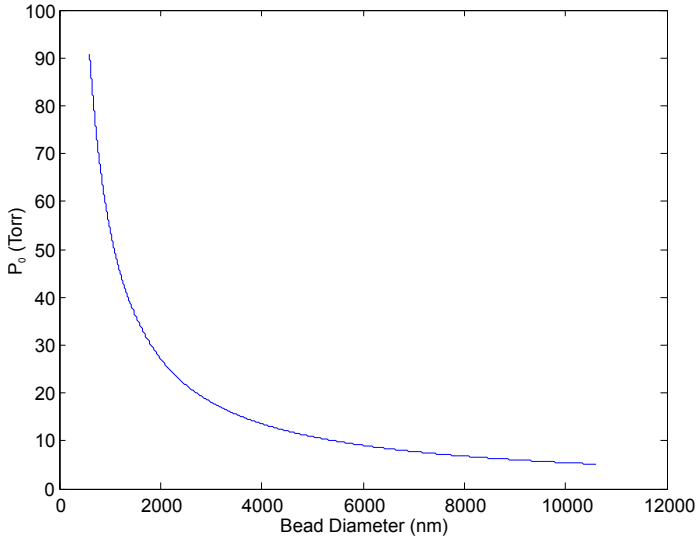

Figure 5.4: The mean free path pressure P_0 plotted as a function of bead diameter. According to Ref. [38], radiometric forces should be dominant at this pressure.

have found that the radiometric instabilities are only a nuisance below $\sim$1 Torr and that it is relatively easy to keep a 3 μm sphere trapped at 20 Torr indefinitely. In order to better understand this, we can parameterize the micro-sphere absorption as the imaginary part of the complex permitivity of the sphere.

The complex permitivity is given by

$$\epsilon = \epsilon_1 + i\epsilon_2. \tag{5.1}$$

The real part, ϵ_1, is parameterizes the energy stored within the medium. The imaginary part, ϵ_2, parameterizes the absorption or dissipation of energy within the medium.

In thermal equilibrium, the sum of the power absorbed from the trap laser and blackbody radiation from the environment must equal the sum of the power lost to gas collisions and emitted through blackbody radiation.

$$P_{bb}^{abs} + P_{laser}^{abs} = P_{bb}^{rad} + P_{col}^{rad}, \tag{5.2}$$

The Stefan-Boltzmann law provides the blackbody power absorbed from the environment and radiated, which is given by

$$P_{bb}^{abs} = \varepsilon\sigma(4\pi r^2)T^4, \tag{5.3}$$

$$P_{bb}^{rad} = \varepsilon\sigma(4\pi r^2)T_{int}^4, \tag{5.4}$$

where ε is the emissivity of the blackbody, σ is the Stefan-Boltzmann constant, r is the sphere radius, T is the temperature of the external environment and T_{int} is the internal; temperature of the micro-sphere. Ref. [62] provides a solution for P_{laser}^{abs} and P_{col}^{rad}

$$P_{laser}^{abs} = \frac{12\pi I_0 V}{\lambda} Im\left[\frac{\epsilon_1 + i\epsilon_2 - 1}{\epsilon_1 + i\epsilon_2 + 2}\right], \tag{5.5}$$

where I_0 is the laser intensity, V is the sphere volume and λ is the laser wavelength.

$$P_{col}^{rad} = -\alpha_g\sqrt{\frac{2}{3\pi}}(\pi r)^2 P v_{rms}\frac{\gamma_{sh}+1}{\gamma_{sh}-1}\left(\frac{T_{int}}{T} - 1\right), \tag{5.6}$$

where P is the background gas pressure, v_{rms} is the gas root-mean square speed and T is the gas temperature. γ_{sh} is the gas specific heat ratio and α_g is factor ($0 \leq \alpha_g \leq 1$), which characterizes the degree to which a gas molecule thermalizes with the sphere upon a single collision.

The actual value of ϵ_2 is uncertain for our micro-spheres. According to Ref. [63], $\epsilon_2 = 10^{-7}$ for bulk fused silica. We have observed trapped micro-spheres at high vacuum (10^{-6} Torr) with trap intensity $I_0 \sim 10^{10}$ W/m^2. As such, we can set an upper bound on $\epsilon_2 < 10^{-6}$. Solving equation 5.2 for T_{int} with these parameters gives a value of $T_{int} = 1042$ K, which is ~ 300 K below the continuous use temperature of fused silica. We expect $10^{-7} < \epsilon_2 < 10^{-6}$. In Collaboration with Dr. Pat Arnott's group at

UNR, we have also begun investigations of bead optical absorption coefficients using photoacoustic methods [64].

Figure 5.5 contains a plot of the theoretical internal temperature for a 3 μm sphere with $\epsilon_2 = 10^{-6}$. At high pressure ($>$ 10 Torr,) the micro-sphere is primarily cooled

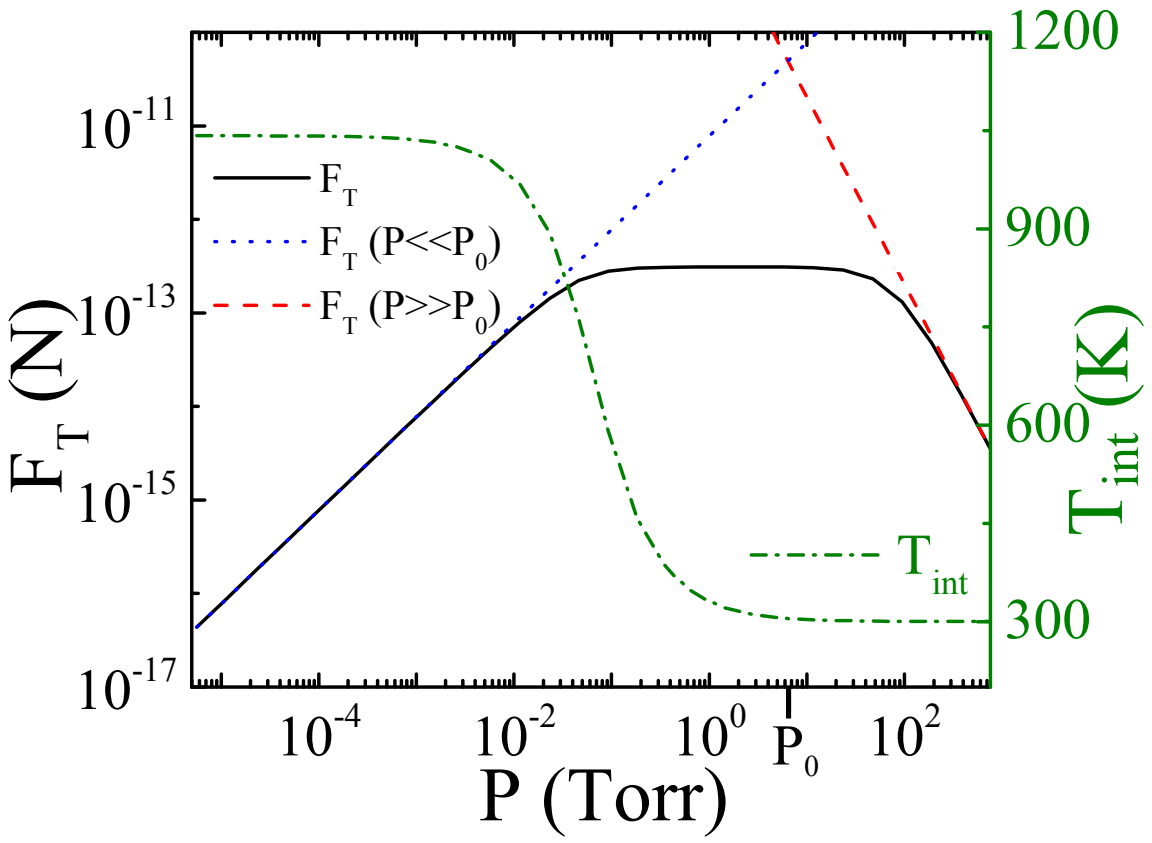

Figure 5.5: Radiometric force and internal temperature vs. vacuum chamber pressure. These calculations are for a 3 μm sphere with a laser intensity of 2 x 10^9 W/m^2. We assumed $\epsilon_2 = 10^{-6}$.

by collisions with the background gas. However, at high vacuum ($< 10^{-3}$) Torr, heat is primarily dissipated through blackbody radiation. The shape of the curve remains roughly the same for smaller ϵ_2, however the T_{int} values will be smaller.

Ref. [65] provides a model for radiometric forces on aerosols. The radiometric force is given by

$$F_T = -\frac{\pi r^2 \eta \sqrt{\frac{\alpha R_g}{MT}} \Gamma_i}{\frac{P}{P_0} + \frac{P_0}{P}}, \tag{5.7}$$

where η is the gas viscosity, M is the molar mass, R_g is the is the gas constant, Γ_i is the temperature gradient and P_0 is the MFP pressure. Plotted in figure 5.5 are F_T for the limits that $P \gg P_0$ (red dashed line) and $P \ll P_0$ (blue dotted line.) For $P \gg P_0$, F_T scales with $\frac{1}{P}$. In this region, thermalization is dominated by gas collisions and T_{int} is constant. However, for $P \ll P_0$, blackbody radiation is the dominant thermalization mechanism. In this region, F_T scales with P. In this model, F_T has a maximum value at P_0, which agrees with Ashkin's model in Ref. [38]. As mentioned previously, we have not observed dominant radiometric forces at P_0 experimentally.

Both of the radiometric force models presented so far (Ref. [38, 65]) assume that the temperature gradient of the micro-sphere Γ_i is pressure independent. The solid black curve in figure 5.5 is F_T from equation 5.7 with $\Gamma_i(P) \propto \frac{1}{P}$. This estimate assumes a 1% change in temperature across the surface of a 3 μm sphere due to the intensity gradient of the trap laser. We also assume the temperature gradient of the surface scales with the internal temperature if the micro-sphere. This results in a region where F_T is independent of P. In the regions far away from P_0, this model agrees with the models presented in Refs. [38, 65]. The shape of this curve is qualitatively similar for other temperature variations on the sphere's surface. At high pressure and high vacuum, F_T will still converge with the dotted and dashed curves. However, for other temperature variations, the flat region will change in magnitude. Since the value we used for ϵ_2 is an upper limit, we expect the magnitude of the force plotted to also be an upper limit. If the absorption were lower, the temperature gradient on the micro-sphere surface would decease resulting in a weaker radiometric force. In this flat region F_T is constant while gas damping decreases as pressure decreases, as seen in figure 4.18. Thus, when P is of order 1 Torr or less, radiometric forces continue to be significant as the pressure is lowered and can contribute to trap loss.

Figure 5.6 contains the COM temperature of the bead along the horizontal axis as a function of pressure for two beads. At sufficiently high pressures ($>$ 3-5 Torr), the temperature is largely independent of pressure. So, we assume that the bead

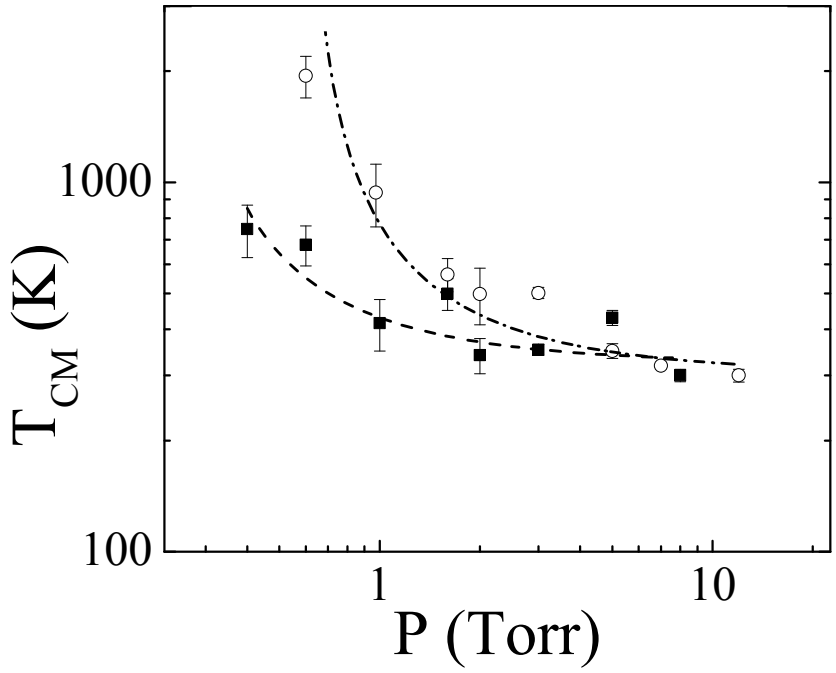

Figure 5.6: The measured center of mass temperature along the horizontal axis vs pressure. The trapping laser intensity is 2 x 10^9 W/m^2. At sufficiently high pressures, the temperature is largely independent of pressure. So, we assume that the bead is in thermal equilibrium with the gas above 5 Torr.

is in thermal equilibrium with the room temperature gas above 5 Torr. This is a reasonable assumption since the thermal conductivity of the gas is increasing with pressure until the transition out of the ballistic regime at ∼10-20 Torr. According the figure 4.18, Γ_{gas} begins to be non-linear with pressure above ∼10-20 Torr. Since the temperature equilibration has occurred around 5 Torr in the linear damping region, where the thermal conductivity of the gas is still increasing with pressure, we estimate that the equilibrium temperature is room temperature.

As another way to check the equilibrium temperature of the bead, we can study the temperature of the COM motion versus trap laser power at fixed pressure. Figure 5.7 contains position spectra for a 3 μm sphere trapped with a trap intensity of 2 x 10^9 W/m^2 and with the intensity reduced by a factor of 4 to 5 x 10^8 W/m^2 at 1.7 Torr. The lower intensity data is rescaled by the ratio of power (211/52) for better visualization of the trap frequency difference. The fitted temperature for the reduced intensity data is lower by a factor of .72. This data shows that the bead temperature

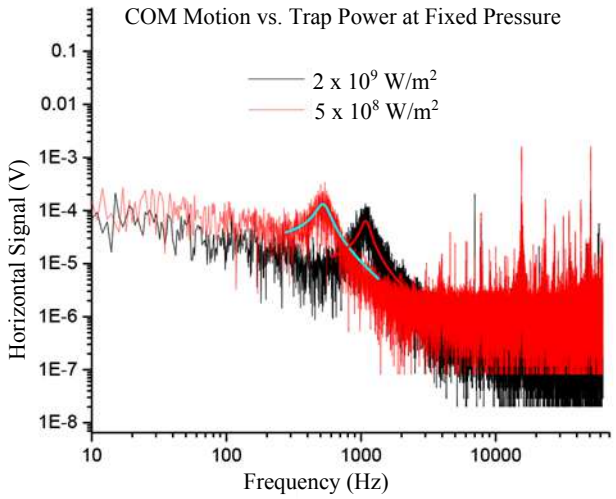

Figure 5.7: Position spectra for a 3 μm sphere trapped with a laser intensity of 2 x 10^9 W/m^2 and reduced intensity of 5 x 10^8 W/m^2 at 1.7 Torr. The lower intensity data was rescaled by the ratio of power (211/52) for better visualization of the trap frequency difference. Also shown are Lorentzian fits to the position spectra.

increases with trap intensity at 1.7 Torr and is not quite in thermal equilibrium with the surrounding gas. It is also below the 5 Torr cutoff, where we believe the bead is in thermal equilibrium with the surrounding gas. This is consistent with the behavior shown in figure 5.6. In the future, we plan to further validate our assumption by collecting further data involving varying the trap intensity at pressures above 3 Torr, where we do not expect to see a variance in bead COM temperature. Ref. [61] provides data for similarly sized beads and intensities. They do not see a change in COM temperature when varying the trap power at $\sim$ 3.75 Torr.

The average phonon $\langle n \rangle$ number in the trap can be written in 1-D as

$$\langle n \rangle (\Gamma_{gas} + \Gamma_{cool} - \alpha_{NC}) = \langle n_{th} \rangle \Gamma_{gas} + \Gamma_{sc}, \tag{5.8}$$

where α_{NC} corresponds to heating from the non-conservative scattering force and radiometric force. Γ_{sc} is due to laser noise and photon recoil. Γ_{gas} and Γ_{cool} are the gas and laser damping coefficients respectively. By turning off the feedback cooling we can get rid of Γ_{cool} from equation 5.8. The right hand side of equation 5.8 vanishes at the pressure where the micro-sphere is lost. Under these circumstances, the $\Gamma_{gas} \approx \alpha_{NC}$. By experimentally measuring Γ_{gas}, we can estimate α_{NC}. For trap intensities under

4 x 10^9 W/m^2, the loss pressure is $\sim$ 250 mTorr (figure 5.1). This corresponds to a range of 20 - 50 Hz for the non-conservative heating rate α_{NC}. Variations in this value may be due to differences in the absorption coefficient of a particular bead or variations in the trap alignment.

5.3 Feedback Cooling at High Vacuum

In an effort to minimize the effect of radiometric forces while pumping down from $\sim$2 Torr, we reduce the trap intensity to 2 x 10^9 W/m^2. This lowers the loss pressure, as plotted in figure 5.1, and the temperature gradient across the sphere's surface. The lower intensity still provides a sufficient trap depth ($\sim$3 x 10^6 K along the vertical axis) while the feedback cooling system provides adequate damping and stabilization. The feedback intensity typically ranges from $\sim 10^7$ W/m^2 to $\sim 10^8$ W/m^2 in the radial directions. The gain of the feedback signal is adjusted so that the linewidth of the mechanical resonace is $\sim$ 400 - 500 Hz in the radial directions and $\sim$300 Hz along the axial axis. Once the trap intensity has been decreased and the feedback is optimized, we slowly open the valve between the turbo pump and vacuum chamber. The purpose of slowly opening the valve is to not create air currents that cause bead loss. Once the trapped bead is at high vacuum, we can increase the laser power to provide a deeper trap depth.

Figure 5.8 contains the DFT power spectrum along the horizontal axis for a 3 μm sphere cooled with various feedback laser powers at 5 x 10^{-6} Torr. As the laser power increases so does Γ_{cool}, the feedback damping coefficient. As such, the resonant peaks decrease in amplitude and broaden with increasing power. The fact that we can reduce the feedback power at high vacuum without bead loss suggests that radiometric forces are a mechanism for trap loss at inetermediate pressure. This is also consistent with the theoretical model for the radiometric force presented in figure 5.5.

Figure 5.9 contains horizontal position spectra for various trap powers at 5 x

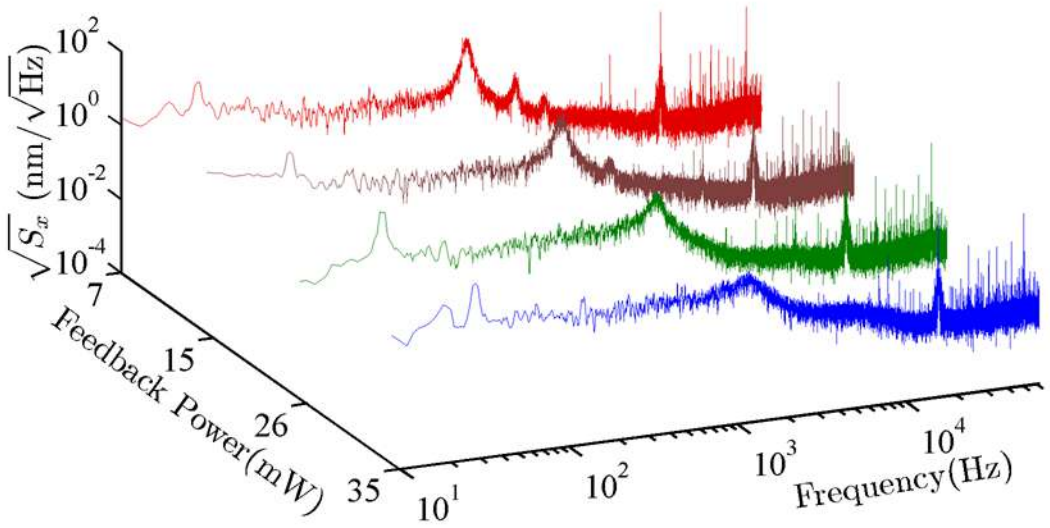

Figure 5.8: DFT power spectrum for a 3 μm sphere with active feedback cooling at 5 x 10^{-6} Torr. As the feedback laser power increases the peaks decrease in amplitude and broaden.

10^{-6} Torr. By changing the intensity of the trap, we are able to tune the frequency

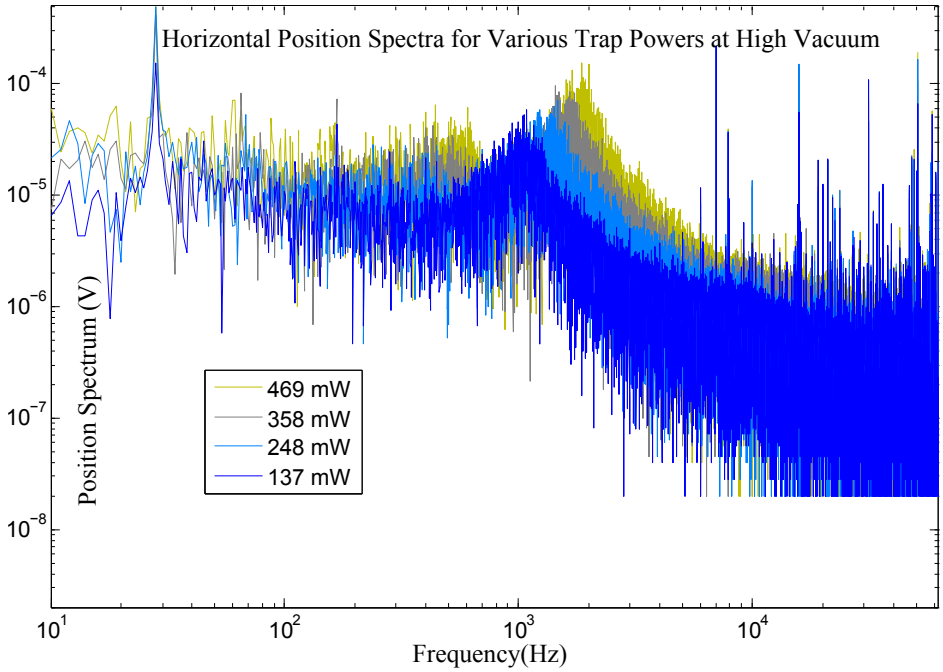

Figure 5.9: Horizontal Position Spectra for Various Trap Powers at High Vacuum.

of the oscillator. In this example, we were able to vary the trap frequency by roughly

a factor of 2.

From our analysis of dual-beam dipole trap instabilities while pumping down, we have come to two conclusions. First, the alignment of the counter propagating trap beams is critical. We have dealt with this issue by steering the non-imaging trap beam with a mirror mounted on piezoelectric transducers. Ref. [40] address the issue of fine alignment by steering trap beams with acoustic optical modulators. Second, our theoretical analysis of radiometric forces suggests that the pressure range over which radiometric forces are at a maximum is larger than previously thought. By lowering the trap intensity sufficiently, we succeeded in reducing the radiometric forces enough to allow us to pump down to high vacuum rapidly. At high vacuum, we increase the trap intensity and maintain trap lifetimes of days. The previous record for dual-beam trap lifetime at high vacuum is 88 minutes [40].

Plotted in figure 5.10 are characteristic 3-D position spectra of a bead held at 1.7 Torr with no feedback cooling (red,) and at 5 x 10^{-6} Torr with feedback damping. The transverse frequencies are 1073 Hz and 1081 Hz for the horizontal and vertical

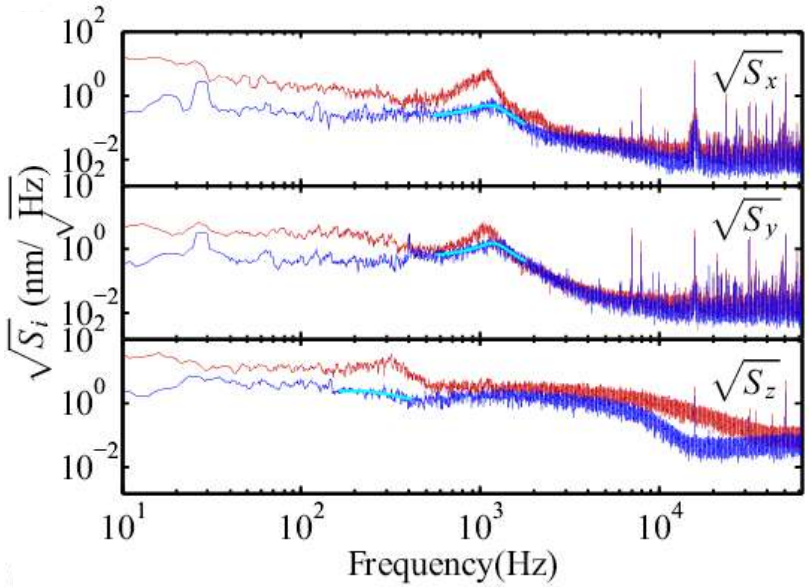

Figure 5.10: Typical position spectrum of a bead held at low vacuum of 1.7 Torr with no feedback cooling applied (red), and at high vacuum of 5×10^{-6} Torr with feedback cooling applied (blue). Also shown (light blue) is a Lorentzian fit to the peaks in the high vacuum data, with fit parameters as discussed in the text.

modes respectively. The axial mode frequency is 312 Hz. By performing a Lorentzian fit to the peaks, we can determine the effective COM temperatures for each mode. For the high vacuum spectra, we get 10 ± 3 K, 55 ± 9 K, and 12 ± 2 K for the horizontal, vertical and axial modes respectively. These temperatures equate to the following effective damping rates: 454 ± 29 Hz, 448 ± 16 Hz, and 340 ± 120 Hz. The amplitude of the cooled peak along the horizontal axis corresponds to a force sensitivity of $S^{1/2}_{F,x_{horizontal}} = 217 \pm 48$ aN$/\sqrt{\text{Hz}}$. The error is dominated by the uncertainty in the micro-sphere size and the distance to voltage calibration.

Theoretically, the predicted sensitivity at 5 x 10^{-6} Torr should be 100 times better. Cross talk between the feedback lasers prevents us from reaching the lowest attainable temperatures. Plotted in figures 5.11 and 5.12 is the laser noise (green) and electrical noise (light blue) on the same axes as the position spectrum for a bead at low vacuum (red) and high vacuum (dark blue.) This data was collected by first recording the low vacuum spectrum. Next, the the chamber was pumped down to high vacuum with the same bead used for the low vacuum data. Data was then recorded at high vacuum. Next, the bead was intentionally lost from the trap and the laser noise was recorded. Lastly, the laser was turned off and the electric noise in the QPDs was recorded. Within the frequency range of the horizontal and vertical modes there is a significant amount of laser noise. Note that the laser noise dominates over the electronics noise. Figure 5.13 contains the laser and electronics noise from the axial channel. In this figure, the laser noise is significantly less than in figure 5.11. This is because the axial channel uses the scattered light from the bead to image its motion while the horizontal channel uses the shadow of the bead in the laser. In this situation there is no laser light being measured, so the laser noise spectrum is similar to the electronic noise spectrum. The steep roll off around 5000 Hz results from detector bandwidth. A peak from DAQ digitization noise is also visible in the spectrum at $\sim$10.7 kHz. In the near future, we have plans to stabilize the dipole trap laser with a proportional-integral-derivative controller.

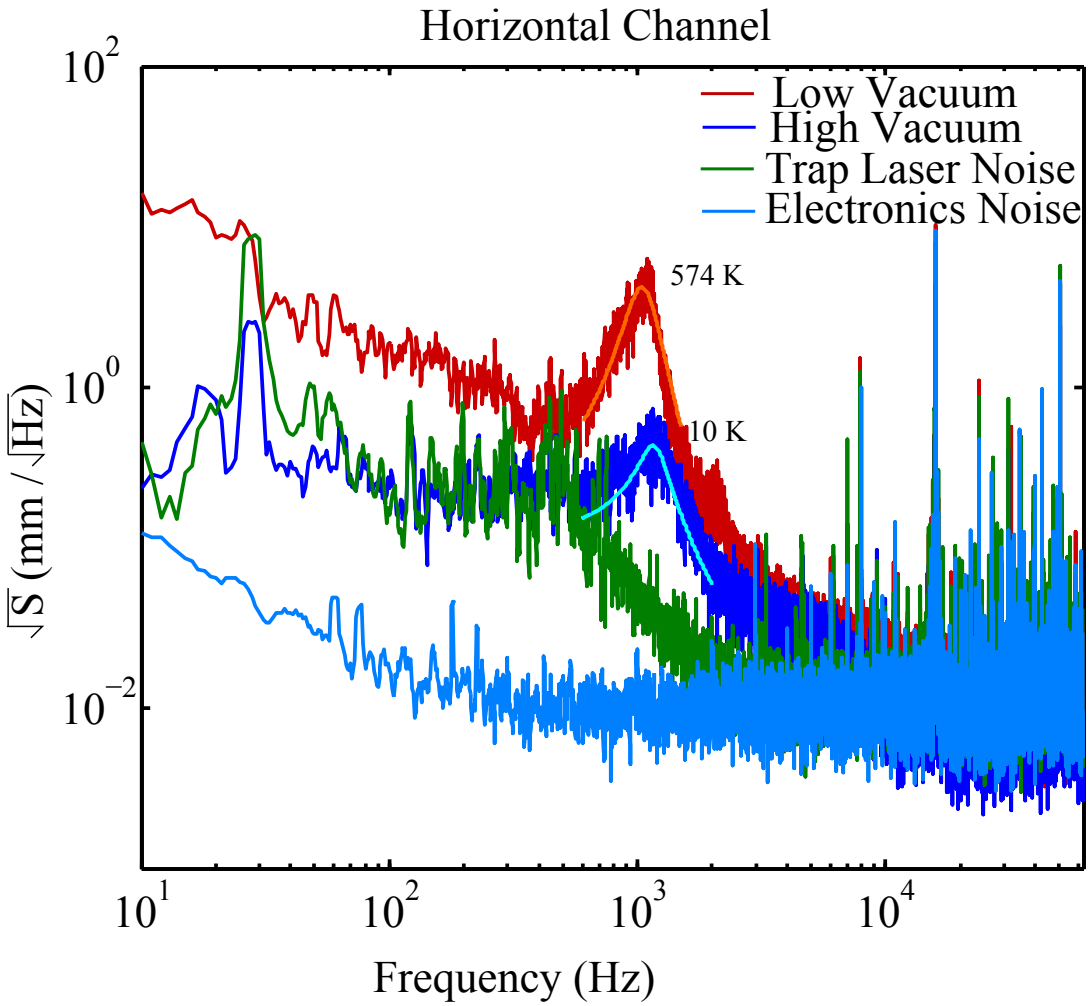

Figure 5.11: The power spectrum of the laser and electronics noise from our system. Also plotted is the position spectrum for a bead trapped at ∼1 Torr and ∼5 x 10^{-6} Torr. Laser noise limits the ability to cool the micro-sphere.

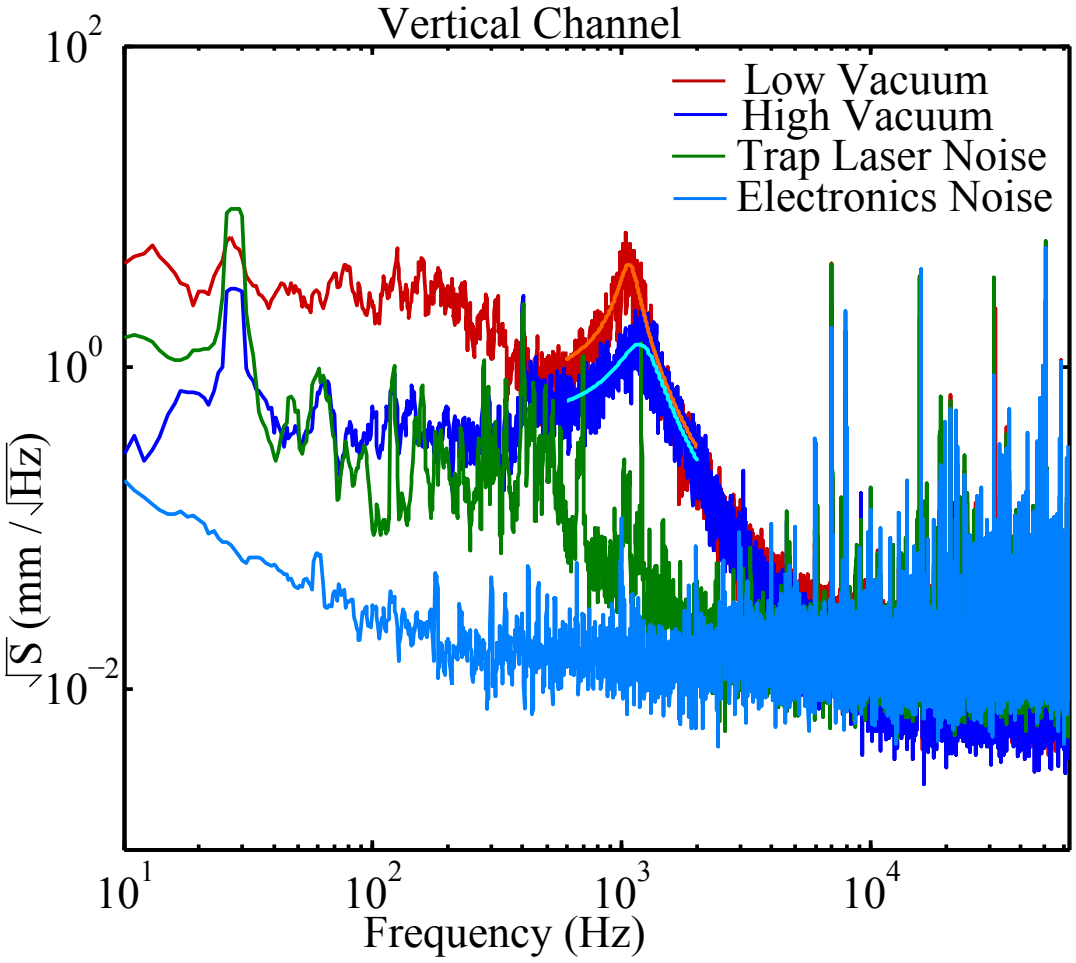

Figure 5.12: The power spectrum of the laser and electronics noise from our system. Also plotted is the position spectrum for a bead trapped at ∼1 Torr and ∼5 x 10^{-6} Torr. Laser noise limits the ability to cool the micro-sphere.

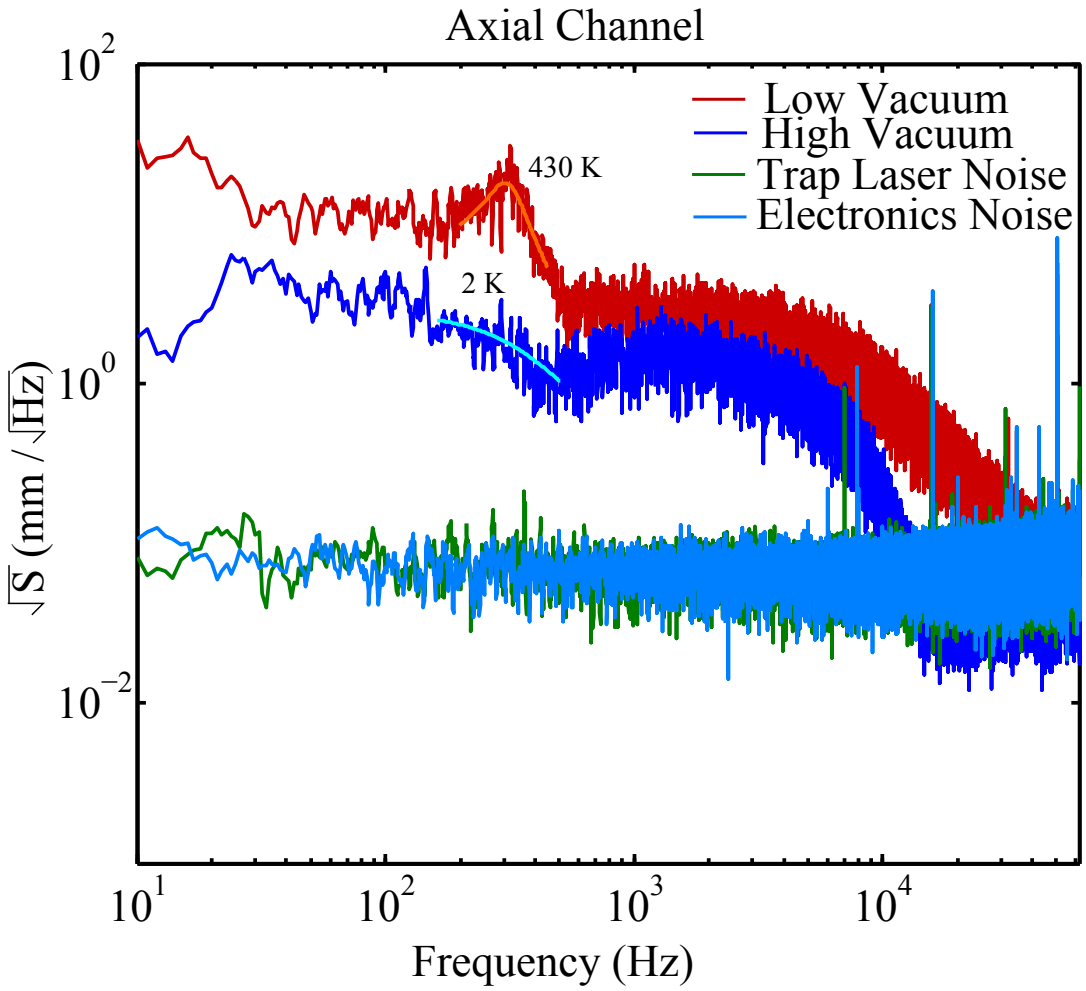

Figure 5.13: The power spectrum of the laser and electronics noise from our system. Also plotted is the position spectrum for a bead trapped at ∼1 Torr and ∼5 x 10^{-6} Torr.

Chapter 6

Force Measurements

The eventual goal of the work presented in this dissertation is to measure corrections to Newtonian gravity at the micro-meter length scale with a 300 nm diameter fused silica sphere near a test mass. The theoretical best force sensitivity for this configuration is $\sim$ 1zN/$\sqrt{Hz}$ [1]. In this chapter, we describe a force calibration method and provide results showing the current state of the system with a force sensitivity of $\sim$200 aN/$\sqrt{Hz}$. We estimate improved sensitivity is possible with reduced laser noise. Our results have also been posted to the arxiv [66].

6.1 Force Sensing

Harmonic oscillators are suitable force measuring devices since the measured amplitude is proportional to an applied driving force. In the case of this experiment, we apply a sinusoidal electric force to a micro-sphere trapped in a dual-beam optical trap.

Thermal fluctuations ultimately limit the force sensitivity of a levitated micro-sphere. The minimum force detectable can be calculated from the Equipartition Theorem from Statistical Mechanics by treating the micro-sphere as a harmonic oscillator in thermal equilibrium with a bath at temperature T [67],

$$F_{min} = \sqrt{\frac{4k_bTbk}{\omega_0 Q}}, \tag{6.1}$$

where b is the measurement bandwidth, k is the spring constant of the oscillator, k_b

is Boltzmann's constant, w_0 is the resonance frequency, and Q is the quality factor (Q-factor). Equation 6.1 be written as

$$F_{min} = \sqrt{4k_b T m \gamma b}, \tag{6.2}$$

where $\gamma = 16P/(\pi\rho v r)$ is the damping coefficient of the surrounding gas, v is the average thermal velocity of the gas, m is the mass of the sphere, r is the radius, m_{gas} is the mass of the gas, P is the pressure, and ρ is the density of the object. Looking at equations 6.1 and 6.2, we see that there are a few experimentally modifiable parameters that can improve force sensitivity.

1. Increase the measurement integration time (decease b.)
2. Decrease the temperature T.
3. Increase the oscillator quality factor Q by decreasing vacuum chamber pressure P

It is believed that optically trapped micro-sphere oscillators can attain $Q \sim 10^{12}$ in ultra high vacuum. With such a high Q and our typical radial trap frequency of 3500 Hz, the ring down time would be $\tau = \frac{2Q}{\omega_0} \sim 6 \cdot 10^8$ seconds. Since such a high Q is unacceptable experimentally, we use a feedback cooling method to optically damp (decrease Q) and cool the center of mass temperature of the of the micro-sphere simultaneously. Fortunately, the feedback damping system reduces Q and T by a similar amount, except for small effects due to photon recoil [68].

The two main parameters we can tweak to improve force sensitivity are integration time and vacuum pressure. Reducing the chamber pressure turned out to be a non-trivial engineering feat because of turbulence while pumping and radiometric forces.

6.2 Experimental Setup

The experimental setup is illustrated in figure 6.1. This system is similar to that presented in chapter 4. Two copper wires and a grounded metallic plane are placed

near the trapped micro-sphere and are used to apply a time varying electric force to the micro-sphere. By applying a known electric force on the micro-sphere, we can determine the conversion factor for converting the QPD voltage to a force.

Figure 6.2 contains an illustration of the force calibration wires and grounded plane. An AC voltage was applied to the two wires. The sum of the electric fields from the the wires is directed along the horizontal axis at the micro-sphere's location. A sphere with polarizability α and charge q experience the following force F when interacting with an electric field E,

$$\mathbf{F} = \frac{1}{2}\alpha \bigtriangledown E^2 + q\mathbf{E}. \tag{6.3}$$

The charge q is the result of excess electrons on the micro-sphere. The second term in equation 6.3 dominates when electrons are present.

6.3 Force Calibration Procedure

Once a micro-sphere is trapped we measure its position spectrum at a pressure above 5 Torr. As discussed in chapter 5, we believe the micro-sphere is in thermal equilibrium with the surrounding gas at this pressure. Figure 6.3 contains the position power spectrum along the horizontal axis for a 3 μm sphere trapped above 5 Torr. A Lorentzian fit was performed on the peak to determine the amplitude V_{peak}, frequency ω_0 and Q of the oscillator. The force-to-voltage conversion factor is then given by dividing equation 6.1) with V_{peak}:

$$\text{force-to-voltage} = \frac{F_{min}}{V_{peak}}. \tag{6.4}$$

Once the force-to-voltage conversion factor is known, we can test our systems force sensitivity by applying a known electric force on the micro-sphere with the wire and grounded plane system at frequency ω. When the bead is driven at the trap frequency ($\omega = \omega_0$,) the amplitude of the mechanical motion increases with Q. However, when we drive the motion of the bead at an off resonance frequency ($\omega \gg \omega_0$,) the mechanical amplitude of the mechanical motion scales as $\frac{1}{\omega^2}$. By taking

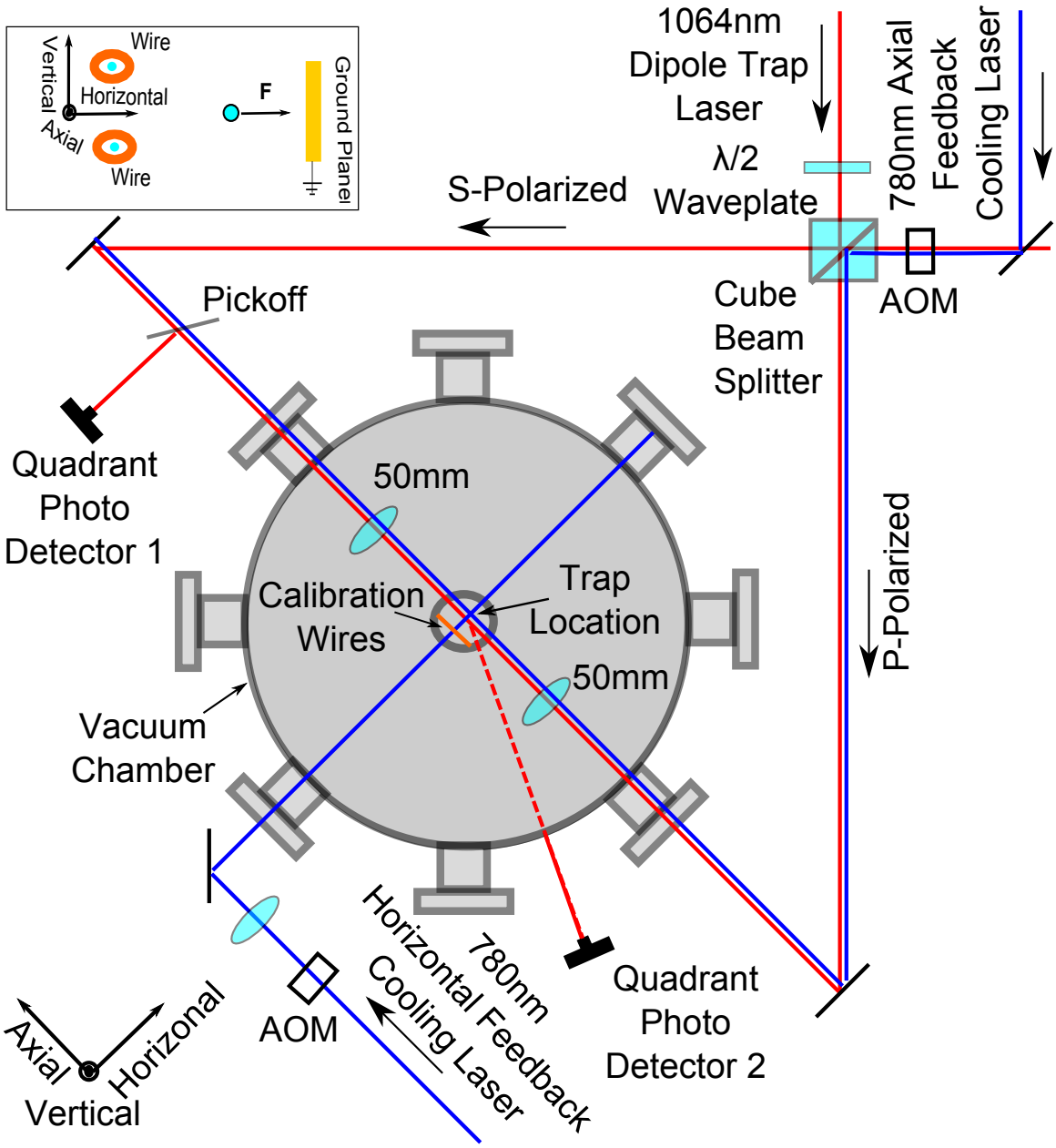

Figure 6.1: The optical dipole trap is created by focusing two orthogonality polarized laser beams at the same point in space. This is achieved by splitting a 2.2 W 1064 nm laser beam into two orthogonality polarized beams with a $\frac{\lambda}{2}$ waveplate and a polarizing cube beam splitter. The two beams carry roughly half the total laser power and are focused to the same spatial location with 50 mm lenses. Three 780 nm active feedback lasers stabilize trapped beads in vacuum and provide optical damping.

the difference between the amplitude of the on and off resonance driven peaks, we determine how much of the on resonance driving signal is electronics noise and how

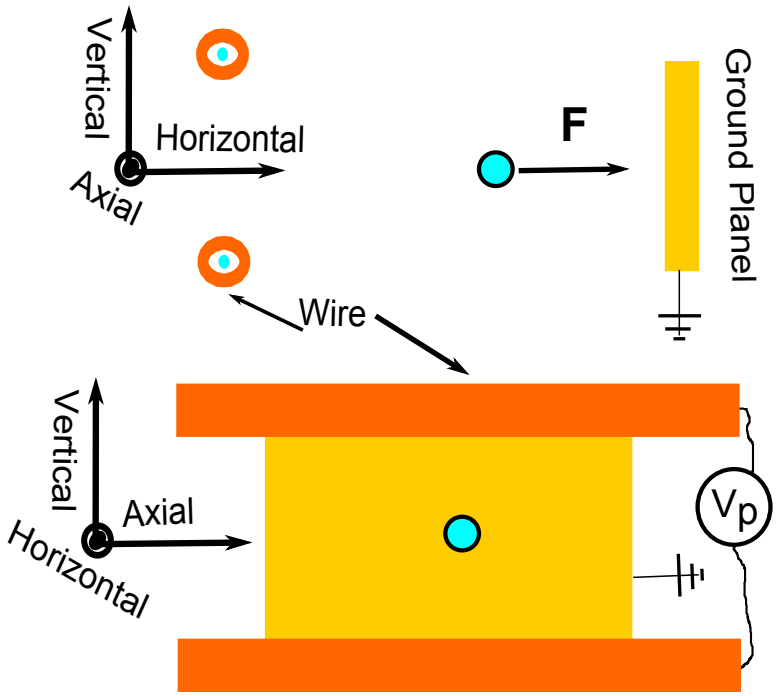

Figure 6.2: Force calibration wire and grounded plane drawing. A time varying voltage is applied to the wires which produces a time vary electric field along the horizontal axis at the micro-sphere's position.

much of the signal is mechanical motion. Figure 6.4 contains DFTs with on and off resonance driving. This calibration method and the data presented is provided by Ref. [69] and taken at ∼1 Torr. The force measurements results presented later in this chapter were performed for trap resonances near 1.1 kHz and not ∼3815 kHz as plotted in figure 6.4. The off resonance driving was taken at 7 kHz.

6.4 Results

Plotted in figure 6.5 is the calculated minimum force from equation 6.1 (red) and the measured thermal force (black) along the horizontal axis as a function of averaging time. Without an applied force, we expect from equation 6.1, the thermal noise to average down as the square root of the measurement bandwidth. After averaging for 10 hours, we have shown sensitivity of ∼2 aN. Theoretically, the predicted sensitivity

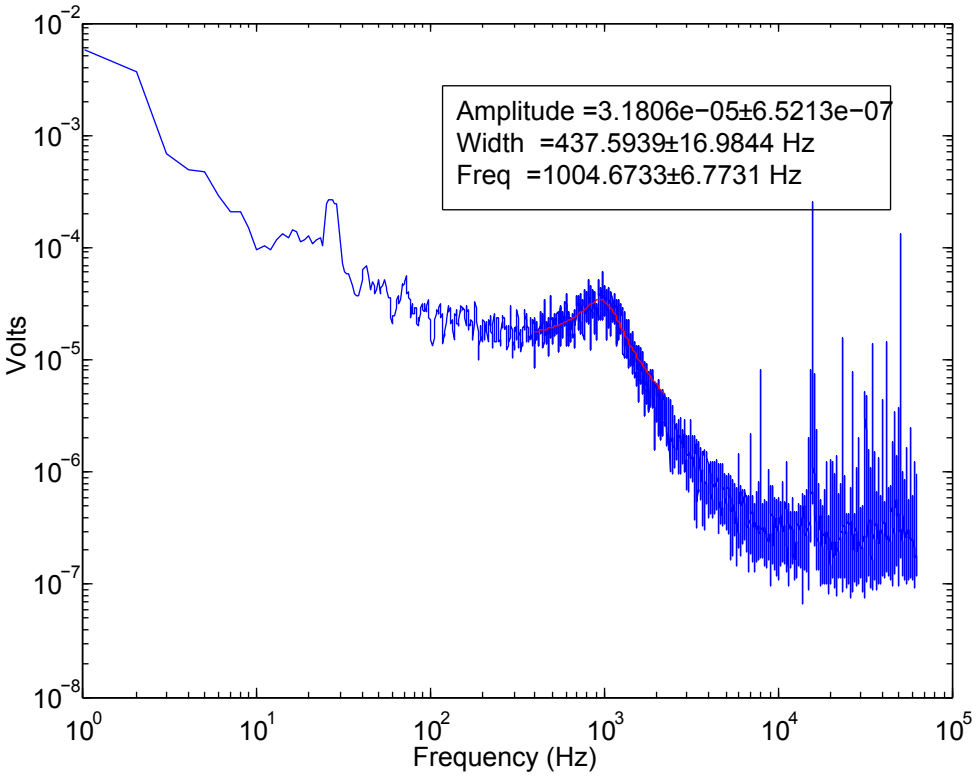

Figure 6.3: Lorentzian fit of the horizontal peak for a 3 μm sphere trapped above 5 Torr. The amplitude of the peak is used to convert the QPD signal in Volts to Newtons.

at 5 x 10^{-6} Torr should be 100 times better. Cross talk between the feedback lasers and trap laser noise prevent us from reaching the lowest attainable temperatures as discussed in section 5.3.

We found that ∼80% of trapped beads have excess electric charge due to extra electrons. Typical charge ranged from 0 to 40 e^-. By applying UV light we were able to remove some of the excess charge, but not all [69]. With a more energetic UV source we hope to remove all excess charge. The charge on the bead can be determined by knowing the electric field and measuring the bead displacement.

Plotted in figure 6.6 are the measured electric forces on beads with no charge or $2e^-$ charge as a function of averaging time for various applied electric fields. The driving signal frequency is on resonance with the trap frequency for these measurements. When the applied field is turned off, the thermal noise averages down as expected.

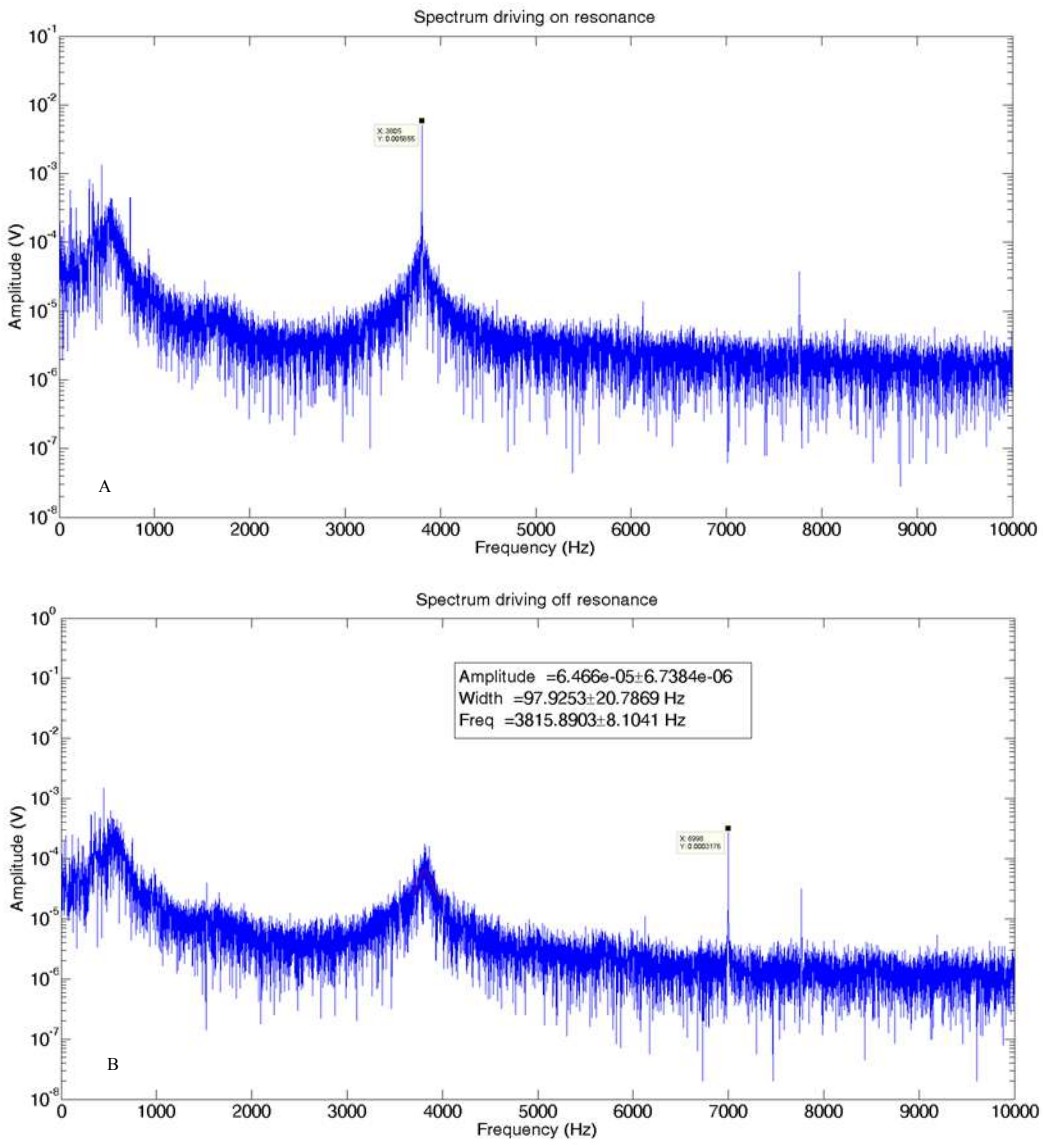

Figure 6.4: [DFT of on and off resonance driving with the force calibration wires. A) The horizontal position spectrum while driving on resonance frequency with the calibration wires. B) The horizontal position spectrum while driving off resonance frequency with the calibration wires. This data was taken at ∼1 Torr and not at high vacuum.

When no charge is on the bead, only the gradient term in equation 6.3 remains. The sensitivity of the gradient force is currently within the noise of our system. When a non-zero charge is on the micro-sphere, the second term in equation 6.3 dominates. In this case, the applied force is much greater than the thermal force. For driving

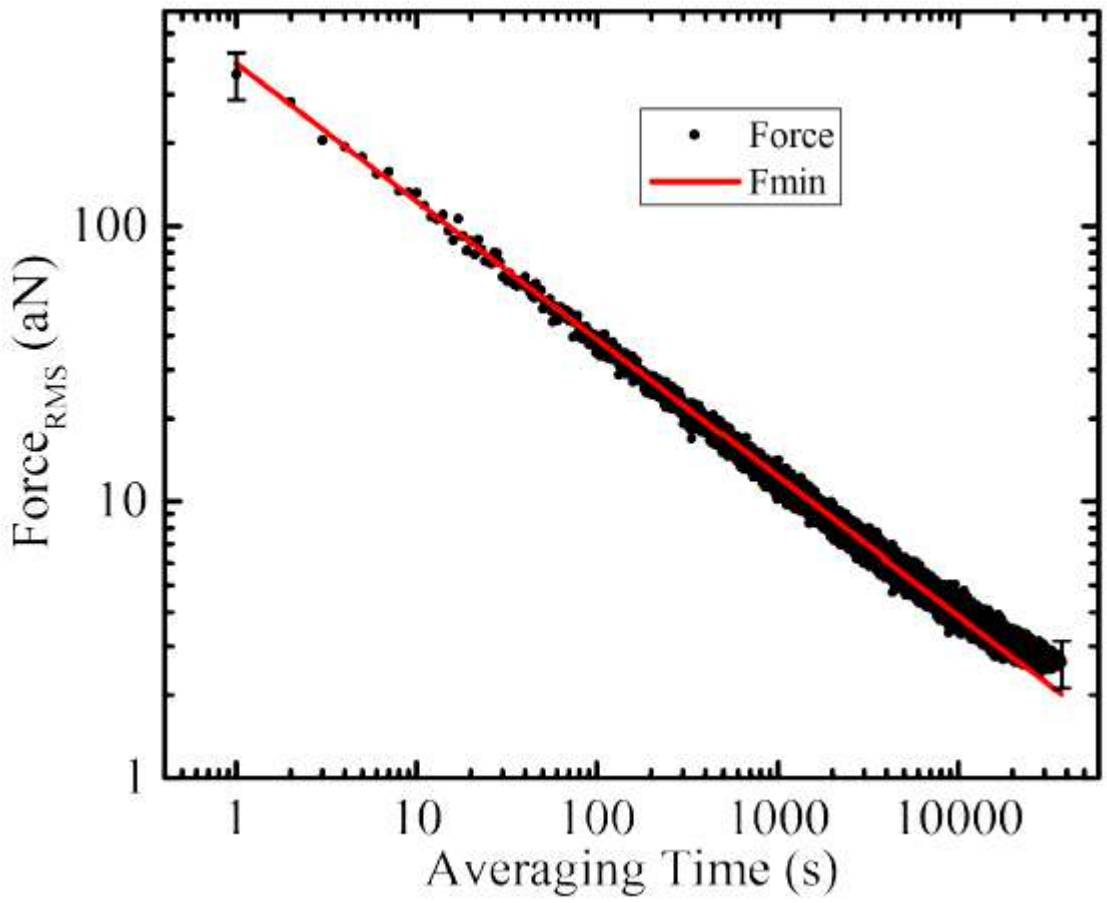

Figure 6.5: The measured thermal force on a 3 μm sphere along the horizontal axis without driving versus averaging time.

voltages up to 8 V, we found that the electronic noise is insignificant after averaging for 100 s.

The driving force uncertainty was determined by propagating the uncertainty in the bead radius (5%,) and Lorentzian fit (1σ confidence interval.) Both uncertainties translate into uncertainty in the distance to voltage conversion factor K_{dv}, the oscillator spring constant $k = m\omega_0^2$ and Q. The error in K_{dv} is given by

$$\Delta K_{dv} = K_{dv}\sqrt{\left(\frac{\Delta x_{th}}{x_{th}}\right)^2 + \left(\frac{\Delta V_{th}}{V_{th}}\right)^2}, \tag{6.5}$$

where V_{th} is the amplitude of the fitted position spectrum voltage and x_{th} is the theoretical RMS amplitude of the beads COM motion. The uncertainty in x_{th} is from

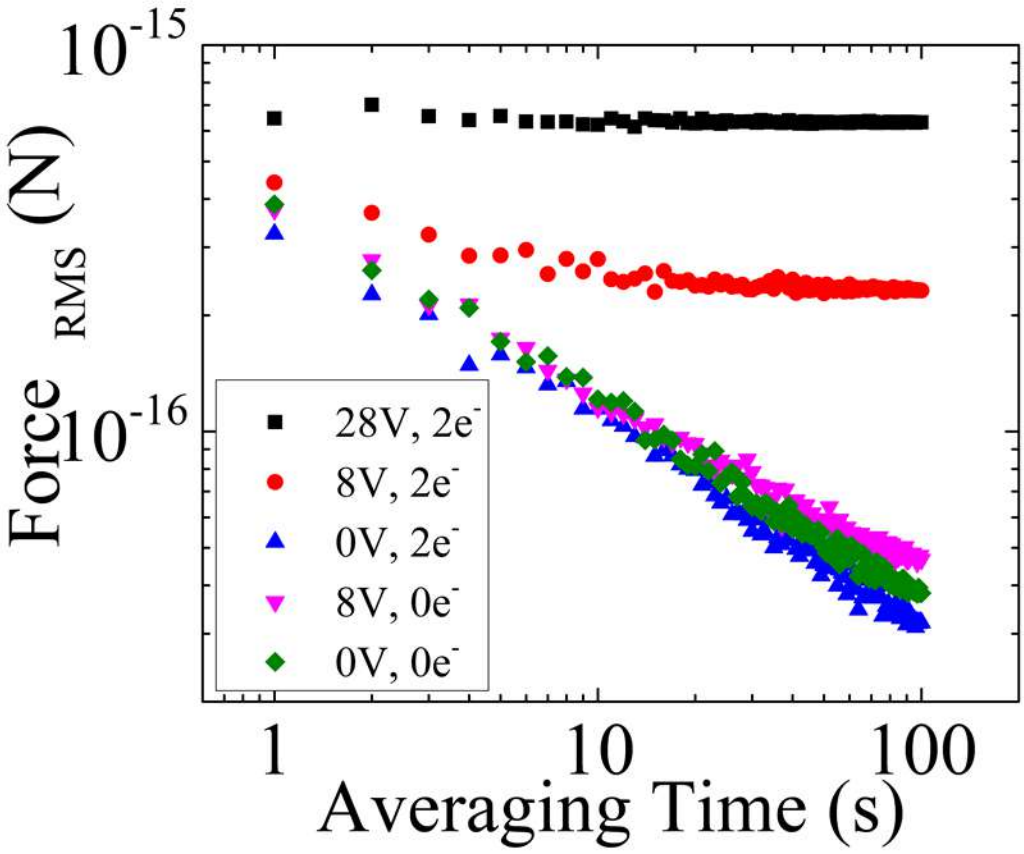

Figure 6.6: The force on a neutral bead ($0e^-$) and a charged bead ($2e^-$) versus avreraging time with various driving driving voltages.

the uncertainty in the size of the bead. The is also uncertainty in k is given by

$$\Delta k = k\sqrt{\left(\frac{\Delta m}{m}\right)^2 + \left(\frac{2\Delta\omega_0}{\omega_0}\right)^2}. \tag{6.6}$$

The error in the driving force is then given by

$$\Delta F_{driven} = F_{driven}\sqrt{\left(\frac{\Delta k}{k}\right)^2 + \left(\frac{\Delta K_{dv}}{K_{dv}}\right)^2 + \left(\frac{\Delta Q}{Q}\right)^2}. \tag{6.7}$$

Since the driving field E is known, the charge on the bead q is given by the second term in equation 6.3. The measured value for the charged bead in figure 6.6 was 1.83 $\pm$ .21. So, we assigned it a value of $2e$.

Plotted in figure 6.7 are the forces on beads with various charge as a function of applied electric field. The uncertainty in charge increases with number of elec-

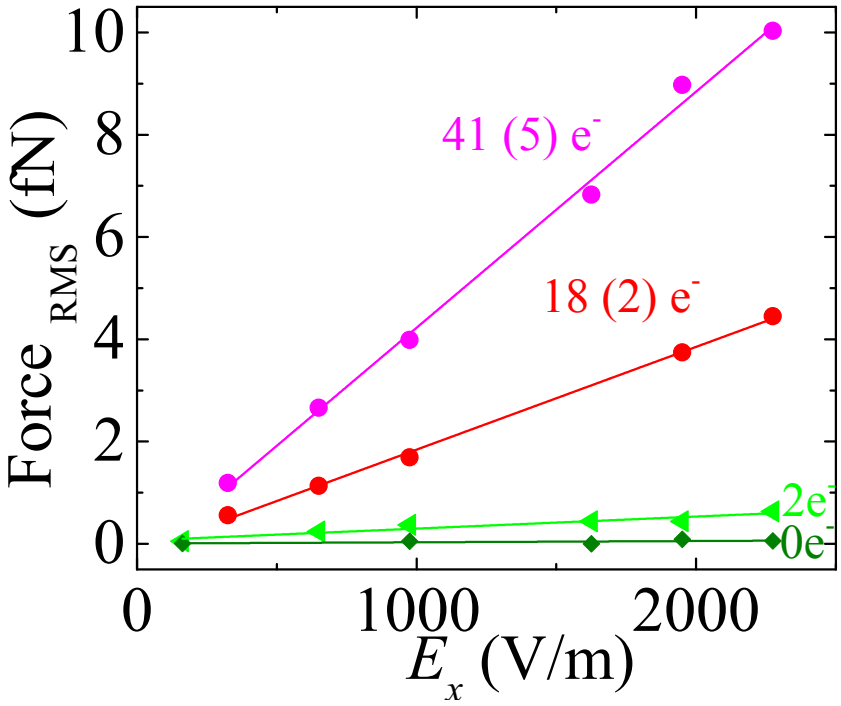

Figure 6.7: The force on beads of varying charge vs. the applied driving voltage and corresponding electric field.

trons, because the applied force scales with charge. A Monte-Carlo simulation was performed to determine the error in the charge number. In the Monte-Carlo, each point in figure 6.7 is varied according to the experimental uncertainty and the overall uncertainty of the slope is determined. The resulting error in number of electrons appears in parenthesis.

Chapter 7

Future Outlook

7.1 Current Technical Challenges

7.1.1 Dipole Trap Power Stabilization

As discussed in section 5.3, noise in the dipole trap laser limits our ability to cool the COM of trapped micro-spheres. The trap laser model is the Ventus HP 1064 3 W Laser manufactured by Laser Quantum. Before purchasing the laser, we had the foresight to purchase one with constant power control. Unfortunately, the manufacturer sent us a laser without this functionality, even though the terms of purchase included it. Fortunately, the laser controller has the option to control the power with a 0 - 5 V pin on a D-sub connector. In the very near future we will attempt to address this issue by feedback stabilizing the laser with a PID controller.

7.1.2 Imaging 300 nm Micro-Spheres

Ideally, we would like to use the same QPD imaging system for 300 nm micro-spheres. Since the smaller spheres scatter significantly less light and produce a smaller shadow in the trap beam, we need to make modifications to the system.

We have already seen a small signal along the axial channel with the scattering QPD. As such, we are hopeful that the only modification needed to the scattering detector is to change the gain of the transimpedance amplifiers in the QPD circuit, depicted in 4.15. We may also need to modify the imaging optics to produce a larger image on the QPD.

With the current shadow QPD system, we have not seen a signal from 300 nm micro-spheres. Most likely, we will need to modify the imaging optics to provide a larger shadow on the QPD. Another option would be to use two scattering detectors for 3-D imaging.

In an ideal world, we would prefer to have one imaging system for a wide range of micro-sphere sizes. Although all future experiments will predominantly use the smaller 300 nm spheres, it is convenient to have the ability trap and image 3 μm spheres for alignment purposes.

7.1.3 Launching Small Spheres

In section 4.3.1, we discussed the difficulty of launching micro-spheres under 1 μm in diameter with the diving board method. We have successfully launched and trapped 300 nm micro-spheres with our current diving board system, but there are two major issues that need to be addressed. First, we only catch a few 300 nm per day; whereas we can catch 3 μm within minutes. Second, we regularly break piezos, microscope slides and the piezo driver because of the high voltages required to launch 300 nm spheres.

The nebulizer method is successful at depositing micro-spheres in the optical trap. However, it has two major drawbacks. First, the chamber pressure needs to be close to atmospheric pressure. Otherwise, the pressure gradient between the nebulizer and vacuum chamber is too great. The pressure gradient accelerates the micro-spheres to velocities well above the trap capture velocity. Once a 300 nm bead is trapped, it takes many hours to pump down to a few mbar. The second drawback of the nebulizer method is that some of the micro-sphere solution enters the chamber, which is not convenient for pumping down to high or ultra-high vacuum.

Ref. [70] has developed a clever technique for depositing nm scale diamonds into a dipole trap. They deposit the nano-diamonds onto a single atom layer of graphene and burn a hole through the graphene with a laser. We have already purchased graphene and hope to try this technique out for ourselves.

7.2 Optical Cavity Trapping and Cooling

A primary goal for our research group is to optically trap and cool micro-spheres in an optical cavity. Illustrated in figure 7.1 is the cavity we are currently working with. Two lasers are injected into the cavity. A 1596 nm laser traps the micro-sphere

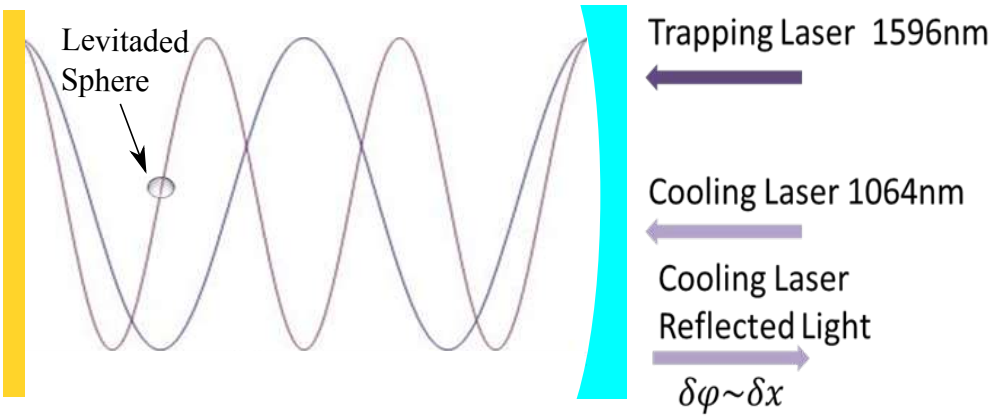

Figure 7.1: Illustration of the experiment optical cavity. The input mirror is a curved glass mirror and the output mirror is a flat gold mirror. Two lasers are injected into the cavity and on resonance with it. A 1596 nm laser traps a micro-sphere and a 1064 nm laser cools the COM motion along the cavity axis.

at the first anti-node from a flat gold mirror. The second laser, 1064 nm, cools the micro-sphere's center of mass (COM) motion along the cavity axis. The lasers were chosen because the ratio of their wavelengths is 2/3. With this ratio, the intensity gradient of the cooling laser is at a maximum which is convenient for measuring the micro-sphere's displacement. The challenge we faced was locking two lasers to a cavity and maintaining a 2/3 ratio of their wavelengths. The solution we came up with was to first frequency stabilize both lasers to a reference cavity with very little thermal expansion. Second, we locked the experiment cavity to the trapping laser. With this configuration, the two lasers should maintain the 2/3 wavelength ratio.

7.2.1 Reference Cavity

The reference cavity is composed of a two curved mirrors and a glass spacer between the mirrors. Both of the mirrors and the spacer are made from ultra low expansion

(ULE) glass and optically fused together. The cavity is roughly 1 cm long which corresponds to a FSR of 15 Ghz. Figure 7.2 contains a photograph of the reference cavity mounted in a 3 way conflat T, which acts as a vacuum chamber. The cavity is

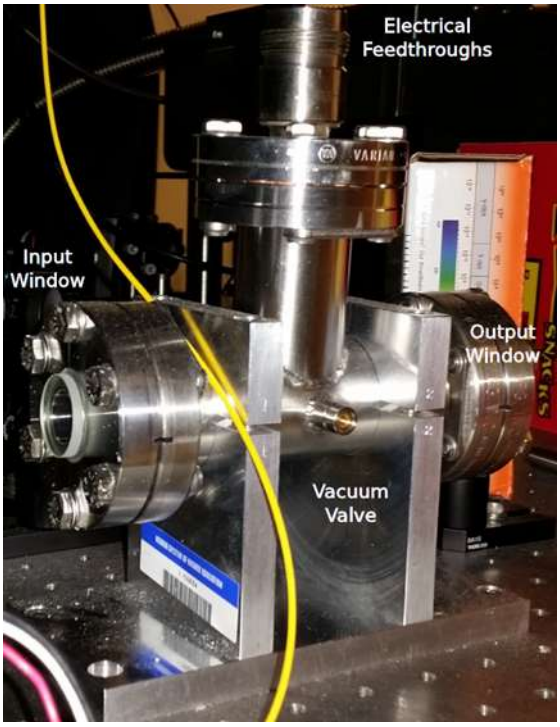

Figure 7.2: The reference cavity mounted in its low vacuum chamber.

mounted on a conflate with a 1 inch window for the laser input. On the opposit end of the T is a 2.5 inch window for monitoring the cavity transmittion with either a CCD camera or wavelength meter. A conflat with electrical feedthroughs is mounted on the top of the T and provides electrical connections for temperature control.

7.2.2 Experiment Cavity

Our experiment cavity, pictured in figure 7.3, has a length of roughly 5 cm, which corresponds to a FSR of 3 GHz. The input mirror has a radius of curvature of 5 cm and the output mirror is a flat gold coated mirror. The input side of the input mirror has AR coatings for 1064 nm, 1596 nm and 780 nm. The reflective curved side has reflective coatings for 1064 nm and 1596 nm. The spacer is machined from two blocks of aluminum. However, this is a temporary proof of concept cavity. The

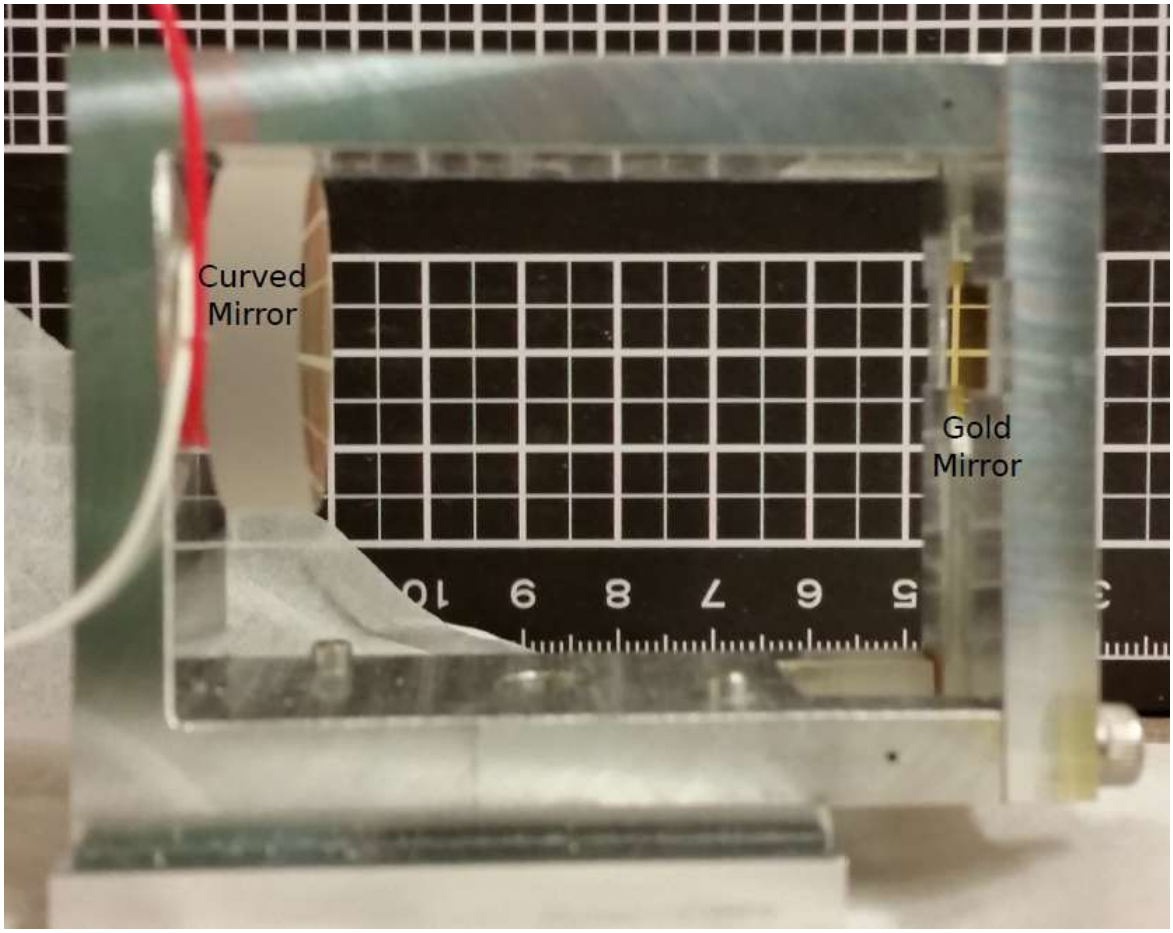

Figure 7.3: The experiment optical cavity.

actual experiment cavity spacer will be machined from a single block of Invar, which has very low thermal expansion. Figure 7.4 is a photograph of the experiment within the vacuum chamber.

7.3 Prospects for the Future of the Field

In this section we discuss some of the future experiments planned in the field of levitated micro-spheres. Although it is not an exhaustive list (we have certainly left out a lot of amazing experiments) we hope to share with the reader our excitement of the future of the field.

Cooling macroscopic systems, like a micro-sphere, to the quantum ground state is a hot topic today. Many groups have efforts in this area [40, 41, 71, 72]. Our

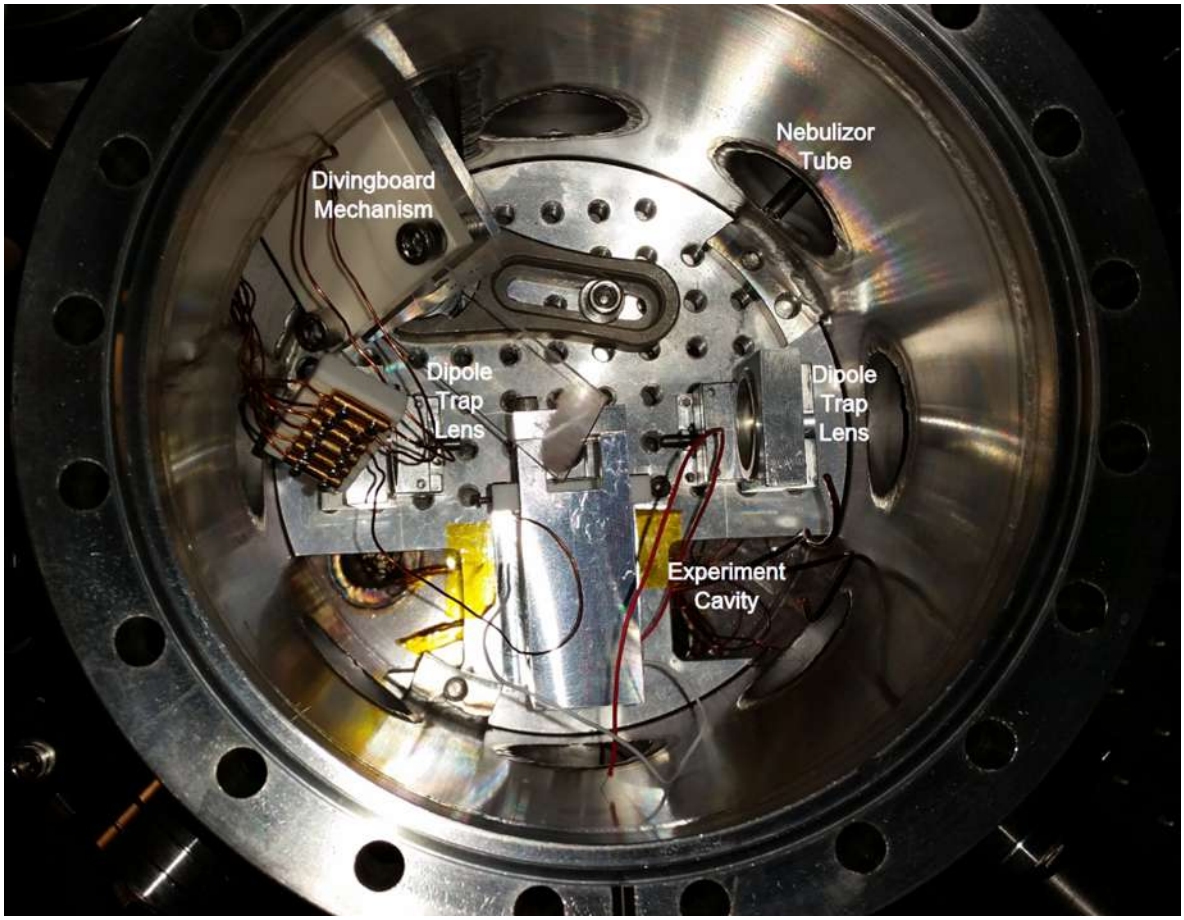

Figure 7.4: The experiment cavity mounted within the experiment vacuum chamber.

group proposes cooling optically levitated micro-spheres to the COM ground state by sympathetic cooling of a cold atomic gas coupled to a micro-sphere trapped in an optical cavity [73]. An extension of this experiment is presented in Ref. [74], where our proposes using a nanoparticle cooled near the quantum ground state as a mater-wave interferometer for sensing short range forces. Refs. [75] [76] propose optically levitating and cooling nano-diamonds with nitrogen-vacancy centers to investigate hybrid opto-mechanical systems that contain both mechanical oscillators and two-level quantum systems. Ref. [77] proposes the use of micro-spheres or micro-discs trapped within an optical cavity for detection of gravitational waves. Whether investigating macroscopic quantum systems, searching for gravitational waves or testing gravity at short range, there are many exciting experiments planned in this field.

Appendix A

Numerical Aperture

Numerical aperture (NA) is a unitless number that characterizes the range of angles at which a system can emit or accept light. In the context of laser physics, NA describes the cone shaped profile of a Gaussian focused beam depicted in figure A.1. NA is given by

$$NA = n\sin(\theta) = n\sin\left[\tan^{-1}\left(\frac{D}{2f}\right)\right] \approx n\frac{D}{2f} \tag{A.1}$$

where n is the index of refraction for the medium in which the lens is working, θ is the divergence angle of the focused beam, D is the beam diameter of a collimated beam incident on a lens and f is the focal length of the lens. D is defined as the width of the collimated beam where the intensity is $1/e^2$ times the maximum intensity, which is on the beam axis. The focal length f is the distance from the lens to the axial location where the beam waist is at a minimum ω_0. As such,

$$\theta = \tan^{-1}\left(\frac{D}{2f}\right). \tag{A.2}$$

For a diffraction limited spot size w_0

$$\theta = \frac{\lambda}{\pi w_0}, \tag{A.3}$$

where λ is the laser wavelength. By combining equations A.1 and A.3 we get

$$w_0 = \frac{n\lambda}{\pi(NA)}. \tag{A.4}$$

Increasing the NA decreases the minimum spot size. For applications of trapping a micro-spheres it is quite often desirable to have a small spot size.

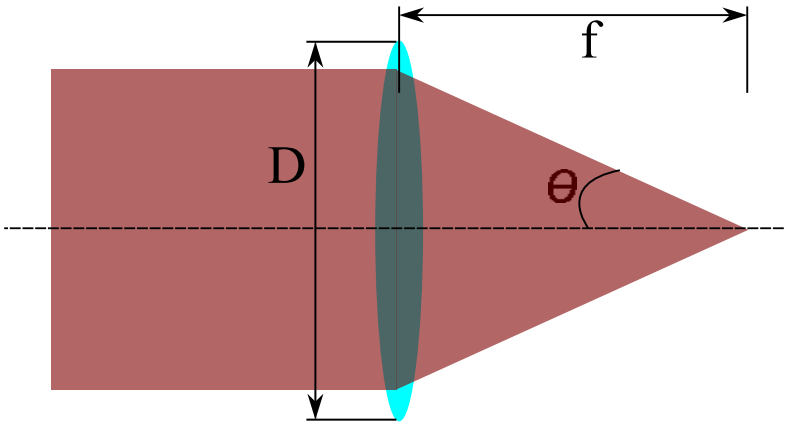

Figure A.1: Illustration of a collimated laser beam focused by a single lens. D is the $\frac{1}{e^2}$ diameter of the incident collimated beam on a focusing lens. The focal length of the lens is f and the divergence angle of the beam is θ.

Appendix B

The Classical Cheshire Cat

The Cheshire Cat phenomenon has recently received significant attention from popular science outlets after the Nature publication of a recent neutron interferometry experiment [78]. In their work, Denkmayr et al. argue that their results can be interpreted as the spin of a neutron being located in one arm of a matter interferometer while the neutron is located in the other. We have reproduced and extended these results with an equivalent optical interferometer. In our experiment, it also appears as if the photon travels through one arm of the interferometer, while its polarization travels through the other. However, we show that these experimental results belong to the domain where quantum and classical wave theories coincide; there is nothing uniquely quantum about the illusion of this Cheshire cat. The work presented in this appendix is published in Ref. [79].

B.1 Weak Measurements

The concept of weak measurements is important for understanding Dankmayr et als. work. Simply put, weak measurements are quantum measurements where the measured system is very weakly coupled to the measuring device, preserving the wave function in an non-collapsed form. Although the concept might appear to contradict basic aspects of quantum mechanics, the formalism lies within the boundaries of theory. The concept was first introduced in 1988 by Aharonov et al. [80]. In 1991, weak measurements were experimentally realized [81]. Ref. [82] is a recent review

(2014) on weak measurements which provides a nice overview of the theory and experiments. The concept has been controversial though [83, 84, 85].

B.2 Quantum Cheshire Cat

In 2013, Aharonov et al. published a paper [86] titled "Quantum Cheshire Cats." Within the paper, they discuss a pre- and post-selected experiment where the circular polarization of a photon is located within one path of an interferometer while the photon itself is located in the other arm. The effect was named after the Alice in Wonderland character, the Cheshire Cat, who has the ability to remove is grin from his body. Dankmayr et al. responded to this paper with the work presented in this appendix.

B.3 Dankmayr et al. Experiment

Figure B.1 contains a simplified drawing of Dankmayr's experiment. A neutron beam

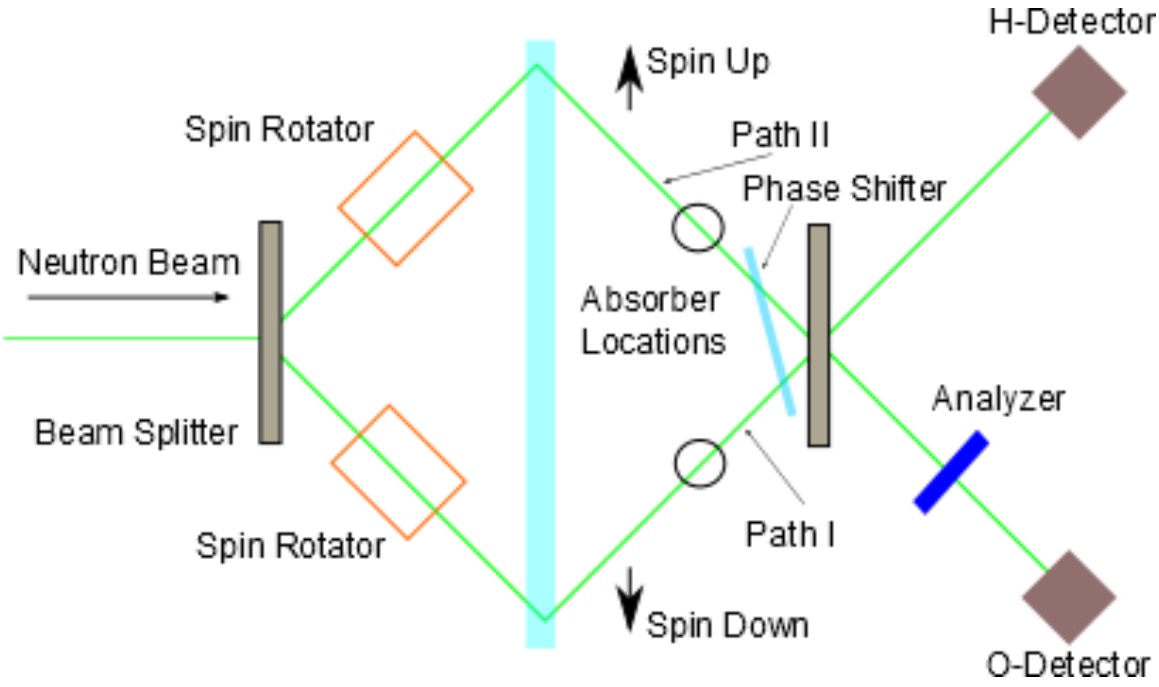

Figure B.1: Dankmayr el al. experiment.

is split into two paths with opposite spin orientations. Each arm contains an absorber location where a weak neutron absorber can be placed for weak location measurements. Also, a weak external magnetic field can be applied to either arm to rotate the neutron spin and perform weak spin measurements. A phase shifter changes the relative phase of the mater waves before the two arms are combined. An analyzer, which blocks spin up particles, is place in front of O-Detector. O-detector is used for all measurements.

B.3.1 Neutron Absorption Measurements

Figure B.2 contains the experimental results and experimental setup for Dankmayr et al.'s absorption measurements for determining the location of the neutron. The

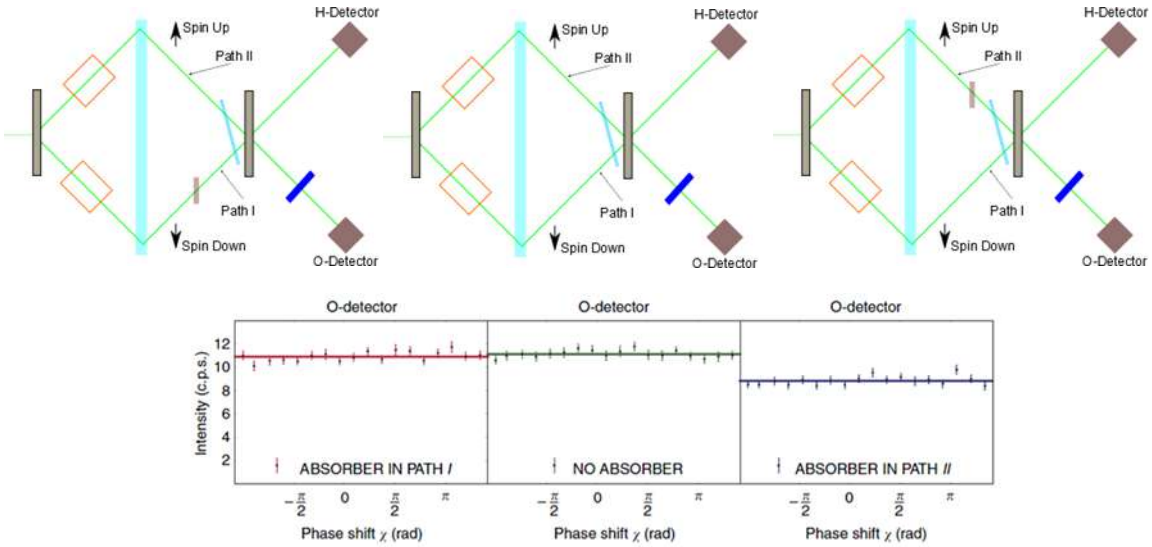

Figure B.2: Dankmayr el al. absorption measurements.

center panel contains a drawing of their system without an absorber placed in either path. The left plot is the signal as a function of phase when an absorber is place in path I and the right plot is the signal when an absorber is placed in path II. A very small effect is observed while the absorber is in path I, whereas a large effect is observed when an absorber is placed in path II. These results can be interpreted as the neutron's location being in path II.

B.3.2 Neutron Spin Measurements

Figure B.3 contains the experimental results and experimental setup for Dankmayr et al.'s spin measurements for determining the location of the neutron's spin. For

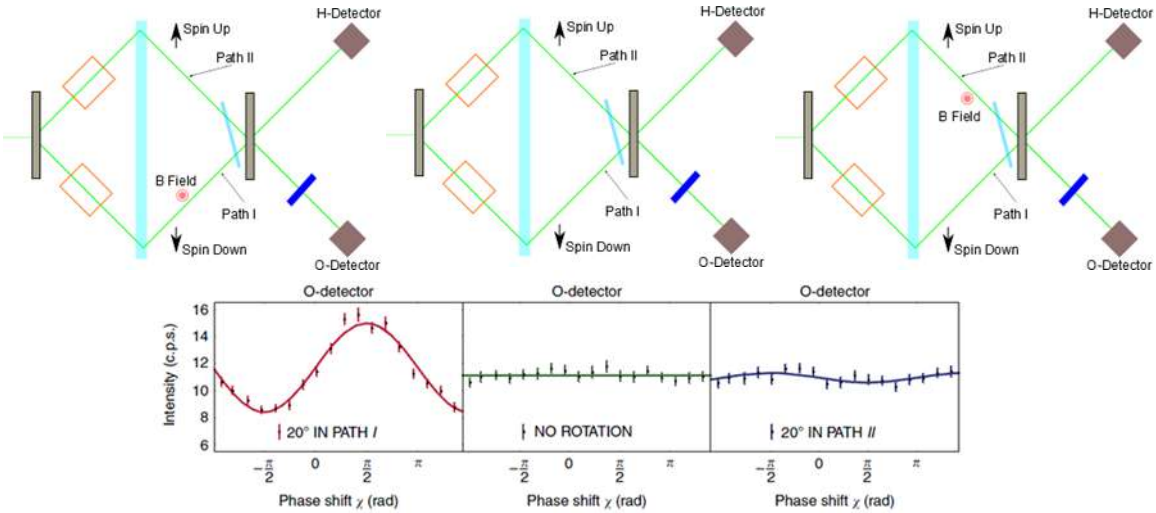

Figure B.3: Dankmayr el al. spin measurements.

these experiments, they applied an external magnetic field in either arm to rotate the neutron's spin. The center plot contains the results for when no external magnetic field was applied. The left plot contains their results for a spin rotation in path I and the right plot contains their results for a spin rotation in path II. For this case, very little interference is observed when a magnetic field is applied to path II. However, noticeable interference is observed when the magnetic field is applied to path I. These results can be interpreted as the spin being located in path I.

B.4 Denkmayr el als. Interpretation

Although the results of Denkmayr et al. are fascinating and thought provoking, we feel that the Cheshire Cat phenomenon is not a uniquely Quantum Mechanical effect. We tested this by reproducing their results with classical laser fields as a photon polarization is mathematically equivalent to a neutron's spin.

B.5 Experiment

The experimental setup is illustrated in FIG. B.4. The laser used was a 780 nm fiber coupled laser stabilized to Rubidium. With a half wave plate and Wollaston prism, the beam was split into two orthogonally polarized beams of equal power. The beams were then mixed with a non-polarizing cube beam splitter. Interference signals from the output of the interferometer were measured with two silicon photo-detectors centered on an interference fringe from the interferometer. The detectors are referred to as detector 1 and detector 2 in FIG. B.4. All measurements reported were obtained with detector 1. Detector 2 was primarily used for alignment purposes. The length of the upper arm in FIG. B.4 is modulated by a mirror mounted on a piezoelectric actuator (piezo.) We refer to this path as "path P" since it contained the piezo. The lower arm is refereed to as "path NP," for "No Piezo." Location A and location B in in FIG. B.4 are the locations where either a half wave plate or neutral density (ND) filter were placed for weak photon polarization and weak location measurements respectively. A linear polarizer placed between the non-polarizing cube beam splitter and detector 1 was rotated to block the polarization of path NP when no wave plate was mounted at location A.

The polarization measurements were taken by rotating the beams' polarization by $-20°, -10°, 0°, 10°$ and $20°$ with a half wave plate placed at either location A or B. A rotation angle of $0°$ results in mixing of two orthoginal beams. A DC signal is measured as the piezo mirror modulates the length of path P as there is no interference. A rotation angle greater than or less than $0°$ projects part of one beam's polarization vector onto the other beam's polarization vector resulting in interference. A sinusoidal signal is measured as the piezo mirror modulates the length of path P.

Location measurements were obtained by placing a ND filter at either location A or B. Measuring a drop in power on the detector implies that the ND filter absorbs some of the photons from the path it is placed in. Not measuring a drop in power can be interpreted as no photons located in the path containing the ND filter.

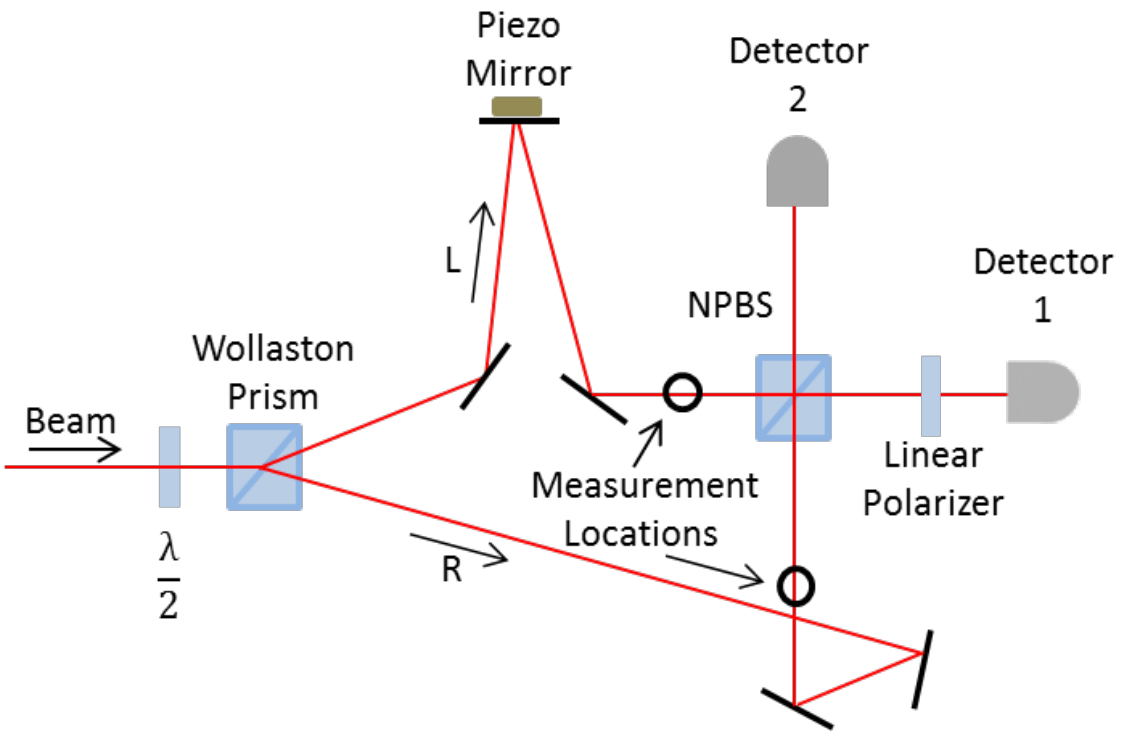

Figure B.4: Experimental setup.

B.6 Results

Plotted in FIG. B.5 is the case where an absorber is placed in either path P or path NP. Also plotted is the signal when no absorber is in place. A drop in DC power was observed when the filter was placed in path P. However, no significant change was observed when the absorber was placed in path NP.

Fig. B.6 contains our polarization results. For rotations in Path P we see very little effect. The DC shift is attributed to a change in total power due to the projection of the path P polarization vector onto the path NP polarization vector. When rotations are performed in path NP, we see a large effect.

In FIG. B.7 we have plotted measurements for the case when an absorber is placed in one beam and rotations are performed on the other beam. This effectively measures the absorption of one beam while measuring the polarization of the other beam simultaneously. For the case where rotations are performed to path P and the

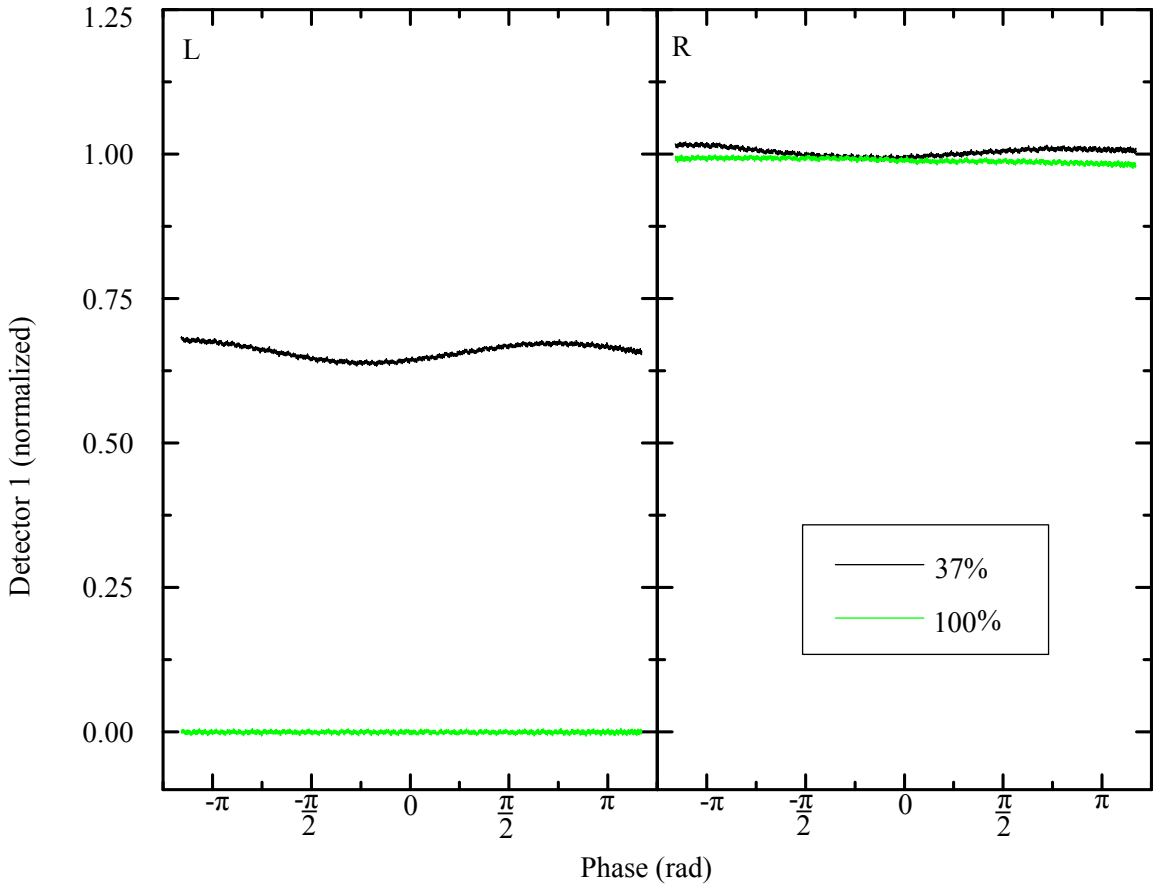

Figure B.5: Location "measurement".

absorber is placed in path NP we see no significant effect to absorption or polarization. However, for the case where rotations are performed in path NP and the absorber is placed in path P we see a significant effect to both absorption and polarization.

B.7 Conclusions

We have reproduced the Cheshire cat results of Dankmay et al. using classical fields. Although Dankmay et al. use a quantum system (mater interferometer) their results are not a purely quantum effect, because we have shown the same effect with classical fields. There is no separation of spin from neutron or polarization from photon. The Cheshire Cat phenomenon is provocative but should be thought of as an illusion and not new science.

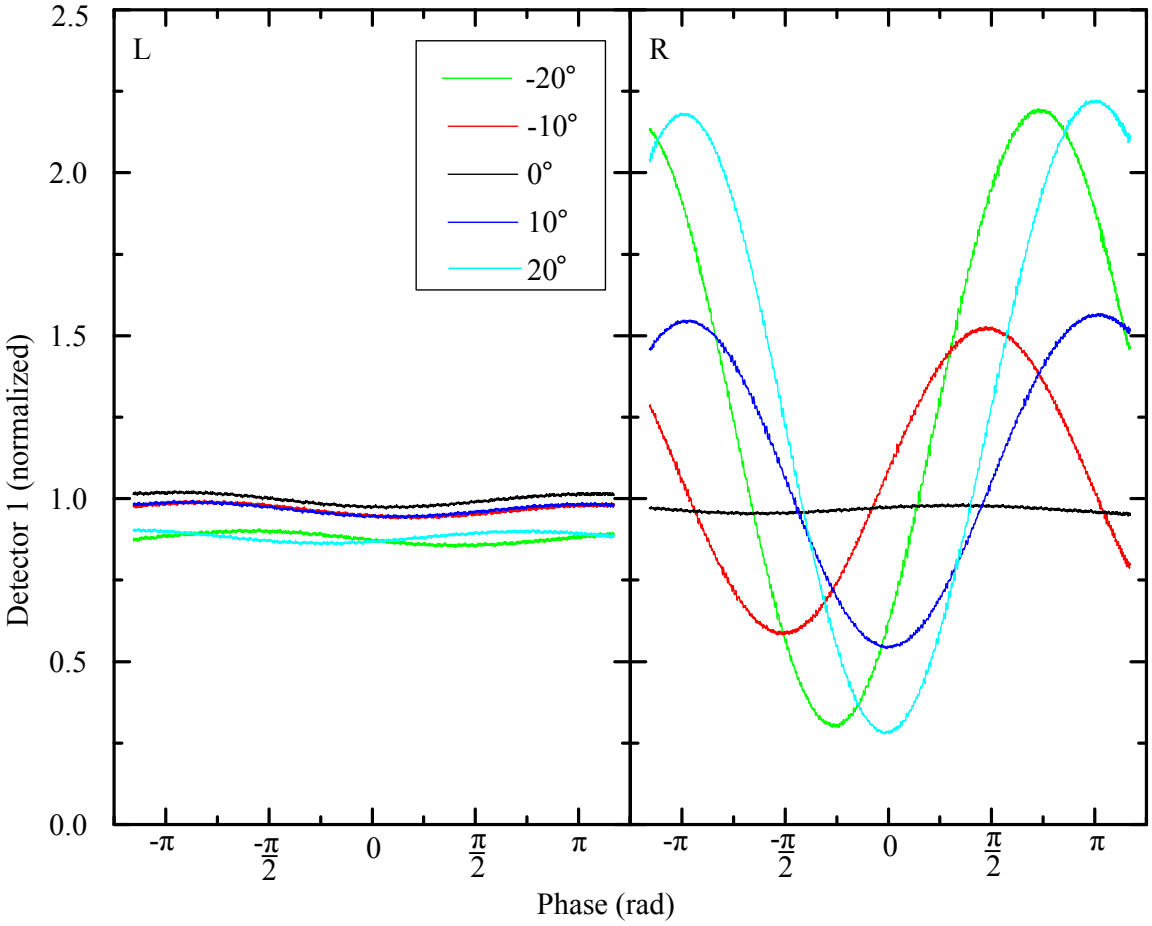

Figure B.6: Polarization "measurement".

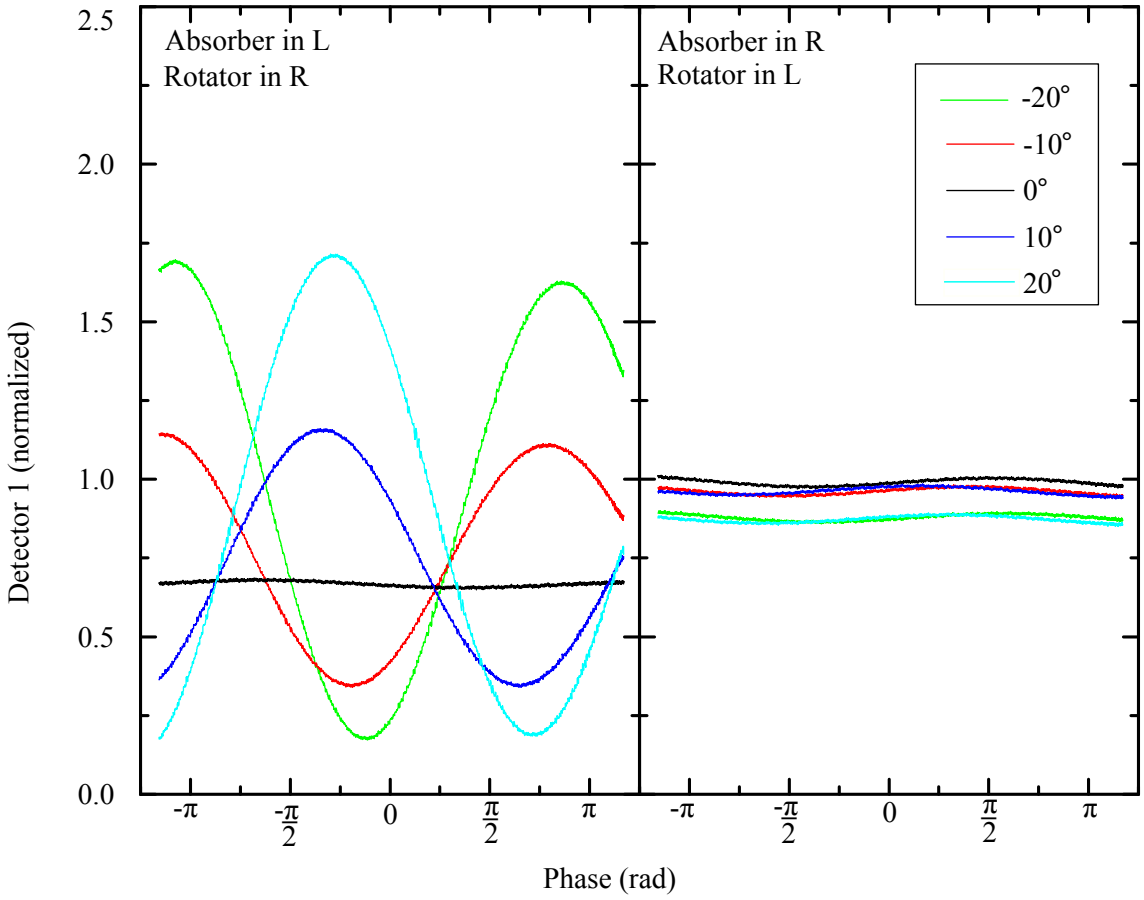

Figure B.7: Simultaneous location and polarization "measurement".

Appendix C

PID Controler

A proportional-integral-derivative controller was designed and built for our experiments. Figure C.1 contains the electronic schematic for the PID controller.

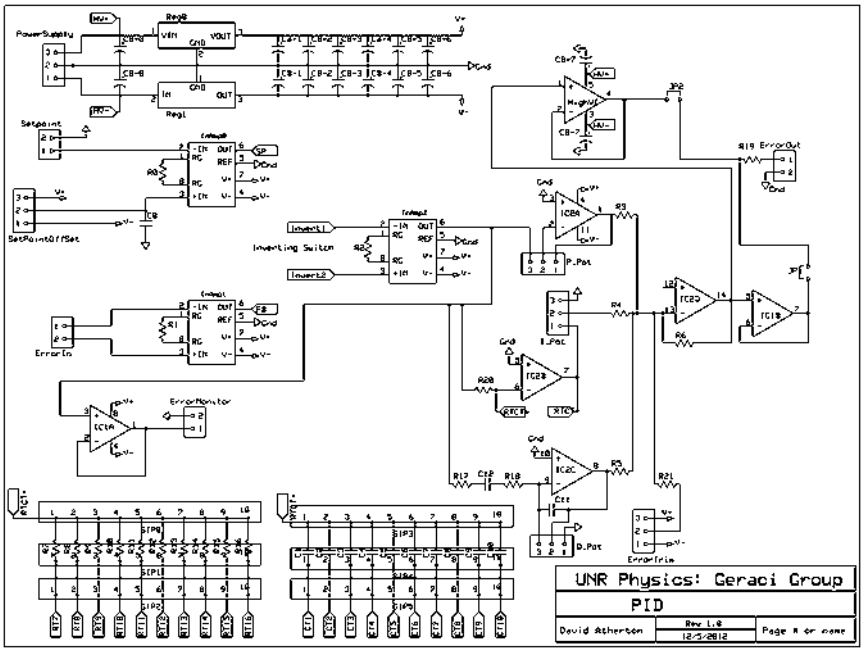

Figure C.1: ExpressPCB schematic for the PID controller.

The instrument requires ±15 V power supplies at the Power-Supply input junction. The ErrorIn junction is where the input signal is input. The set point signal is obtained in one of there ways. The first option is to input a signal from an external source at the Setpoint junction. The second option is to terminate Setpoint to ground and set ±15 V DC set point with a potentiometer connected to SetPointOffset. The

third option is to use both the SetPointOffset and Setpoint signal input.

Once the input and set point signals are provided, instrumentation amplifier InAmp2 provides the difference of the two. A toggle switch swaps the inputs of Inamp2 to provide a sign flip of the out put. The output from InAmp2 can be monitored via ErrorMonitor before the amplification circuits. Potentiometers are connected to the board at P_Pot, I_Pot and D_Pot for the proportional, integral and derivative circuits respectively. The integral circuit has two 10 position toggle switches connected at the RTCT junctions. The switches provide a variety of feedback resistor and capacitor options. The three amplifier outputs are summed with opamp IC2D along with the ErrorTrim signal. The Error trim simply adds a DC -15 - 15 V signal to the error signal. The instrument has a low voltage follower and high voltage follower option for the output. Placing a Molex jumper at either JP1 or JP2 determines which amplifier is used.

Figures C.2 and C.3 contain screen shots of the top and bottom layers of the PID printed circuit board respectively. Figure C.4 is a photograph of the front panel

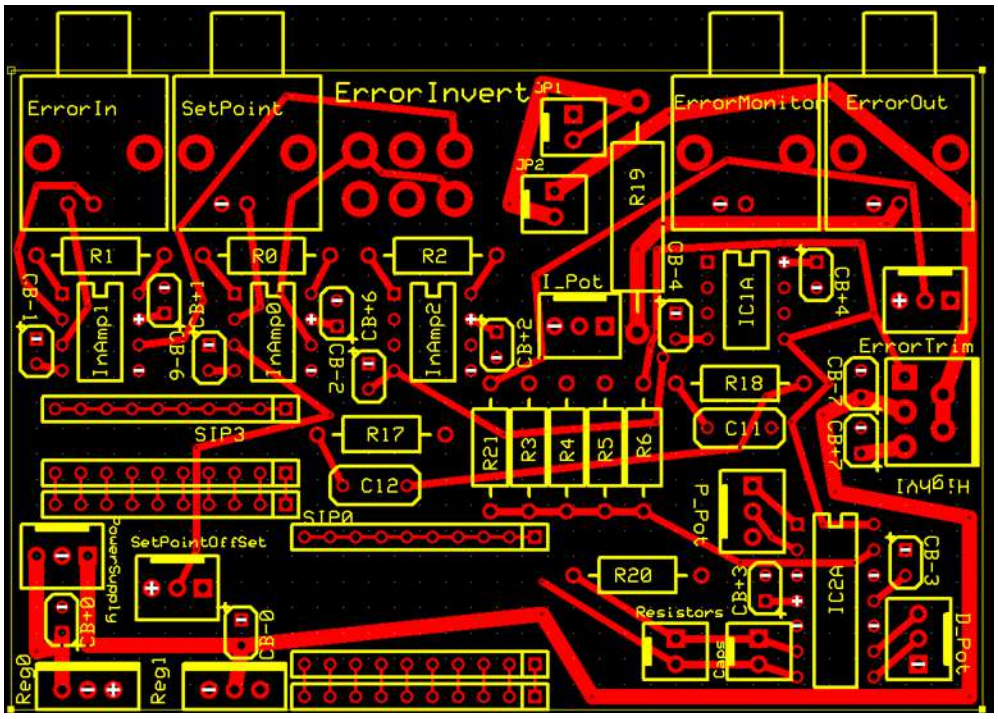

Figure C.2: Top layer of the PID PCB

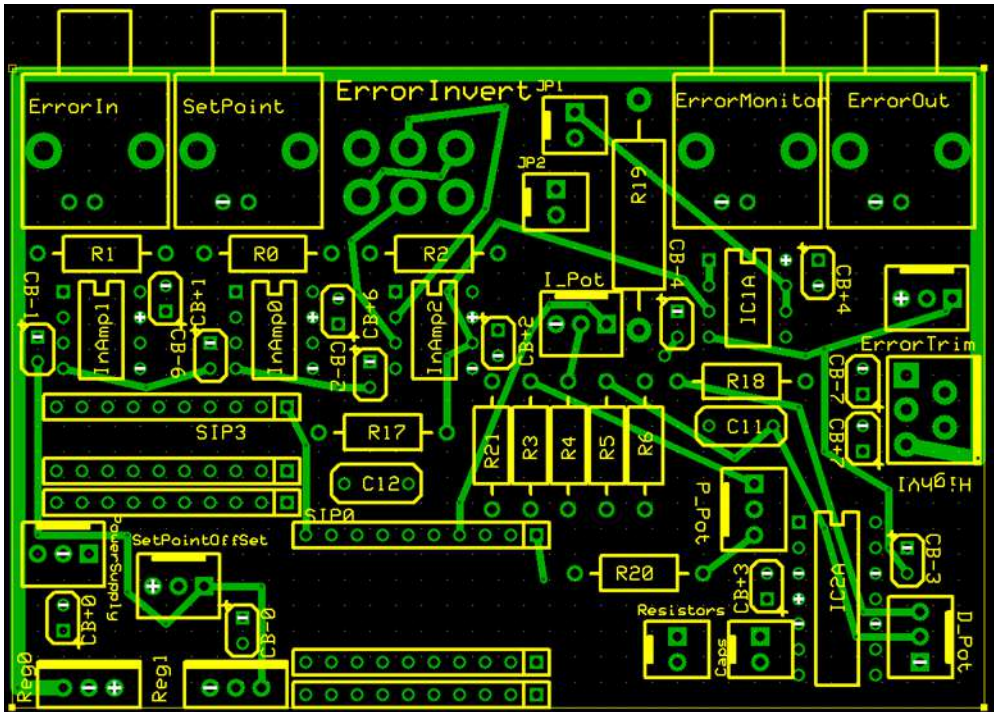

Figure C.3: Bottom layer of the PID PCB

with input, output and control options.

Figure C.4: PID front panel with input, output and control options.

Appendix D

Parametric Feedback Cooling

In ref. [41], Gieseler et al. reported sub-Kelvin cooling of a 30 nm micro-sphere in a single beam dipole trap. In their work, they used a parametric feedback cooling method, which is different from the active feedback cooling we used for the work reported in this dissertation. Parametric feedback cooling works by changing the trap stiffness as a function of bead position. Figure D.1 is a simple illustration of this technique. When the bead moves away from the trap equilibrium position, the trap

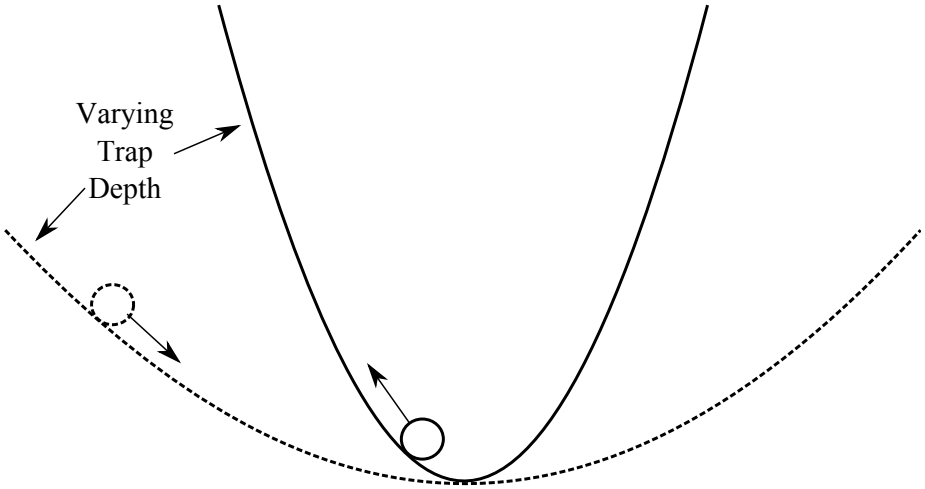

Figure D.1: With parametric feedback cooling, the trap potential is dependent on the position of the micro-sphere.

stiffness (spring constant k) increases. When the bead moves towards the equilibrium position, k is reduced. Since the stiffness of the trap is proportional to the intensity gradient for a dipole trap, the stiffness can be modulated my modulating the trap laser power. The modulation signal is twice the oscillator frequency.

We have modified Gieseler et als. design for possible implementation into our system. Figure D.2 contains an illustration of our design. The imaging system is essentially identical to that presented in this dissertation in that two quadrant photodetectors (QPD) provide voltages (V_x, V_y, V_z), which are proportional to the position of the bead on a rectangular coordinate system. The three signals are first independently frequency doubled. This is achieved by multiplying a position signal by its first derivative (velocity signal.) Next, they are each phase shifted independently. Lastly, they are summed together. The summed signal drives and EOM which modulates the power of the trapping laser at twice the trap frequency of each COM modes of the bead.

The position signals are frequency doubled since we need modulate the trap laser at both turn around points. The phase shifters ensure that the laser modulation is properly in phase with the beads position. The following electronic boxes have already been built for implementation into our system:

- Three phase shifter circuits. Two are optimized for the radial bead motion and one for the axial.
- Three derivative circuits. Two are optimized for the radial bead motion and one for the axial.
- A box with 3 frequency doubling circuits and high pass filters. Each circuit has two inputs. One is for the position signal and the other is for the derivative of the position signal. An AD633 multiplier IC provides a signal proportional twice the input frequencies.
- A simple opamp summing circuit.
- An electronics box with three low pass filters.

Although we have not implemented this system yet, we expect the procedure to parametrically cool a micro-sphere as follows. First, obtain a real time 3-D position

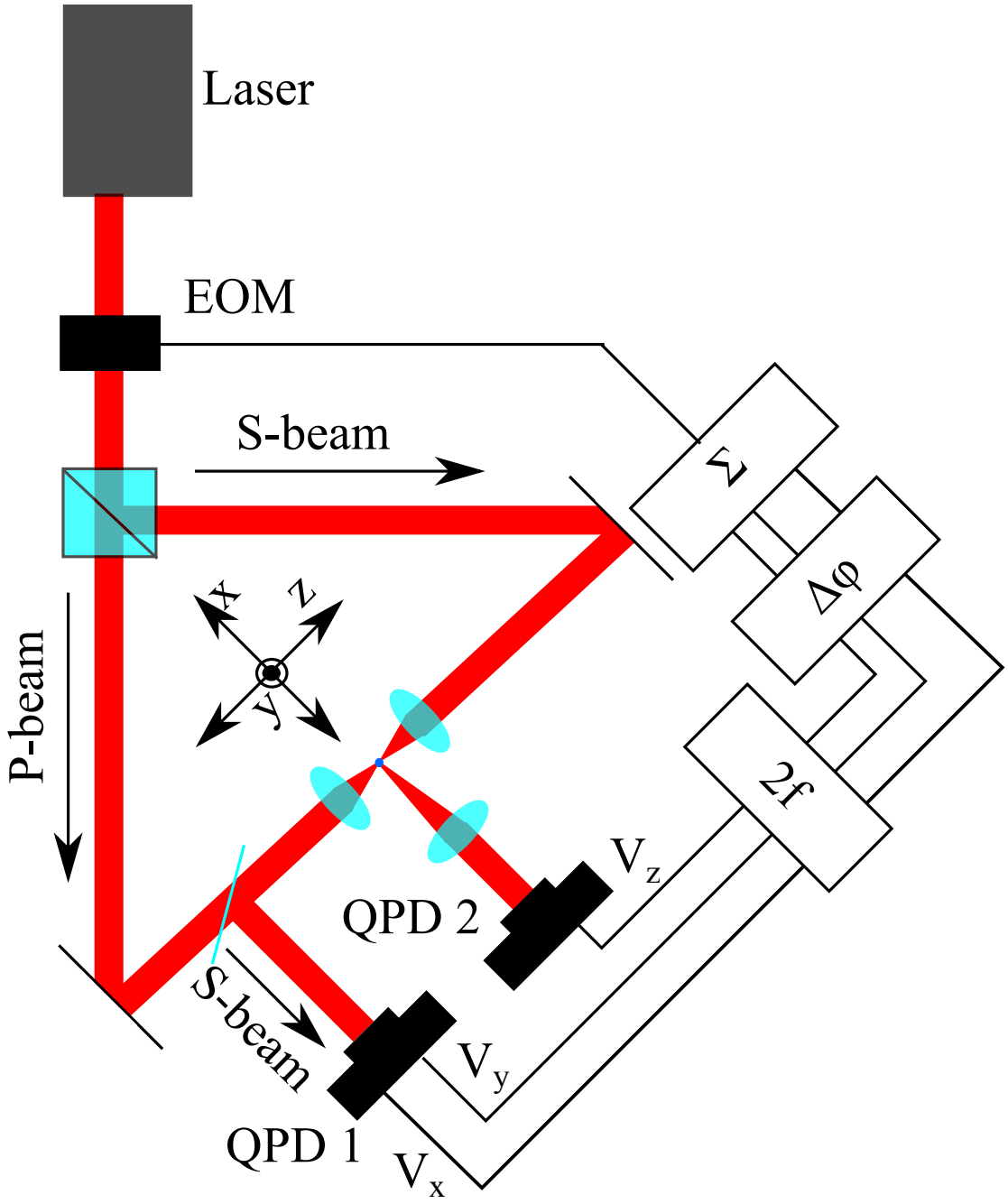

Figure D.2: Proposed parametric feedback feedback cooling system. Two QPDs measure the position of a bead trapped in a dual-beam dipole trap. The x, y, z signals are first frequency doubled by multiplying the position signals by their first derivative (velocity signal.) Next, they are independently phase shifted. Lastly, they are summed. The summed signal drives and EOM which modulates the power of the trapping laser.

power spectrum. Second,individually adjust the phase shifters to maximize cooling. A major advantage of this system over the active feedback method is simplicity.

Bibliography

[1] Andrew A. Geraci, Scott B. Papp, and John Kitching. Short-range force detection using optically cooled levitated microspheres. *Phys. Rev. Lett.*, 105:101101, Aug 2010.

[2] CERN. LHC physics data taking gets underway at new record collision energy of 8tev. Press Release, April 2012.

[3] D. J. Kapner, T. S. Cook, E. G. Adelberger, J. H. Gundlach, B. R. Heckel, C. D. Hoyle, and H. E. Swanson. Tests of the gravitational inverse-square law below the dark-energy length scale. *Phys. Rev. Lett.*, 98:021101, Jan 2007.

[4] S. Dimopoulos and G.F. Giudice. Macroscopic forces from supersymmetry. *Physics Letters B*, 379(14):105 – 114, 1996.

[5] I. Antoniadis, S. Dimopoulos, and G. Dvali. Millimetre-range forces in superstring theories with weak-scale compactification. *Nuclear Physics B*, 516(12):70 – 82, 1998.

[6] Nima Arkani-Hamed, Savas Dimopoulos, and G.R. Dvali. The Hierarchy problem and new dimensions at a millimeter. *Phys.Lett.*, B429:263–272, 1998.

[7] Ignatios Antoniadis, Nima Arkani-Hamed, Savas Dimopoulos, and Gia Dvali. New dimensions at a millimeter to a fermi and superstrings at a tev. *Physics Letters B*, 436(34):257 – 263, 1998.

[8] Nima Arkani-Hamed, Savas Dimopoulos, and Gia Dvali. Phenomenology, astrophysics, and cosmology of theories with submillimeter dimensions and tev scale quantum gravity. *Phys. Rev. D*, 59:086004, Mar 1999.

[9] E. Fischback and C. Talmadge. Ten years of the fifth force. 1996. arXiv:hep-ph/9606249.

[10] S. K. Lamoreaux. Demonstration of the Casimir force in the 0.6 to 6 micrometer range. *Phys. Rev. Lett.*, 78:5–8, Jan 1997.

[11] J. Chiaverini, S. J. Smullin, A. A. Geraci, D. M. Weld, and A. Kapitulnik. New experimental constraints on non-newtonian forces below 100 micrometers. *Phys. Rev. Lett.*, 90:151101, Apr 2003.

[12] Joshua C. Long, Hilton W. Chan, Allison B. Churnside, Eric A. Gulbis, Michael C. M. Varney, and John C. Price. Upper limits to submillimetre-range forces from extra space-time dimensions. *Nature*, 421(6926):922–925, February 2003.

[13] R. S. Decca, D. López, H. B. Chan, E. Fischbach, D. E. Krause, and C. R. Jamell. Constraining new forces in the casimir regime using the isoelectronic technique. *Phys. Rev. Lett.*, 94:240401, Jun 2005.

[14] R. S. Decca, D. López, E. Fischbach, G. L. Klimchitskaya, D. E. Krause, and V. M. Mostepanenko. Tests of new physics from precise measurements of the casimir pressure between two gold-coated plates. *Phys. Rev. D*, 75:077101, Apr 2007.

[15] M. Masuda and M. Sasaki. Limits on nonstandard forces in the submicrometer range. *Phys. Rev. Lett.*, 102:171101, Apr 2009.

[16] Andrew A. Geraci, Sylvia J. Smullin, David M. Weld, John Chiaverini, and Aharon Kapitulnik. Improved constraints on non-newtonian forces at 10 microns. *Phys. Rev. D*, 78:022002, Jul 2008.

[17] A. O. Sushkov, W. J. Kim, D. A. R. Dalvit, and S. K. Lamoreaux. Observation of the thermal Casimir force. *Nature Physics*, 7:230–233, March 2011.

[18] H.B.G. Casimir. On the Attraction Between Two Perfectly Conducting Plates. *Indag.Math.*, 10:261–263, 1948.

[19] M. J. Sparnaay. Attractive Forces between Flat Plates. *Nature*, 180:334–335, August 1957.

[20] M. J. Sparnaay. Measurements of attractive forces between flat plates. *Physica*, 24:751–764, 1958.

[21] U. Mohideen and A. Roy. Precision Measurement of the Casimir Force from 0.1 to 0.9 μm. *Physical Review Letters*, 81:4549–4552, November 1998.

[22] C. I. Sukenik, M. G. Boshier, D. Cho, V. Sandoghdar, and E. A. Hinds. Measurement of the casimir-polder force. *Phys. Rev. Lett.*, 70:560–563, Feb 1993.

[23] D. M. Harber, J. M. Obrecht, J. M. McGuirk, and E. A. Cornell. Measurement of the casimir-polder force through center-of-mass oscillations of a bose-einstein condensate. *Phys. Rev. A*, 72:033610, Sep 2005.

[24] M. Biercuk, H. Uys, J. Britton, A. VanDevender, and J. Bollinger. Ultrasensitive detection of force and displacement using trapped ions. *Nature Nanotechnology.*, 5:646–650, 2010.

[25] Lambrecht, A. and Reynaud, S. Casimir force between metallic mirrors. *Eur. Phys. J. D*, 8(3):309–318, 2000.

[26] I. Lekavicius. Towards investigating the casimir effect in a new regime, 2013. B.S. thesis.

[27] V.V. Nesvizhevsky. Interaction of neutrons with nanoparticles. *Physics of Atomic Nuclei*, 65(3):400–408, 2002.

[28] E.V. Lychagin, D.G. Kartashov, A.Yu. Muzychka, V.V. Nesvizhevsky, G.V. Nekhaev, and A.V. Strelkov. Mechanism of small variations in energy of ultracold neutrons interacting with a surface. *Physics of Atomic Nuclei*, 65(11):1995–1998, 2002.

[29] D. G. KARTASHOV, E. V. LYCHAGIN, A. Yu. MUZYCHKA, V. V. NESVIZHEVSKY, G. V. NEKHAEV, and A. V. STRELKOV. An investigation into the origin of small energy changes (10-7ev) of ultracold neutrons in traps. *International Journal of Nanoscience*, 06(06):501–513, 2007.

[30] J. Kepler. *De cometis libelli tres ...* De cometis libelli tres. Typis Andreæ Apergeri, sumptibus Sebastiani Mylii bibliopolæ Augustani, 1619.

[31] J. C. Maxwell. *A treatise on electricity and magnetism*. De cometis libelli tres. Dover, 1891, 1873.

[32] D. M. Harber, J. M. Obrecht, J. M. McGuirk, and E. A. Cornell. Untersuchungen ber die druckkrfte des lichtes. *Annalen der Physik*, pages 433–458, 1901.

[33] E. F. Nichols and G. F. Hull. A preliminary communication on the pressure of heat and light radiation. *Phys. Rev. (Series I)*, 13:307–320, Nov 1901.

[34] Charles H. Townes. *How the laser happened : adventures of a scientist / Charles H. Townes*. Oxford University Press New York, 1999.

[35] A. Ashkin. Acceleration and trapping of particles by radiation pressure. *Physical Review Letters*, 24(4):156–159, January 1970.

[36] O. Marago, P. Jones, P. Gucciardi, G. Volpe, and A. Ferrari. Optical trapping and manipulation of nanostructures. *Nature Nanotechnology.*, 8:807–819, 2013.

[37] A. Ashkin and J. M. Dziedzic. Optical levitation by radiation pressure. *Applied Physics Letters*, 19(8):283–285, 1971.

[38] A. Ashkin and J. M. Dziedzic. Optical levitation in high vacuum. *Applied Physics Letters*, 28(6):333–335, 1976.

[39] A. Ashkin and J. M. Dziedzic. Feedback stabilization of optically levitated particles. *Applied Physics Letters*, 30(4):202–204, 1977.

[40] Tongcang Li, Simon Kheifets, and Mark G. Raizen. Millikelvin cooling of an optically trapped microsphere in vacuum. *Nature Phys.*, 7:527–530, 2011.

[41] Jan Gieseler, Bradley Deutsch, Romain Quidant, and Lukas Novotny. Subkelvin parametric feedback cooling of a laser-trapped nanoparticle. *Phys. Rev. Lett.*, 109:103603, Sep 2012.

[42] A. Ashkin. Forces of a single-beam gradient laser trap on a dielectric sphere in the ray optics regime. *Biophysical Jopurnal*, 61:569–582, 1992.

[43] W. H. Wright, G. J. Sonek, and M. W. Berns. Parametric study of the forces on microspheres held by optical tweezers. *Appl. Opt.*, 33(9):1735–1748, Mar 1994.

[44] K. Im, H. Kim, C. Oh, S. Song, P. Kim, and B. Park. Calculation of Optical Trapping Forces on Microspheres in the Ray Optics Regime. *Journal of the Korean Physics Society*, 40(5):930–933, 2002.

[45] A. Callegari, M. Mijalkov, A. Gokos, and G Volpe. Computational toolbox for optical tweezers in geometrical optics. *arxive.org*, 2014.

[46] Yasuhiro Harada and Toshimitsu Asakura. Radiation forces on a dielectric sphere in the rayleigh scattering regime. *Optics Communications*, 124(56):529 – 541, 1996.

[47] MATLAB functions for Mie scattering and absorption. `http://arrc.ou.edu/~rockee/NRA_2007_website/Mie-scattering-Matlab.pdf`. Accessed: 2014-07-19.

[48] Timo A Nieminen, Vincent L Y Loke, Alexander B Stilgoe, Gregor Knner, Agata M Braczyk, Norman R Heckenberg, and Halina Rubinsztein-Dunlop. Optical tweezers computational toolbox. *Journal of Optics A: Pure and Applied Optics*, 9(8):S196, 2007.

[49] S. Yushanov, J. S. Crompton, and K. C. Koppenhoefer. Mie scattering of electromagnetic waves. 2013.

[50] Mie scattering calculator by scott prahl. `http://omlc.org/calc/mie_calc.html`. Accessed: 2014-07-19.

[51] James A. Lock and Grard Gouesbet. Generalized lorenzmie theory and applications. *Journal of Quantitative Spectroscopy and Radiative Transfer*, 110(11):800 – 807, 2009. Light Scattering: Mie and More Commemorating 100 years of Mie's 1908 publication.

[52] Melles Griot (Firm). *Optics Guide: 4*. Melles Griot, 1988.

[53] Tongcang Li. *Fundamental tests of physics with optically trapped microspheres*. PhD thesis, The University of Texas at Austin, Austin, Texas, May 2011.

[54] M. Beck. Overcoming stiction forces: Launching silica microspheres into an optical trap, 2012. B.S. thesis.

[55] B.V Derjaguin, V.M Muller, and Yu.P Toporov. Effect of contact deformations on the adhesion of particles. *Journal of Colloid and Interface Science*, 53(2):314 – 326, 1975.

[56] Lars-Oliver Heim, Jürgen Blum, Markus Preuss, and Hans-Jürgen Butt. Adhesion and friction forces between spherical micrometer-sized particles. *Phys. Rev. Lett.*, 83:3328–3331, Oct 1999.

[57] H. Nyquist. Thermal agitation of electric charge in conductors. *Phys. Rev.*, 32:110–113, Jul 1928.

[58] S. A. Beresnev, V. G. Chernyak, and G. A. Fomyagin. Motion of a spherical particle in a rarefied gas. part 2. drag and thermal polarization. *Journal of Fluid Mechanics*, 219:405–421, 10 1990.

[59] Yohai Roichman, Bo Sun, Allan Stolarski, and David G. Grier. Influence of nonconservative optical forces on the dynamics of optically trapped colloidal spheres: The fountain of probability. *Phys. Rev. Lett.*, 101:128301, Sep 2008.

[60] Pinyu Wu, Rongxin Huang, Christian Tischer, Alexandr Jonas, and Ernst-Ludwig Florin. Direct measurement of the nonconservative force field generated by optical tweezers. *Phys. Rev. Lett.*, 103:108101, Sep 2009.

[61] J. Millen, T. Deesuwan, P. Barker, and J. Anders. Nanoscale temperature measurements using non-equilibrium Brownian dynamics of a levitated nanosphere. *Nature Nanotechnology*, 9:425–429, June 2014.

[62] D. E. Chang, C. A. Regal, S. B. Papp, D. J. Wilson, J. Ye, O. Painter, H. J. Kimble, and P. Zoller. Cavity opto-mechanics using an optically levitated nanosphere. *Proceedings of the National Academy of Sciences*, 107(3):1005–1010, 2010.

[63] Rei Kitamura, Laurent Pilon, and Miroslaw Jonasz. Optical constants of silica glass from extreme ultraviolet to far infrared at near room temperature. *Appl. Opt.*, 46(33):8118–8133, Nov 2007.

[64] J. Wodjula. In perpetration. Master's thesis, The University of Nevada in Reno, 2015.

[65] N. A. Fuchs. *The Mechanics of Aerosols*. Dover, 1926.

[66] G. Ranjit, D. P. Atherton, J. H. Stutz, M. Cunningham, and A. A. Geraci. Attonewton force detection using microspheres in a dual-beam optical trap in high vacuum. *ArXiv e-prints*, March 2015.

[67] John A Marohn. The minimum detectable force concept. Technical report, Department of Chemistry and Chemical Biology, Cornell University, 2006.

[68] Z.-Q. Yin, A. A. Geraci, and T. Li. Optomechanics of Levitated Dielectric Particles. *International Journal of Modern Physics B*, 27:30018, September 2013.

[69] J. Stutz. Calibration of an optically levitated microsphere as a force sensor, 2014. M.S. thesis.

[70] P. Ji, M. Momeen, J. Hsu, B D'Urso, and G. Dutt. Towards a quantum interface between diamond spin qubits and phonons in an optical trap. 2014. DAMOP poster: http://meetings.aps.org/link/BAPS.2014.DAMOP.Q1.100.

[71] N. Kiesel, F. Blaser, U. Delic, D. Grass, R. Kaltenbaek, and M. Aspelmeyer. Cavity cooling of an optically levitated submicron particle. *Proceedings of the National Academy of Science*, 110:14180–14185, August 2013.

[72] J. Millen, P. Z. G. Fonseca, T. Mavrogordatos, T. S. Monteiro, and P. F. Barker. Cavity cooling a single charged nanoparticle. *ArXiv e-prints*, July 2014.

[73] Gambhir Ranjit, Cris Montoya, and Andrew A. Geraci. Cold atoms as a coolant for levitated optomechanical systems. *Phys. Rev. A*, 91:013416, Jan 2015.

[74] A. Geraci and H. Goldman. Sensing short-range forces with a nanosphere matter-wave interferometer. 2014. arXiv:1412.4482.

[75] Z. Yin, N. Zhao, and T. Li. Hybrid opto-mechanical systems with nitrogen-vacancy centers. 2015. arXiv:1501.00636.

[76] Z. Yin, T. Li, X. Zhang, and L. Duan. Large quantum superpositions of a levitated nanodiamond through spin-optomechanical coupling. 2013. arXiv:1305.1701.

[77] Asimina Arvanitaki and Andrew A. Geraci. Detecting high-frequency gravitational waves with optically levitated sensors. *Phys. Rev. Lett.*, 110:071105, Feb 2013.

[78] Tobias Denkmayr, Hermann Geppert, Stephan Sponar, Hartmut Lemmel, Alexandre Matzkin, Jeff Tollaksen, and Yuji Hasegawa. Observation of a quantum Cheshire Cat in a matter-wave interferometer experiment. *Nature Communications*, 5, July 2014.

[79] David P. Atherton, Gambhir Ranjit, Andrew A. Geraci, and Jonathan D. Weinstein. Observation of a classical cheshire cat in an optical interferometer. *Opt. Lett.*, 40(6):879–881, Mar 2015.

[80] Yakir Aharonov, David Z. Albert, and Lev Vaidman. How the result of a measurement of a component of the spin of a spin- *1/2* particle can turn out to be 100. *Phys. Rev. Lett.*, 60:1351–1354, Apr 1988.

[81] N. W. M. Ritchie, J. G. Story, and Randall G. Hulet. Realization of a measurement of a "weak value". *Phys. Rev. Lett.*, 66:1107–1110, Mar 1991.

[82] Justin Dressel, Mehul Malik, Filippo M. Miatto, Andrew N. Jordan, and Robert W. Boyd. *Colloquium* : Understanding quantum weak values: Basics and applications. *Rev. Mod. Phys.*, 86:307–316, Mar 2014.

[83] A. J. Leggett. Comment on "how the result of a measurement of a component of the spin of a spin-(1/2 particle can turn out to be 100". *Phys. Rev. Lett.*, 62:2325–2325, May 1989.

[84] I. M. Duck, P. M. Stevenson, and E. C. G. Sudarshan. The sense in which a "weak measurement" of a spin-1/2 particle's spin component yields a value 100. *Phys. Rev. D*, 40:2112–2117, Sep 1989.

[85] Konstantin Y Bliokh, Aleksandr Y Bekshaev, Abraham G Kofman, and Franco Nori. Photon trajectories, anomalous velocities and weak measurements: a classical interpretation. *New Journal of Physics*, 15(7):073022, 2013.

[86] Yakir Aharonov, Sandu Popescu, Daniel Rohrlich, and Paul Skrzypczyk. Quantum cheshire cats. *New Journal of Physics*, 15(11):113015, 2013.